NUMERICAL MODELING OF SEASONALLY FREEZING GROUND AND PERMAFROST

A

THESIS

Presented to the Faculty

of the University of Alaska Fairbanks

in Partial Fulfillment of the Requirements

for the Degree of

DOCTOR OF PHILOSOPHY

By

Dmitry J. Nicolsky, B.S., M.S.

Fairbanks, Alaska

December 2007

NUMERICAL MODELING OF SEASONALLY FREEZING GROUND AND PERMAFROST

By

Dmitry J. Nicolsky

RECOMMENDED:

Advisory Committee Chair

Chair, Department of Geology and Geophysics

APPROVED:

Dean, College of Natural Science and Mathematics

Dean of the Graduate School

Nov 27, 2007

Date

Abstract

This thesis represents a collection of papers on numerical modeling of permafrost and seasonally freezing ground dynamics.

An important problem in numerical modeling of temperature dynamics in permafrost and seasonally freezing ground is related to parametrization of already existing models. In this thesis, a variation data assimilation technique is presented to find soil properties by minimizing the discrepancy between in-situ measured temperatures and those computed by the models. The iterative minimization starts from an initial approximation of the soil properties that are found by solving a sequence of simple subproblems. In order to compute the discrepancy, the temperature dynamics is simulated by a new implementation of the finite element method applied to the heat equation with phase change. Despite simplifications in soil physics, the presented technique was successfully applied to recover soil properties, such as thermal conductivity, soil porosity, and the unfrozen water content, at several sites in Alaska. The recovered properties are used in discussion on soil freezing/thawing and permafrost dynamics in other parts of this thesis.

Another part of this thesis concerns development of a numerical thermo-mechanical model of seasonal soil freezing on the lateral scale of several meters. The presented model explains observed differential frost heave occurring in non-sorted circle ecosystems north of the Brooks Range in the Alaskan tundra. The model takes into account conservation principles for energy, linear momentum and mass of three constituents: liquid water, ice and solid particles. The conservation principles are reduced to a computationally convenient system of coupled equations for temperature, liquid water pressure, porosity, and the velocity of soil particles in a three-dimensional domain with cylindrical symmetry. Despite a simplified rheology, the model simulates the ground surface motion, temperature, and water dynamics in soil and explains dependence of the frost heave on specific environmental properties of the ecosystem.

In the final part, simulation of the soil temperature dynamics on the global scale is addressed. General Circulation Models are used to understand and predict future climate change, but most of them do not simulate permafrost dynamics and its potentially critical feedback on climate. In this part, a widely used climate model is evaluated and the simulated temperatures are compared against observations. Based on this comparison, several modifications to the Global Circulation Models are identified to improve the fidelity of permafrost and soil temperature simulations. These modifications include increasing the total

soil depth by adding new layers, incorporating a surface organic layer, and modifying the numerical scheme to include unfrozen water dynamics.

Table of Contents

Page

Page

Page

List of Figures

Page

List of Tables

Acknowledgements

I am grateful to my advisor Dr. Vladimir Romanovsky for his inspiring scientific discussions and encouragement. Without his guidance and support this thesis would has never been completed in its present form. My deepest appreciation to Dr. Vladimir Romanovsky is for creating an atmosphere of colleagueship and friendship in which his expert guidance and assistance in any aspect of my research was truly indispensable. I owe him an inestimable debt of gratitude. Additionally, I am eager to express my gratitude to all present and past members of my graduate committee: Dr. Gerhard Kramm, Dr. Paul Layer, Dr. Glen Shaw, Dr. Gennadiy Tipenko, Dr. Gleb Panteleev, and Dr. Donald Walker for their critical review of my thesis, commitment of time and willingness to help me in this work.

I was very fortunate that at the beginning of my study, Dr. Gennadiy Tipenko arrived in Fairbanks and worked on numerical modeling of permafrost in the Geophysical Institute. From him I learned arts of numerical simulations, from writing a basic numerical scheme on a piece of scratch paper through implementing this scheme on a computer and verifying the computations. In addition to Gennadiy's help, numerous discussions regarding numerical modeling with Dr. Edward Bueler and Dr. Martin Trueffer provided me with a great deal of inspirations and confidence in computations.

I am thankful to Dr. Donald (Skip) Walker, who showed me the beauty of the arctic tundra and taught me an unforgettable course in Arctic ecosystems. From him I recognized and understood how fragile the Arctic tundra is. Skip helped me tremendously by providing his experience, and by supporting my field work and trips to conferences through his grants.

I greatly appreciate Dr. Gleb Panteleev's help, who motivated me to study data assimilation techniques. Without the inspiration he has been constantly giving me, without his lectures on adjoint problems and multivariate minimization, this thesis would not have been "optimal".

I would like to thank Dr. Vladimir Alexeev and Dr. David Lawrence for introducing me to the global climate models. With their support and invaluable advice a substantial part of this thesis was completed. They both helped me tremendously in acquiring, interpreting and validating computations, as well as publishing the results of our study. I am also thankful to Dr. Michael Rawlins who taught me modeling global scale hydrology and parametrization of land surface schemes.

Special thanks to Dr. Uma Bhatt and Dr. Igor Polykov, from whom I gained experience in structuring and writing proposal. Even though our proposal has not been funded, I gained

knowledge how to structure and to clearly write proposals. This precious knowledge later played a crucial role in obtaining a grant from the Center for Global Change and Arctic System Research and the Office of the Graduate School. I gratefully acknowledge these organizations for their interest in my research and for providing financial support.

My special appreciation is expressed to Alexey and to Marina. Being a graduate student, I could always rely on their advice whether it was on research or in life. I am particularly thankful to Alexandr Chirtsov for showing me a beautiful world of physics. I am thankful to my friends: John Doe (Re: dorofeev), Jake, David & Elise, Lars, Mike, Pavel & Luda, Elçin, Victor, Elena, and Diane.

Finally, I would like to thank my colleagues Sergei Marchenko, Guido Grosse, Alexandr Kholodov, and Ronald Daanen for their advice, assurance and help along the way. The overwhelming part of the financial support for this study was provided by the ARCSS Program and by the Polar Earth Science Program, Office of Polar Programs, National Science Foundation (OPP-0120736, ARC-0632400, ARC-0520578, ARC-0612533, IARC-NSF CA: Project 3.1 Permafrost Research), by NASA Water and Energy Cycle grant, by UAF CIFAR Student Award, and by the State of Alaska.

General Introduction

In this thesis, I present a collection of five articles (chapters) focused on the modeling of seasonally freezing ground and permafrost. Three common threads weave through these five papers. The first thread is modeling phase change of ground water trapped in the soil pores. Freezing of water trapped in the ground material is a complicated physical process that is still poorly understood. There are many models of freezing and thawing soil, some of them are described *Goodrich* (1982); *Nelson and Outcalt* (1987); *Kane et al.* (1991); *Zhuang et al.* (2001); *Ling and Zhang* (2003); *Oleson et al.* (2004); *Sazonova et al.* (2004) and *Mölders and Romanovsky* (2006). Typically the models are formulated in the language of partial differential equations that include non-linearities. Due to the non-linearities, application of the analytical methods to compute a solution of the partial differential equations is limited. Hence, numerical methods are typically employed to predict the evolution of soil temperature dynamics.

Another thread that weaves through the thesis is related to parametrization of the permafrost models used to calculate the soil temperature dynamics. Key parameters in the models are thermal and hydrological properties of the ground material. At present time, these properties are known for a small portion of the land surface area. However, the soil temperature data (*Muhll et al.*, 1998; *Brown et al.*, 2000; *Oberman and Mazhitova*, 2001; *Romanovsky et al.*, 2001; *Burgess et al.*, 2002; *Clow and Urban*, 2002; *Pavlov and Moskalenko*, 2002; *Romanovsky et al.*, 2002; *Nixon et al.*, 2003; *Osterkamp*, 2003; *Marchenko et al.*, 2007) collected in numerous locations across the pan-Arctic can be used in inverse modeling techniques to find thermal and hydrological properties of the ground material. In this thesis, I show that temperature records at several depths beneath the soil surface, and instantaneous temperature profiles in relatively deep boreholes can be assimilated to recover the unknown soil properties. Once the soil properties are found they can be used to reconstruct soil temperature dynamics in the past and also to project its future evolution.

The third thread that interconnects the chapters is related to modeling soil freezing and thawing on different spatial and temporal scales. I describe a detailed thermo-mechanical model of freezing soil. The model addresses water, temperature, and soil particle dynamics on the local scale - several meters. Since the presented thermo-mechanical model is computationally expensive, its execution by nowadays computers on the pan-Arctic scale requires an enormous amount of time. After analyzing the temperature and water transport on

the local scale, I propose suggestions to improve modeling of temperature dynamics by the Global Circulation Models. The proposed suggestions lessen biases in the Global Circulation Models and improve simulation of the temperature dynamics for the Arctic regions on the Earth.

In Chapter 1, I and several colleagues propose a method to determine an initial approximation to the soil properties using observed temperature time series at specified depths. The described method is based on solution of simpler subproblems and is tested on field data. To compute the temperature dynamics in the freezing and thawing ground, a novel finite element method is proposed. In this chapter, a special emphasis is put on necessity of good initial values of the thermal properties which can be used later in variational data assimilation problems.

In Chapter 2, we describe a variational data assimilation to estimate the soil properties using high-resolution-in-time temperature records at several depths beneath the soil surface, and instantaneous temperature profiles in a deep borehole. We conduct a sensitivity analysis which shows robustness and efficiency of the variational approach. We applied the developed tool to estimate soil properties at several sites in Alaska.

In Chapter 3, we use the obtained knowledge on estimation of soil thermal properties, to investigate bio-geophysical processes causing differential frost heave in non-sorted circles north of the Alaska's Brooks Range. The main question addressed is "How does heterogeneity in soil properties and ground surface conditions cause the differential frost heave observed within the non-sorted circle?" We address this question by developing a numerical thermo-mechanical model of a non-sorted circle. The performed sensitivity study of predicted differential frost heave with respect to soil physical properties and vegetation characteristics shows that hydrological and thermal properties as well as the local heterogeneity in the distribution of the surface vegetation have a decisive role in formation of the differential frost heave.

In Chapter 4, we describe an approach to improve global climate models which are frequently used to understand and predict future climate change. In particular, we evaluate the Community Land Model, which is a land-surface scheme, against observations and identify potential modifications to this model that improve fidelity of permafrost and soil temperature simulations

In Chapter 5, we examine the Community Land Model and its modifications. We estimate the required thickness of soil layers to calculate temperature dynamics within

certain errors. Our results show that to compute the annual cycle of temperature dynamics for cold permafrost, the soil thickness should be at least 30 meters.

All five chapters were originally written as stand-alone manuscripts, which have been published, submitted or are to be submitted for publication. The first paper is co-authored with Drs. Vladimir Romanovsky and Gennadiy Tipenko. Dr. Vladimir Romanovsky is also my co-author in the second paper, as well as Dr. Gleb Panteleev. The third paper is co-authored with Drs. Vladimir Romanovsky, Gennadiy Tipenko and Donald Walker. The forth paper is co-authored with Vladimir Romanovsky, Vladimir Alexeev and David Lawrence. In the final fifth paper, Dr Vladimir Alexeev is the first author, however the majority of numerical computations and parts of the synthesis was performed by the second author, Dmitry Nicolsky. Additional co-authors in the fifth paper are Drs. Vladimir Romanovsky and David Lawrence. In each case my co-authors helped me tremendously by providing guidance, assisting with modeling, acquisition of field data, and editing. As the first author I wrote the first four manuscripts and contributed an overwhelming portion of the work in all five manuscripts.

Bibliography

Brown, J., K. Hinkel, and F. Nelson (2000), The circumpolar active layer monitoring (CALM) program: research designs and initial results, *Polar Geography*, *24*, 163–258.

Burgess, M., S. Smith, J. Brown, V. Romanovsky, and K. Hinkel (2002), *Global Terrestrial Network for Permafrost (GTNet-P): permafrost monitoring contributing to global climate observations*, Geological Survey of Canada, 8 pp., Current Research 2000-E14.

Clow, G., and F. Urban (2002), Largest permafrost warming in northern alaska during the 1990s determined from gtn-p borehole temperature measurements, in *EOS, Transactions of the AGU*, vol. 83(47), p. F258.

Goodrich, W. (1982), The influence of snow cover on the ground thermal regime, *Can. Geotech. J.*, *19*, 421–432.

Kane, D., L. Hinzman, and J. Zarling (1991), Thermal response of the active layer in a permafrost environment to climatic warming, *Cold Reg. Sci. Technol.*, *19*(2), 111–122.

Ling, F., and T. Zhang (2003), Impact of the timing and duration of seasonal snow cover on the active layer and permafrost in the alaskan arctic, *Permafrost Periglac.*, *14*, 141–150.

Marchenko, S., A. Gorbunov, and V. Romanovsky (2007), Permafrost warming in the tien shan mountains, central asia, *Global Planet. Change*, *56*, 311–327.

Mölders, N., and V. Romanovsky (2006), Long-term evaluation of HTSVS frozen ground/permafrost component using observations at barrow, alaska., *J. Geophys. Res.*, *111*, D04105, doi:10.1029/2005JD005957.

Muhll, V., T. Stucki, and W. Haeberli (1998), Borehole temperatures in alpine permafrost: a ten years series, in *Seventh International Conference on Permafrost*, Yellowknife, Canada.

Nelson, F., and S. Outcalt (1987), Anthropogenic geomorphology in northern alaska, *Polar Geography*, *3*(1), 17–48.

Nixon, F., C. Tarnocai, and L. Kutny (2003), Long-term active layer monitoring: Mackenzie valley, northwest canada, in *Eighth International Conference on Permafrost*, vol. 2, edited by M. Phillips, S. Springman, and L. Anderson, pp. 821–826, Balkema, Lisse, Netherlands.

Oberman, N., and G. Mazhitova (2001), Permafrost dynamics in the northeast of european russia at the end of the 20th century, *Norwegian Journal of Geography*, *55*, 241–244.

Oleson, K., et al. (2004), *Technical description of the Community Land Model (CLM)*, NCAR Tech. Note NCAR/TN-461+STR, 173 pp., NCAR.

Osterkamp, T. (2003), Establishing long-term permafrost observatories for active-layerand permafrost investigations in alaska: 1977-2002, *Permafrost Periglac.*, *14*, 331–342.

Pavlov, A., and Moskalenko (2002), The thermal regime of soils in the north of western siberia, *Permafrost Periglac.*, *13*, 43–51.

Romanovsky, V., N. Shender, T. Sazonova, V. Balobaev, G. Tipenko, and Rusakov (2001), Permafrost temperatures in alaska and east siberia: past, present, in *Proceedings of the Seconnd Russian Conference on Geocryology*, pp. 301–314.

Romanovsky, V., M. Burgess, S. Smith, K. Yoshikawa, and J. Brown (2002), Permafrost temperature records: indicator of climate change, *EOS*, *83*(50), 593–594.

Sazonova, T., V. Romanovsky, J. Walsh, and D. Sergueev (2004), Permafrost dynamics in the 20th and 21st centuries along the east siberian transect, *J. Geophys. Res.*, *109*, D01108, doi:10.1029/2003JD003680.

Zhuang, Q., V. Romanovsky, and A. McGuire (2001), Incorporation of a permafrost model into a large-scale ecosystem model: evaluation of temporal and spatial scaling issues in simulating soil thermal dynamics, *J. Geophys. Res.*, *106*, 33,649–33,670.

Chapter 1

Using in-situ temperature measurements to estimate saturated soil thermal properties by solving a sequence of optimization problems[1]

1.1 Abstract

We describe an approach to find an initial approximation to the thermal properties of soil horizons. This technique approximates thermal conductivity, porosity, unfrozen water content curves in horizons where no direct temperature measurements are available. To determine physical properties of ground material, optimization-based inverse techniques are employed to fit the simulated temperatures to the measured ones. Two major ingredients of these techniques are an algorithm to compute the soil temperature dynamics and a procedure to find an initial approximation to the ground properties. In this article we show how to determine the initial approximation to the physical properties and present a new finite element discretization of the heat equation with phase change to calculate the temperature dynamics in soil. We successfully apply the proposed algorithm to recover the soil properties for the Happy Valley site in Alaska using one-year temperature dynamics. The determined initial approximation is utilized to simulate the temperature dynamics over several consecutive years; the difference between simulated and measured temperatures lies within uncertainties of measurements.

1.2 Introduction

Recently, the Arctic Climate Impact Assessment report (*ACIA*, 2004) concluded that climate change is likely to significantly transform present natural environments, particularly across extensive areas in the Arctic and sub-Arctic. Among the highlighted potential transformations is soil warming which can potentially cause an increase in the active layer thickness and degradation of permafrost as well as have broader impacts on soil hydrology, northern ecosystems and infrastructure. Since permafrost is widely distributed and covers approximately 25% of the land surface in the Northern Hemisphere (*Brown et al.*, 1997), it is important to understand the causes affecting the soil temperature regime. One approach to studying soil temperature dynamics and their dependence on climate variability is to employ mathematical modeling (*Goodrich*, 1982; *Nelson and Outcalt*, 1987; *Kane et al.*,

[1] D.J. Nicolsky, V.E. Romanovsky and G.S. Tipenko, 2007, "Using in-situ temperature measurements to estimate saturated soil thermal properties by solving a sequence of optimization problems", published in The Cryosphere, 1: 41-58

1991; *Zhuang et al.*, 2001; *Ling and Zhang*, 2003; *Oleson et al.*, 2004; *Sazonova et al.*, 2004; *Mölders and Romanovsky*, 2006)

A mathematical model of soil freezing/thawing is based on finding a solution of a non-linear heat equation over a specified domain, (see *Andersland and Anderson*, 1978; *Yershov*, 1998, and many references therein). The domain represents ground material and is divided into several horizons (e.g. an organic matt, an organically enriched mineral soil layer, and a mineral soil layer) each with its distinct properties characterized by mineral-chemical composition, texture, porosity, heat capacity and thermal conductivity. By parameterizing the coefficients in the heat equation within each horizon, it is possible to take into account temperature-dependent latent heat effects occurring when ground freezes and thaws. This approach yields a realistic model of temperature dynamics in soils. However, in order to produce quantitatively reasonable results, it is necessary to prescribe physical properties of each horizon.

Conventional Time Domain Reflectometry (*Topp et al.*, 1980) and drying methods are commonly used to estimate soil water content at shallow depths. The Time Domain Reflectometry method is based on measurements of the apparent dielectric constant around a wave guide inserted into the soil. It has been demonstrated that there is a relationship between the apparent dielectric constant and liquid water content (*Topp et al.*, 1980) enabling robust estimations of water content in shallow soils with homogeneous composition. There are some difficulties however in measuring unfrozen water content of coarsely textured, heterogeneous or organically enriched soils in Arctic tundra (*Boike and Roth*, 1997; *Yoshikawa et al.*, 2004). More accurate measurements of the total water content (ice and water together) can be acquired by thermalization of neutrons and gamma ray attenuation. This is not always suitable for Arctic regions as it requires transportation of radioactive equipment to remote locations (*Boike and Roth*, 1997). An alternative to the above-mentioned methods and also to a number of others (*Schmugge et al.*, 1980; *Tice et al.*, 1982; *Ulaby et al.*, 1982; *Stafford*, 1988; *Smith and Tice*, 1988) is the use of inverse modeling techniques. These techniques estimate the water content and other thermal properties of soil using in-situ temperature measurements and by exploiting the mathematical model.

A variety of inverse modeling techniques that recover the thermal properties of soil are known. Many of them rely on the commonly called source methods (*Jaeger and Sass*, 1964), in which temperature response due to heating is measured at a certain distance from the heat source. The temperature response and geometry of the probe are used to

compute the thermal properties by either direct or indirect methods. In the direct methods, the temperature measurements are explicitly used to evaluate the thermal properties. In the indirect methods, one minimizes a discrepancy between the measured and the synthetic temperatures, the latter computed mathematically by exploiting the heat equation in which the coefficients are parameterized according to the specified thermal properties.

Application of direct methods such as the Simple Fourier Methods (*Carson*, 1963), Perturbed Fourier Method (*Hurley and Wiltshire*, 1993), and the Graphical Finite Difference Method (*McGaw et al.*, 1978; *Zhang and Osterkamp*, 1995; *Hinkel*, 1997) yield accurate results for the thermal diffusivity (the ratio of the thermal conductivity and the heat capacity), only when water does not undergo the phase change. Despite the fact that the direct methods are well established for the heat equation without the phase change, no universal framework exists in the case of the soil freezing/thawing because the heat capacity and thermal conductivity depend strongly on the temperature in this case.

A common implementation of the indirect methods uses an analytical or numerical solution of the heat equation to evaluate the synthetic temperature. Due to strong non-linearities, the analytical solution of the heat equation is known only for a limited number of cases (*Gupta*, 2003), whereas numerical solutions are typically computable. Given a numerical solution computed by finite difference (*Samarskii and Vabishchevich*, 1996) or finite element (*Zienkiewicz and Taylor*, 1989) methods, one can minimize a cost function, J, which measures a discrepancy between the measured T_m and synthetic T_c temperatures. The typical expression for the cost function, J, is given by

$$J(\mathcal{C}) \approx \int_{t_s}^{t_e} (T_m(x_i,t) - T_c(x_i,t;\mathcal{C}))^2 dt. \tag{1.1}$$

Here, the quantity $\mathcal{C}$ is the control vector that is a set of parameters defining soil properties of each soil horizon. The synthetic temperature, T_c, is computed by the mathematical model parameterized by variables in $\mathcal{C}$ at some depths x_i over the time interval $[t_s, t_e]$.

In this article, we deal with optimization techniques that find soil properties by minimizing the cost function (1.1). Commonly, the cost function J is minimized iteratively starting from an initial approximation $\mathcal{C}_0$ to the parameters $\mathcal{C}$ (*Thacker and Long*, 1988). Since the heat equation is non-linear, in general there are several local minima. Hence, it is important that the initial approximation lies in the basin of attraction of a proper minimum (*Avriel*, 2003).

We present a semi-heuristic algorithm to determine an initial approximation $\mathcal{C}_0$, for use as the starting point in multivariate minimization of cost functions such as (1.1). In

this article, we use in-situ measured temperature T_m to formulate the cost function J. We construct the initial approximation by minimizing cost functions over specifically selected time intervals $[t_s, t_e]$ in a certain order. For example, first, we propose to find thermal conductivity of the frozen soil using the temperature collected during winter, and then use these values to find properties of the thawed soil. In order to minimize the cost function it is necessary to compute the temperature dynamics multiple times for various control vectors $\mathcal{C}$. Since an analytical solution of the non-linear heat equation is not generally available, we use a finite element method to find its solution. To compute latent heat effects, we propose a new fixed grid technique to evaluate the latent heat terms in the mass (compliance) matrix using enthalpy formulation. Our techniques do not rely on temporal or spatial averaging of enthalpy, but rather evaluate integrals directly by employing a certain change of variables. An advantage of this approach is that it reduces the numerical oscillation of the temperature dynamics at locations near $0°C$ isotherm.

The structure of this chapter is organized as follows. In Section 1.3, we describe a commonly used mathematical model of temperature changes in the active layer and near surface permafrost. In Section 1.4, we outline a finite element discretization of the heat equation with phase change. In Section 1.5, we introduce main definitions, notations and state the variational approach to find the thermal properties. In Section 1.6, we provide an algorithm to construct an initial approximation to thermal properties. In Section 1.7, we apply our method to estimate the thermal properties and the coefficients determining the unfrozen water content at a site located in Alaska. In Section 1.8, we state limitations and shortcomings of the proposed algorithm. Finally, in Section 1.9, we provide conclusions and describe main results.

1.3 Modeling of soil freezing and thawing

For many practical applications, heat conduction is the dominant process, and hence the soil temperature $T, [°C]$ can be simulated by a 1-D heat equation with phase change (*Carslaw and Jaeger*, 1959):

$$C\frac{\partial}{\partial t}T(x,t) + L\frac{\partial}{\partial t}\theta_l(T,x) = \frac{\partial}{\partial x}\lambda\frac{\partial}{\partial x}T(x,t), \tag{1.2}$$

where $x \in [0,l]$, $t \in [0,\tau]$; the quantities $C=C(T,x)$ $[Jm^{-3}K^{-1}]$ and $\lambda=\lambda(T,x)$ $[Wm^{-1}K^{-1}]$ stand for the volumetric heat capacity and thermal conductivity of soil, respectively; L $[Jm^{-3}]$ is the volumetric latent heat of fusion of water, and θ_l is the volumetric liquid water content. We note that this equation is applicable when migration of water is negligible,

there are no internal sources or sinks of heat, frost heave is insignificant, and there are no changes in topography and soil properties in lateral directions. Typically, the heat equation (1.2) is supplemented by Dirichlet, Neumann, or Robin boundary conditions specified at the ground surface, x=0, and at the depth l (*Carslaw and Jaeger*, 1959). In geothermal studies, a Neumann boundary condition is typically set at the depth l. In this study we use the measured temperatures T_u and T_l to set the Dirichlet boundary conditions at depths x=0 and x=l, respectively, i.e. $T(0,t)$=$T_u(t)$, $T(l,t)$=$T_l(t)$. In order to calculate the temperature dynamics $T(x,t)$ at any time $t \in [0,\tau]$, equation (1.2) is supplemented by an initial condition, i.e. $T(x,0)$=$T_0(x)$, where $T_0(x)$ is the temperature at $x \in [0,l]$ at time t=0.

In certain conditions such as waterlogged Arctic lowlands, soil can be considered a porous media fully saturated with water. The fully saturated soil is a multi-component system consisting of soil particles, liquid water, and ice. It is known that the energy of the multi-component system is minimized when a thin film of liquid water (at temperature below $0°C$) separates ice from the soil particles (*Hobbs*, 1974). A film thickness depends on soil temperature, pressure, mineralogy, solute concentration and other factors (*Hobbs*, 1974). One of the commonly used measures of liquid water below freezing temperature is the volumetric unfrozen water content (*Williams*, 1967; *Anderson and Morgenstern*, 1973; *Osterkamp and Romanovsky*, 1997; *Watanabe and Mizoguchi*, 2002). It is defined as the ratio of liquid water volume in a representative soil domain at temperature T to the volume of this representative domain and is denoted by $\theta_l(T)$. There are many approximations to θ_l in the fully saturated soil (*Lunardini*, 1987; *Galushkin*, 1997). The most common approximations are associated with power or exponential functions. Based on our positive experience in *Romanovsky and Osterkamp* (2000), we parameterize θ_l by a power function $\theta_l(T)$=$a|T|^{-b}$; a,b>0 for T<T_*<0°C (*Lovell*, 1957). The constant T_* is called the freezing point depression (*Hobbs*, 1974), and from the physical point of view it means that ice does not exist in the soil if T>T_*. In thawed soils (T>T_*), the amount of water in the saturated soil is equal to the soil porosity η, and hence the function $\theta_l(T)$ can be extended to T>T_* as $\theta_l(T)$=η. Therefore, we assume that

$$\theta_l(T,x)=\eta(x)\phi(T,x), \quad \phi=\begin{cases} 1, & T \geq T_* \\ |T_*|^b|T|^{-b}, & T < T_* \end{cases}, \tag{1.3}$$

where ϕ=$\phi(T,x)$ represents the liquid pore water fraction, and T is in $°C$, see the curve marked by triangles in Figure 1.1. Note that the constants T_* and b are the only parameters

that specify dependence of the unfrozen liquid water content on temperature. For example, small values of b describe the liquid water content in some fine-grained soils, whereas large values of b are related to coarse-grained materials in which almost all water freezes at the temperature T_*. The limiting case in which all water freezes at the temperature T_* is associated with phase change between water and ice (no soil particles). This limiting case is commonly called the classical Stefan problem and is represented by extremely large values of b in (1.3).

We use the following notation and definitions. We abbreviate by letters i, l and s, ice, liquid water, and the soil particles, respectively. We express thermal conductivity λ of the soil and its apparent volumetric heat capacity C_{app} according to (*de Vries*, 1963; *Sass et al.*, 1971) as

$$\lambda(T)=\lambda_s^{\theta_s}\lambda_i^{\theta_i(T)}\lambda_l^{\theta_l(T)}, \quad C_{app}(T)=C(T)+L\frac{d\theta_l(T)}{dT} \tag{1.4}$$

$$C(T) = \theta_i(T)C_i + \theta_l(T)C_l + \theta_s C_s \tag{1.5}$$

where C is called the volumetric heat capacity of the soil. Here, the constants C_k, λ_k, $k\in\{i,l,s\}$ are the volumetric heat capacity and thermal conductivity of the k-th constituent at $0°C$, respectively. The quantity θ_k, $k\in\{i,l,s\}$ is the volume fraction of each constituent. Exploiting the relations $\theta_s=1-\eta$ and $\theta_i=\eta-\theta_l$, we introduce notation for the effective volumetric heat capacities C_f and C_t, and the effective thermal conductivities λ_f and λ_t of soil for frozen and thawed states, respectively. Therefore formulae (1.4) and (1.5) yield

$$C_{app}=C+L\frac{d\theta_l}{dT}, \quad C=C_f(1-\phi)+C_t\phi, \quad \lambda=\lambda_f^{1-\phi}\lambda_t^{\phi}, \tag{1.6}$$

where

$$\lambda_f=\lambda_s^{1-\eta}\lambda_i^{\eta}, \quad \lambda_t=\lambda_s^{1-\eta}\lambda_l^{\eta}, \quad C_f=C_s(1-\eta)+C_i\eta, \quad C_t=C_s(1-\eta)+C_l\eta.$$

For most soils, seasonal deformation of the soil skeleton is negligible, and hence temporal variations in the total soil porosity η for each layer are insignificant. Therefore, the thawed and frozen thermal conductivities for the fully saturated soil satisfy

$$\frac{\lambda_t}{\lambda_f} = \left[\frac{\lambda_l}{\lambda_i}\right]^{\eta}. \tag{1.7}$$

It is important to emphasize that evaporation from the ground surface and from within the upper organic layer can cause partial saturation of upper soil horizons (*Hinzman et al.*, 1991; *Kane et al.*, 2001). Therefore, formula (1.7) need not hold within live vegetation and

organic soil layers, and possibly within organically enriched mineral soil (*Romanovsky and Osterkamp*, 1997).

We approximate the coefficients C_{app}, λ according to (1.6), where the thermal properties λ_f, λ_t, C_f, C_t and parameters η, T_*, b are constants within each soil horizon. Table 1.1 lists typical soil horizon geometry, commonly occurring ranges for the porosity η, thermal conductivity λ_f and the values of b parameterizing the unfrozen water content.

1.4 Solution of the heat equation with phase change

1.4.1 A review of numerical methods

In order to solve the inverse problem one needs to compute a series of direct problems, i.e. to obtain the temperature fields for various combinations of thermal properties. A number of numerical methods (*Javierre et al.*, 2006) exist to compute temperature that satisfies the heat equation with phase change (1.2). These methods vary from the simplest ones which yield inaccurate results to sophisticated ones which produce accurate temperature distributions. The highly sophisticated methods explicitly track a region where the phase change occurs and produce a grid refinement in its vicinity, and therefore take significantly more computational time to obtain temperature dynamics. Implementing such complicated methods is not always necessary, since an extremely accurate solution is not particularly important when the mathematical model describing nature is significantly simplified.

In this subsection, we briefly review several fixed grid techniques (*Voller and Swaminathan*, 1990) that accurately estimate soil temperature dynamics and easily extend to multi-dimensional versions of the heat equation (1.2). These methods provide the solution for arbitrary temperature-dependent thermal properties of the soil and do not explicitly track the area where the phase change occurs. Recall that in soils the phase change occurs at almost all sub-zero temperatures. A cornerstone of the fixed grid techniques is a numerical approximation of the apparent heat capacity C_{app}. A variety of the approximation techniques can be found in (*Voller and Swaminathan*, 1990; *Pham*, 1995) and references therein. In general, two classes of them can be identified. The first class is based on temperature/coordinate averaging (*Comini et al.*, 1974; *Lemmon*, 1979) of the phase change. Here, the apparent heat capacity is approximated by

$$C_{app} = \frac{\partial H}{\partial x}\left(\frac{\partial T}{\partial x}\right)^{-1}, \tag{1.8}$$

where

$$H = \int_0^T C_{app} dT,$$

is the enthalpy. The second class of methods is based on temperature/time averaging (*Morgan et al.*, 1978). In this approach,

$$C_{app} = \frac{H_{current} - H_{previous}}{T_{current} - T_{previous}}, \tag{1.9}$$

where subscripts mark time steps at which the values of H and T are calculated. Although these methods have been presented in the context of large values of b in (1.3), it is noted that they work best in the case of a naturally occurring wide phase change interval. Also, it is important to note that the approximation (1.8) is not accurate for near zero temperature gradients. In the case when the boundary conditions are given by natural variability (several seasonal freezing/thawing cycles), near zero gradients at some depths may occur for some time intervals. Hence, the temperature dynamics calculated by using (1.8) can have large computational errors.

An alternative fixed grid technique can be developed by rewriting the heat equation (1.2) in a new form:

$$\frac{\partial H}{\partial t} = \frac{\partial}{\partial x} \lambda \frac{\partial}{\partial x} T, \quad T = T(H), \tag{1.10}$$

resulting in the enthalpy diffusion method (*Mundim and Fortes*, 1979). Advantages of discretizing (1.10) is that the temperature $T = T(H)$ is a smooth function of enthalpy H and hence one can compute all partial derivatives. However, for soils with a sharp boundary between thawed and completely frozen states, the enthalpy H becomes a multivariate function when temperature T nears T_*. Therefore, solution of (1.10) results in that the front becomes artificially stretched over at least one or even several finite elements.

In this chapter, we propose a fixed grid technique that applies the basic finite element method (*Zienkiewicz and Taylor*, 1989) to equation (1.2). Finite element discretization of

$$L \frac{\partial \theta_l}{\partial t} = L \frac{d\theta_l}{dT} \frac{\partial T}{\partial t}$$

in the left hand side of (1.2) results in

$$\left(\int_{x_0}^{x_1} \psi_i(x) \psi_j(x) L \frac{d\theta_l}{dT}(T(x,t)) dx \right) \frac{dT_j}{dt}, \tag{1.11}$$

where $\psi_i(x)$ and $\psi_i(x)$ are two piecewise linear basis functions at nodes i and j, respectively, $T_j(t)$ is the value of temperature at the j-th node at time t, and $T(x,t) = \sum_i \psi_i(x) T_i(t)$.

We propose to evaluate this type of integrals using the unfrozen liquid water content θ_l as the integration variable, i.e.

$$\int_{x_0}^{x_1} \psi(x) L \frac{d\theta_l}{dT}(T(x,t))dx = L \int_{\theta_0}^{\theta_1} \psi(T(\theta_l,t))d\theta_l, \tag{1.12}$$

where ψ=$\psi_i\psi_j$, and θ_0=$\theta_l(T(x_0,t))$ and θ_1=$\theta_l(T(x_1,t))$. This substitution allows precise computation of the latent-heat effect for arbitrary grid cells, since it is parameterized by the limits of integration θ_0, θ_1, instead of being calculated using the rapidly varying function $\frac{d\theta_l}{dT}(T)$ on the element $[x_0, x_1]$ by a quadrature rule. As a consequence of the proposed substitution, evaluation of the integral in (1.11) may not to yield the right result unless the function $T(\theta_l)$ must be monotonically increasing for all θ_l<η, and $T(x,t)$ be monotonous on $[x_0, x_1]$ at time t. Figure 1.1 shows two instances of the unfrozen water content curves frequently occurring in nature. The curve marked by circles is associated with soils in which free water freezes prior to freezing of the bound liquid water in soil pores. The free water is associated with a vertical line at T=T_* whereas the bound water is represented by a smooth curve at T<T_*. The curve marked by triangles reflects soil in which all water is bounded in soil pores and can be parameterized by (1.3) used in our modeling.

1.4.2 Finite element formulation

Let us consider a triangulation of the interval $[0, l]$ by a set of nodes $\{x_i\}_{i=1}^n$. With each node x_i, we associate a continuous function $\psi_i(x)$ such that $\psi_i(x_j) = \delta_{ij}$. We will refer to $\{\psi_i\}_{i=1}^n$ as the basis functions on the interval $[0, l]$. Hence, the temperature $T(x,t)$ on $[0, l]$ is approximated by a linear combination: $T(x,t)$=$\sum_{i=1}^n T_i(t)\psi_i(x)$, where T_i=$T_i(t)$ is the temperature at the node x_i at the time t. Substituting this linear combination into (1.2), multiplying it by ψ_j and then integrating over the interval $[0, l]$, we obtain a system of differential equations (*Zienkiewicz and Taylor*, 1989):

$$\mathbf{M}(\mathbf{T})\frac{d}{dt}\mathbf{T}(t) = -\mathbf{K}(\mathbf{T})\mathbf{T}(t), \tag{1.13}$$

where $\mathbf{T}\equiv\mathbf{T}(t)$=$[T_1(t)\ T_2(t)\ \ldots T_n(t)]^t$ is the vector of temperatures at nodes $\{x_i\}_{i=1}^n$ at time t. Here, the $n\times n$ matrices $\mathbf{M}(\mathbf{T})$=$\{m_{ij}\}_{ij=1}^n$ and $\mathbf{K}(\mathbf{T})$=$\{k_{ij}\}_{ij=1}^n$ are mass and stiffness matrices, respectively. Entry-wise they are defined as

$$m_{ij} = \int_0^l C(T,x)\psi_i\psi_j dx + L\int_0^l \frac{d\theta_l}{dT}\psi_i\psi_j dx \tag{1.14}$$

$$k_{ij} = \int_0^l \lambda(T,x)\frac{d\psi_i}{dx}\frac{d\psi_j}{dx}dx. \tag{1.15}$$

The fully implicit scheme is utilized to discretize (1.13) with respect to time. Denoting by dt_k the time increment at the k-th moment of time t_k, one has

$$\left[\mathbf{M}^k + dt_k \mathbf{K}^k\right]\mathbf{T}^k = \mathbf{M}^k\mathbf{T}^{k-1}, \quad k > 1 \tag{1.16}$$

where $\mathbf{T}^k = \mathbf{T}(t_k)$, $\mathbf{K}^k$=$\mathbf{K}(\mathbf{T}^k)$, $\mathbf{M}^k$=$\mathbf{M}(\mathbf{T}^k)$. We impose boundary conditions at x=0 and some depth x=l by specifying $T_1(t_k)$=$T_u(t_k)$ and $T_n(t_k)$=$T_l(t_k)$.

Given $\mathbf{T}^{k-1}$, we find the solution $\mathbf{T}^k$ of (1.16) by Picard iteration (*Kolmogorov and Fomin*, 1975). The iteration process starts from the initial guess $\mathbf{T}_0^k = \mathbf{T}^{k-1}$ that is used to compute temperature $\mathbf{T}_1^k$ at the first iteration. At iteration s, we compute $\mathbf{T}_s^k$ and terminate iterations at s_e when a certain convergence condition is met. The value of $\mathbf{T}_s^k$ is used to evaluate the matrices $\mathbf{M}^k{}_s$=$\mathbf{M}(\mathbf{T}_s^k)$, and $\mathbf{K}^k{}_s$=$\mathbf{K}(\mathbf{T}_s^k)$. In turn, these are utilized to compute the $s+1$ iteration $\mathbf{T}_{s+1}^k$ by equating

$$[\mathbf{M}^k{}_s + dt_k \mathbf{K}^k{}_s]\mathbf{T}^k{}_{s+1} - \mathbf{M}^k{}_s\mathbf{T}^{k-1} = 0. \tag{1.17}$$

At each iteration the convergence condition $\max_k |T_k^{s+1}(t_k) - T_k^s(t_k)| \leq \epsilon$ is checked. If it hold, the iterations are terminated at s_e=$s+1$. If the number of iterations exceeds a certain predefined number, the time increment dt_k is halved and the iterations start again. Please, note that the convergence is guaranteed if the time increment dt_k is small enough.

1.4.3 Computation of the mass matrix

One of the obstacles to obtain a finite dimensional approximation that accurately captures the temperature dynamics is related to evaluation of the mass matrix $\mathbf{M}$. Since the basis function ψ_i does not vanish only on the interval $[x_{i-1}, x_{i+1}]$, the matrix $\mathbf{M}$ is tri-diagonal. Therefore, to compute its i-th row we evaluate

$$\int_0^l \frac{d\theta_l}{dT}\psi_j(x)\psi_i(x)dx \quad j = i-1, i, i+1, \tag{1.18}$$

where j stands for the column index. For the sake of brevity, we consider the first integral (j=i−1) in (1.18). This restricts us only to the grid element $[x_{i-1}, x_i]$, yielding

$$\int_0^l \frac{d\theta_l}{dT}\psi_{i-1}(x)\psi_i(x)dx = \int_{x-1}^{x_i} \frac{d\theta_l}{dT}\psi_{i-1}(x)\psi_i(x)dx. \tag{1.19}$$

We recall that in the standard finite element method, the temperature on the interval $[x_{i-1}x_i]$ is approximated by

$$T(x,t)=\psi_{i-1}(x)T_{i-1}(t)+\psi_i(x)T_i(t), \tag{1.20}$$

for any $x \in [x_{i-1}, x_i]$ and fixed moment time t. Here, ψ_i and ψ_{i-1} are piece-wise linear functions satisfying $\psi_{i-1}=1-\psi_i$ on $[x_{i-1}, x_i]$. For all $x \in [x_{i-1}, x_i]$, we can compute the temperature T from (1.20) and values of T_i, T_{i-1}. Note that in the case of $\Delta T_i=0$, we can compute (1.19) directly since $d\theta_l/dT$ is constant over $[x_{i-1}x_i]$. However, if $\Delta T_i=T_i-T_{i-1} \neq 0$, then we can consider an inverse function, that is, x is taken as a function of T to obtain

$$\int_{x_{i-1}}^{x_i} \frac{d\theta_l}{dT}\psi_{i-1}\psi_i dx = \frac{x_i - x_{i-1}}{(\Delta T_i)^3}\int_{x_{i-1}}^{x_i} \frac{d\theta_l}{dT}(T_i - T)(T - T_{i-1})dT$$

Therefore

$$\int_0^l \frac{d\theta_l}{dT}\psi_{i-1}\psi_i \, dx = \frac{x_i - x_{i-1}}{(\Delta T_i)^3}\int_{\theta_{i-1}}^{\theta_i} (T - T_i)(T_{i-1} - T)d\theta, \tag{1.21}$$

where $\theta_{i-1}=\theta_l(T(x_{i-1}, t))$ and $\theta_i=\theta_l(T(x_i, t))$. Note that in (1.21) the temperature T is a function of the liquid water content θ_l, i.e. $T = \theta_l^{-1}(\theta_l)$. Therefore, returning back to (1.18), we have that each of the integrals in (1.18) is a linear combination of the type $\beta_2 A_2 + \beta_1 A_1 + \beta_0 A_0$, where

$$A_k = \int_{\theta_{i-1}}^{\theta_i} [\theta_l^{-1}(z)]^k dz, \quad k = 0, 1, 2.$$

The constants $\{\beta_k\}$ are easily computable if $\theta_l(T)$ is given by (1.3).

1.4.4 Evaluation of the proposed method

To test the proposed method, we compare temperature dynamics computed by the proposed method with an analytical solution of the heat equation (1.2) in which $b \to \infty$. This analytical solution is called Neumann solution (*Gupta*, 2003) and is typically used to verify numerical schemes. In the proposed numerical scheme the mass matrix $\mathbf{M}$ is tri-diagonal, and hence this scheme is called consistent. Other commonly utilized numerical schemes are called mass lumped (*Zienkiewicz and Taylor*, 1989) since they employ the diagonal mass matrix:

$$\mathbf{M} = \text{diag}(C_{app,1}\int_0^1 \psi_1 dx, \ldots, C_{app,n}\int_0^1 \psi_n dx). \tag{1.22}$$

Here, $C_{app,i}$ is the value of the apparent heat capacity C_{app} at the $i-$th node computed either by spatial (1.8) or temporal (1.9) averaging of latent heat effects.

In Figure 1.2, we compare temperature dynamics computed by the proposed consistent and a typical mass lumped scheme. We plot a location of the $0°C$ isotherm for several spatial discretizations, i.e. the distance Δx_i between two neighboring nodes x_i and x_{i-1} is

0.1 or 0.01 meter. In this figure we see that the location of the $0°C$ isotherm calculated by numerical schemes lies within Δx_i bound near the analytical solution. However, temporal dynamics of the location of the $0°C$ isotherm differ among methods. In the solution (squares) computed by the mass lumped approach with temporal enthalpy averaging (TA), dynamics of the $0°C$ isotherm has some irregularities, i.e the freezing front either advancing too fast or too slow. In average, however this algorithm produces good results. Our proposed consistent method (circles) gives a better solution and smoother rate of advancing of the $0°C$ isotherm, see Figure 1.2, left.

In Figure 1.3, we compare temperature dynamics computed by two mass lumped approaches exploiting spatial (1.8) and temporal (1.9) enthalpy averaging. A warm bias in the temperature computed by the spatial averaging of the enthalpy is due to computational errors occurring when the temperature gradient is approximately zero at some depth. Our experience shows that this difference appears regardless of decreasing the tolerance ϵ between iterations in (1.17). We note that in all above numerical experiments a finite element computer code is the same except for a part associated with computation of mass matrix, i.e. consistent (1.18) or mass lumped (1.22). These numerical experiments show that the straight-forward mass lumped schemes are typically inferior to consistent ones.

Since our method (1.14) is based on the consistent approach (the mass matrix $\mathbf{M}$ is the tri-diagonal one), the numerical solution oscillates if the time steps dt_k are too small (*Pinder and Gray*, 1977). For a fixed time step dt_k, the oscillations disappear if the spatial discretization becomes fine, i.e. the inequality $m_{ij}+dt_k k_{ij}<0$ holds when $i\neq j$ (*Ciarlet*, 1978; *Dalhuijsen and Segal*, 1986). It is shown that these oscillations occur due to violation of the discrete maximum principle (*Rank et al.*, 1983). Therefore, to avoid the oscillations in the numerical solution (*Dalhuijsen and Segal*, 1986), we propose either to use sufficiently large time steps (for which the formula can be found in the above cited references) or to exploit the following regularization. We construct a lumped version $\tilde{\mathbf{M}} = \{\tilde{m}_{ij}\}$ of the mass matrix $\mathbf{M}$ given by

$$\tilde{m}_{ii} = \sum_j m_{ij} \tag{1.23}$$

and substitute $\tilde{\mathbf{M}}$ for $\mathbf{M}$ in (1.16). Comparison of temperature dynamics computed employing the proposed consistent $\mathbf{M}$ defined by (1.16) and its mass lumped modification $\tilde{\mathbf{M}}$ defined by (1.23) is shown in Figure 1.4. The numerical oscillations near $0°C$ disappear in the temperature dynamics computed by the proposed mass lumped approach (see Figure 1.4). In Figure 1.5, we compare the proposed mass lumped approach (stars), and the one

based on temporal enthalpy averaging (squares) by (1.8). This figure shows that the numerical scheme using temporal averaging of the enthalpy produces larger oscillation than our solution. This comparison reveals that the proposed mass lumped approach (1.23) reduces some numerical oscillations and follows the "exact" solution (computed by the consistent approach with a fine spatial discretization) more closely than the solution computed by the lumped approach exploiting (1.8).

In conclusion, we state that if a spatial discretization is fine and time steps are sufficiently large (*Pinder and Gray*, 1977) then the consistent schemes do not show numerical oscillations, and hence they should be utilized. In the case of a coarse spatial discretization, consistent schemes can violate the discrete maximum principle, and hence the mass lumped schemes are more attractive. In this work, we construct a fine spatial discretization and use the proposed consistent approach, while restricting the time step t_k from below.

1.5 Variational approach to find the soil properties

In this section, we provide definitions and describe main components of the indirect method used to find the soil properties by minimizing the cost function outlined in (1.1).

We define the control $\mathcal{C}$ as a set consisting of thermal conductivities $\lambda_t^{(i)}, \lambda_f^{(i)}$, heat capacities $C_t^{(i)}, C_f^{(i)}$ and parameters $\eta^{(i)}, T_*^{(i)}, b^{(i)}$ describing the unfrozen water content for each soil horizon $i = 1, \ldots, n$, or

$$\mathcal{C} = \{C_f^{(i)}, C_t^{(i)}, \lambda_t^{(i)}, \lambda_f^{(i)}, \eta^{(i)}, T_*^{(i)}, b^{(i)}\}_{i=1}^{n}, \tag{1.24}$$

where n is the total number of horizons. We say that a solution of the direct problem for the control $\mathcal{C}$ is $T(x,t;\mathcal{C})$ and is defined by the set

$$T(x,t;\mathcal{C}) = \{T(x_i,t) : i = 1, \ldots, m; t \in [0,\tau]\}, \tag{1.25}$$

where $\{x_i\}_{i=1}^m$ is a set of m fixed distinct points on [0,l]. In (1.25), the $T(x_i,t)$ are pointwise values of temperature distributions satisfying (1.2) in which thermal properties of each horizon are given according to $\mathcal{C}$.

The counterpart of $T(x,t;\mathcal{C})$ is the data $T_{\mathcal{D}}(x,t)$ defined by a set of measured temperature at the same depths $\{x_i\}_{i=1}^m$ and the same time interval $[0,\tau]$. Since the data $T_{\mathcal{D}}(x,t)$ and its model counterpart $T(x,t;\mathcal{C})$ are given on the same set of depths and time interval, we can easily compute a discrepancy between them, usually measured by the cost function

$$J(\mathcal{C}) = \frac{1}{m(t_s - t_e)} \sum_{i=1}^{m} \frac{1}{\sigma_i^2} \int_{t_s}^{t_e} (T_{\mathcal{D}}(x_i,t) - T(x_i,t;\mathcal{C}))^2 dt. \tag{1.26}$$

Here, $t_s, t_e \in [0, \tau]$ and σ_i stands for an uncertainty in measurements by the i-th sensor. In our measurements all temperature sensors assume the same precision, so all of $\{\sigma_i\}$ are equal. Given a way to measure this discrepancy as in (1.26) we can finally formulate an inverse problem.

For the given data $T_{\mathcal{D}}(x,t)$, we say that the control $\mathcal{C}_*$ is a solution to an inverse problem if discrepancy between the data and its model counterpart evaluated at $\mathcal{C}_*$ is minimal (*Alifanov*, 1995; *Alifanov et al.*, 1996; *Tikhonov et al.*, 1996). That is,

$$J(\mathcal{C}_*) = \min_{\mathcal{C}} J(\mathcal{C}).$$

To illustrate steps which are necessary to solve this inverse problem and find an optimal $\mathcal{C}_*$ we provide the following example. To formulate the inverse problem one has to have the measured temperatures $T_{\mathcal{D}}(x,t)$. For the sake of this example, we replace the data $T_{\mathcal{D}}(x,t)$ by a synthetic temperature $T_{\mathcal{S}}(x,t) = T(x,t;\mathcal{C}')$ (a numerical solution of the heat equation (1.2) for the known combination $\mathcal{C}'$ of the thermal properties):

$$\mathcal{C}' = \left\{ \begin{array}{l} C_f^{(1)}{=}1.6{\cdot}10^6,\ C_t^{(1)}{=}2.1{\cdot}10^6,\ \lambda_f^{(1)}{=}0.55,\ \lambda_t^{(1)}{=}0.14,\ \eta^{(1)}{=}0.30,\ b^{(1)}{=}0.9,\ T_*^{(1)}{=}{-}0.03 \\ C_f^{(2)}{=}1.7{\cdot}10^6,\ C_t^{(2)}{=}2.3{\cdot}10^6,\ \lambda_f^{(2)}{=}\mathbf{0.90},\ \lambda_t^{(2)}{=}0.66,\ \eta^{(2)}{=}0.30,\ b^{(2)}{=}0.6,\ T_*^{(2)}{=}{-}0.03 \\ C_f^{(3)}{=}1.8{\cdot}10^6,\ C_t^{(3)}{=}2.6{\cdot}10^6,\ \lambda_f^{(3)}{=}1.90,\ \lambda_t^{(3)}{=}1.25,\ \eta^{(3)}{=}\mathbf{0.25},\ b^{(3)}{=}0.8,\ T_*^{(3)}{=}{-}0.03 \end{array} \right\}.$$

The initial and boundary conditions in all calculations are fixed and given by in-situ temperature measurements in 2001 and 2002 at the Happy Valley site located in the Alaskan Arctic. We compute the temperature dynamics for a soil slab with dimensions $[0.02, 1.06]$ between 21 July 2001 and 6 May 2002, and evaluate the cost function at $\{x_i\}_i$={0.10, 0.17, 0.25, 0.32, 0.40, 0.48, 0.55, 0.70, 0.86} meters. Uniformly distributed noise on $[-0.04, 0.04]$ was added to $T_{\mathcal{S}}(x,t)$, to simulate noisy temperature data recorded by sensors (precision of the sensor is $0.04°C$). The boundaries between the horizons lie at 0.10 and 0.20 meter depth.

We find a control $\mathcal{C}'$ that minimizes the cost function J defined by (1.26) in which $T_{\mathcal{D}}(x,t) = T_{\mathcal{S}}(x,t)$. For the sake of simplicity, we assume that all variables in $\mathcal{C}'$ are known except for the pair $\lambda_f^{(2)}$,$\eta^{(3)}$. Therefore, the problem of finding this pair can be solved by minimizing the cost function J on $(\lambda_f^{(2)},\eta^{(3)})$ plane as follows. We compute temperature dynamics for various combinations of $\lambda_f^{(2)}$,$\eta^{(3)}$ and plot isolines of J, see Figure 1.6. The point on $(\lambda_f^{(2)},\eta^{(3)})$ plane where the cost function is minimal gives the sought values of $\lambda_f^{(2)}$ and $\eta^{(3)}$. The location of the minimum coincides with values $\lambda_f^{(2)}$=0.9, $\eta^{(3)}$=0.25, which were used to generate the synthetic data.

In the above example, the control had only two unknown variables $\lambda_f^{(2)}, \eta^{(3)}$ and we minimized the corresponding cost function. Usually, a majority of variables in the control $\mathcal{C}$ is unknown, and hence multivariate minimization is required. Since computation of the cost function for all possible realizations of the control on the discrete grid is extremely time-consuming, various iterative techniques are used (*Fletcher*, 2000).

We note that if the cost function has several minima due to non-linearities of the heat equation (1.2) and if the initial approximation $\mathcal{C}_0$ is arbitrary then the iterative algorithm can converge to an improper minimum. Nevertheless, with the initial approximation $\mathcal{C}_0$ within the basin of attraction of the global minimum, the iterative optimization method should converge to the proper minimum even if the model is nonlinear (*Thacker*, 1989). Consequently, proper determination of an initial approximation $\mathcal{C}_0$ is important.

After selection of the initial approximation $\mathcal{C}_0$, the next step is to minimize the cost function $J(\mathcal{C})$ with respect to all parameters in $\mathcal{C}$. There is a great variety of iterative methods that minimize $J(\mathcal{C})$. The majority of them rely on computation of the gradient $\nabla J(\mathcal{C})$ of the cost function. The computation of $\nabla J(\mathcal{C})$ is a complicated problem and is out of the scope of this chapter. An interested reader is referred to (*Alifanov et al.*, 1996; *Permyakov*, 2004) and to references therein. Since we are primarily concerned with evaluation of the initial approximation to the thermal properties, we use the following universal algorithm to minimize the cost function.

We look for the minimum of the cost function by the simplex search method described in (*Lagarias et al.*, 1998), which is a direct search method (*Bazaraa et al.*, 1993). In a two and three dimensional spaces, the simplex is a triangle or a pyramid, respectively. At each iteration the value of the function computed at the point, being in or near the current simplex, is compared with the function's values at the vertices of the simplex and, usually, one of the vertices is replaced by the new point, giving a new simplex. The iteration processes is continued until the simplex sizes are less than an a priori specified tolerance. At the final iteration, we obtain the set $\mathcal{C}$ of parameters that determine the thermal properties, porosity and coefficients specifying the unfrozen water content for each soil horizon. However, we note that this algorithm typically converges to the minimum slower than other algorithms that require calculations of the gradient (*Dennis and Schnabel*, 1987).

1.6 Selection of an initial approximation

Selection of a proper initial approximation $\mathcal{C}_0$ is an important problem, since the proper choice of $\mathcal{C}_0$ ensures that the minimization procedure converges to a global minimum. In this section, we describe how to select a proper initial approximation by considering several simpler subproblems.

1.6.1 General methodology

We begin by noting that in the natural environment, the thermal properties and the water content are confined within a certain range depending on soil texture and mineralogy. Therefore, the coefficients in (1.2) and hence their initial approximations lie within certain limits. To ensure better determination of the initial approximation $\mathcal{C}_0$, we employ an algorithm similar to coordinate-wise searching method (*Bazaraa et al.*, 1993). In this method, one looks for a minimum along one coordinate, keeping other coordinates fixed, and then looks for the minimum along another coordinate keeping others fixed and so on.

We propose to look for a minimum with respect to some subset of parameters in $\mathcal{C}$, followed by a search along other parameters in $\mathcal{C}$ and so on. In details, our approach is formulated in five steps:

1. Select several time intervals $\{\Delta_k\}$ in the period of observations $[0, \tau]$
2. Associate a certain subset $\mathcal{C}_j$ of parameters $\mathcal{C}$ with each Δ_j. The subset $\mathcal{C}_j$ is such that the temperature dynamics over the period Δ_j is primarily determined by $\mathcal{C}_j$ and depend much less on changes in any other parameters in $\mathcal{C}$.
3. Select a certain pair $\{\Delta_j, \mathcal{C}_j\}$, and look for a location of the minimum of the cost function $J(\mathcal{C})$ keeping all parameters in $\mathcal{C}$ except for $\mathcal{C}_j$ fixed.
4. Update values of $\mathcal{C}_j$ in the control $\mathcal{C}$ by the results obtained at Step 3.
5. Select another pair $\{\Delta_i, \mathcal{C}_i\}$ that is different from the pair $\{\Delta_j, \mathcal{C}_j\}$ at the previous step. Go to Step 3 and repeat for the pair $\{\Delta_i, \mathcal{C}_i\}$.

We continue this iterative processes until the difference between the previous and current values of parameters in $\mathcal{C}$ is below a critical tolerance.

The selected periods Δ_k do not have to coincide with traditional subdivision of a year. The choice of Δ_k is naturally dictated by seasons in the hydrological year, which starts at the

end of summer and consists several seasons. If the period of observations is one year, typical intervals Δ_k are "winter", "summer and fall", "fall" and "extended summer and fall", see Table 1.2. We note that the intervals Δ_k can overlap each other, and quantities t_s and t_e determining lower and upper limits of integration in (1.26) are equal to the beginning and end of the time interval Δ_k. For different geographical regions, the timing for the "winter", "summer and fall" and "fall" can be different. Typical timing of periods $\{\Delta_k\}$ for the North Slope of Alaska is shown in Table 1.2, and are now discussed.

1.6.2 Description of subproblems

Δ_1 : The "winter" period corresponds to the time when the rate of change of the unfrozen liquid water content θ_l is negligibly small; the heat equation (1.2) models the transient heat conduction with thermal properties λ=λ_f, C=C_f, and $\frac{d\theta_l}{dT} \simeq 0$. During the "winter", temperature dynamics depend only on the thermal diffusivity C_f/λ_f of the frozen soil, and hence the simultaneous determination of both parameters C_f and λ_f is an ill-conditioned problem. Assuming that the heat capacity $\{C_f^{(i)}\}$ is known (depending on the soil texture and moisture content we can approximate it using published data), we evaluate the thermal conductivity $\{\lambda_f^{(i)}\}$ and use these values during minimization at other intervals.

Δ_2 : During the "summer and fall" time interval, active phase change of soil moisture occurs. Hence, at this time, see Table 1.2, a contribution of the heat capacity C into the apparent heat capacity C_{app} is negligibly small comparing to the contribution of the latent-heat term $Ld\theta_l/dT$. Therefore, the rate of freezing/thawing primarily depends on the soil porosity η and the thermal conductivity λ (*Tikhonov and Samarskii*, 1963). Thus we approximate $\{C_t^{(i)}\}$ using published data by analyzing the soil texture and moisture content. Note that temperature-dependent latent-heat effects due to the existence of unfrozen water θ_l at this period have a second order of magnitude effect (see discussion below). Therefore, if no prior information about the coefficients b, T_* parameterizing the unfrozen water content is available then they can be prescribed by taking into account the soil texture and analyzing measured temperature dynamics at the beginning of freeze-up (see Figure 1.7). We seek better estimates of b, T_* at the next steps, namely during the "fall" period.

Since, during the "summer and fall" interval, the temperature dynamics primarily depend on the porosity η and thermal conductivity λ, we have to find only $\{\lambda_t^{(j)}, \eta^{(j)}\}$, since $\{\lambda_f^{(j)}\}$ are already found at the previous step, i.e. the "winter" interval. Taking into account the relationship (1.7) between the thermal conductivities for completely frozen and thawed

soil, we approximate

$$\lambda_t^{(j)} = \lambda_f^{(j)} \Big[\frac{\lambda_l}{\lambda_i}\Big]^{\eta^{(j)}}, \qquad j = 2, \ldots, n. \tag{1.27}$$

The water content θ_l in the upper soil horizon changes during the year due to moisture evaporation and precipitation and is not always equal to $\eta^{(1)}$. Hence formula (1.27) does not hold for j=1. Hence, during the "summer and fall" period our goal is to estimate $\{\eta^{(i)}\}_{i=1}^n$ and $\lambda_t^{(1)}$, and then determine thermal conductivity $\lambda_t^{(j)}$ for the rest of soil layers j=2,...,n using (1.27).

Δ_3 : Recall that while evaluating the thermal properties $\{\lambda_t^{(i)}, \lambda_f^{(i)}\}$ and the soil porosity $\{\eta^{(i)}\}$, we assumed that the coefficients $\{b^{(i)}, T_*^{(i)}\}$ are known. However they also have to be determined. We remind that the coefficients $\{b^{(i)}, T_*^{(i)}\}$ cannot be computed prior to calculation of $\{\lambda_t^{(i)}, \lambda_f^{(i)}\}$ and $\{\eta^{(i)}\}$, since $\{b^{(i)}, T_*^{(i)}\}$ are related to the second order effects in temperature dynamics during "summer and fall" and "winter" intervals. Once an initial approximation to $\{\lambda_t^{(i)}, \lambda_f^{(i)}\}$ and $\{\eta^{(i)}\}$ is established, we consider the "fall" period (see Table 1.2) during which the temperature dynamics strongly depend on $\{b^{(i)}, T_*^{(i)}\}$ and allow capturing the second order effects in temperature dynamics (*Osterkamp and Romanovsky*, 1997).

Δ_4 : In the previous three periods, we obtained approximations to all variables $\{\lambda_t^{(i)}$, $\lambda_f^{(i)}$, $C_t^{(i)}$, $C_f^{(i)}$, $\eta^{(i)}$, $b^{(i)}$, $T_*^{(i)}\}$. However, we can improve the approximation by considering the "extended summer and fall" period, see Table 1.2. This period is associated with a time interval when the soil first thaws and then later becomes completely frozen. Since previously, we minimized the cost function depending separately on the porosity $\{\eta^{(i)}\}$ ("summer and fall") and on $\{T_*^{(i)}\}$ ("fall"), we minimize the cost function depending simultaneously on $\{\eta^{(i)}\}$ and $\{T_*^{(i)}\}$ during "extended summer and fall", while other parameters are fixed.

We list in Table 1.2 all steps and time periods Δ_k which are necessary to find the initial approximation. One of the sequences of minimization steps is

"winter" → "summer and fall" → "fall" → "extended summer and fall"

From our experience with this algorithm, we conclude that in some circumstances it is necessary to repeat minimization over some time periods several times, e.g.

"winter" → "summer and fall" → "fall" → "extended summer and fall"
→ "fall" → "extended summer and fall"

until the consecutive iterations modify the thermal properties insignificantly.

1.7 Application. Happy Valley site

1.7.1 Short site description

The temperature measurements were taken in the tussock tundra site located at the Happy Valley ($69°8'N$,$148°50'W$) in the northern foothills of the Brooks Range in Alaska from 22 July 2001 until 22 February 2005. We used data from 22 July 2001 until 15 May 2002 to estimate soil properties, and from 15 May 2002 until 22 February 2005 to validate the estimated properties. The site was instrumented by eleven thermistors arranged vertically at depths of 0.02, 0.10, 0.17, 0.25, 0.32, 0.40, 0.48, 0.55, 0.70, 0.86 and 1.06 meter. The temperature sensors were embedded into a plastic pipe (the MRC probe), that was inserted into a small diameter hole drilled into the ground. The empty space between the MRC and the ground was filled with a slurry of similar material to diminish an impact of the probe to the thermal regime of soil. Our frost heave measurements show that the vertical displacement of the ground versus the MRC probe is negligibly small at this particular installation site. Prior to the installation, all sensors were referenced to $0°C$ in an ice slush bath and have the precision of $0.04°C$. An automatic reading of temperature were taken every five minutes, then averaged hourly and stored in a data logger memory.

During the installation, soil horizons were described and their thicknesses were measured. The soil has three distinct horizons: organic cover, organically enriched mineral soil, and mineral soil. The boundaries between the horizons lie at 0.10 and 0.20 meter depth.

In the all following numerical simulations we consider a slab of ground representing the Happy Valley soil between 0.02 and 1.06 meter depth. For the computational purposes, the upper and lower boundary conditions are given by the observed temperatures at depth of 0.02 and 1.06 meter. Also in all computations, the temperatures are compared with the set of measured temperatures at the depths $\{x_i\}$=$\{0.10, 0.17, 0.25, 0.32, 0.40, 0.48, 0.55, 0.70, 0.86\}$ meter.

1.7.2 Selection of an initial approximation

The "winter" period is associated to the ground temperature below $-5°C$, occurring on 15 January 2002 through 15 May 2002 at the Happy Valley site. The heat capacity C_f for each layer is evaluated based on the soil type, texture and is taken from (*Hinzman et al.*, 1991; *Romanovsky and Osterkamp*, 1995; *Osterkamp and Romanovsky*, 1996).

We estimate λ_f for each layer by looking for a minimum of the cost function J in the 3-D space $\{\lambda_f^{(1)}, \lambda_f^{(2)}, \lambda_f^{(3)}\}$. The minimization problem in this space can be simplified by looking

for a minimum in the following series of 2-D problems. For example, for several physically acceptable values of the thermal conductivity $\lambda_f^{(1)}$, we compute temperature dynamics for various values of $\lambda_f^{(2)}$, $\lambda_f^{(3)}$ and plot isolines of the cost function J. In the series of plots in Figure 1.8, we notice that a location of the minimum on the $(\lambda_f^{(2)}, \lambda_f^{(3)})$ plane shifts as $\lambda_f^{(1)}$ changes. The minimum of the cost function at each cross section is almost the same, and the problem of selecting the right combination of parameters arises. Here, knowledge of the soil structure becomes relevant. It is known that the soil type of the third layer is silt highly enriched with ice, so from Table 1.1 $1.6<\lambda_f^{(3)}<2.0$. Therefore, we select $\lambda_f^{(1)}=0.55$, $\lambda_f^{(2)}=1.0$ and $\lambda_f^{(3)}=1.8$, and use them in all other consecutive steps (see Table 1.3, columns 6,7 and 8). More precise results could be obtained if a sensor measuring the thermal conductivity was placed in at least one of the horizons, see discussion in Section 1.8.

The "summer and fall" period is selected to capture the maximal depth of active layer occurring between 28 August 2001 and 6 December 2001. We take values of the heat capacity C_t from (*Hinzman et al.*, 1991; *Romanovsky and Osterkamp*, 1995; *Osterkamp and Romanovsky*, 1996). Comparing measured temperatures to the ones computed for $\lambda_t^{(1)}$, $\{\eta^{(i)}\}_{i=1}^3$ varying within a range of their natural variability, we found that $\lambda_t^{(1)} \in [0.09, 0.15]$, $\eta^{(1)} \in [0.3, 0.9]$, $\eta^{(2)} \in [0.3, 0.9]$ and $\eta^{(3)} \in [0.15, 0.45]$. Once the variability of these parameters is found, we search for a minimum of the cost function in the 4-D space $\{\lambda_t^{(1)}, \eta^{(1)}, \eta^{(2)}, \eta^{(3)}\}$, where each parameter varies within the found boundaries. We note that during minimization of J in this 4-D space, other variables in $\mathcal{C}$ are fixed and their values are listed in 1^{st} "Summer and Fall" row in Table 1.3. For example, values of the thermal conductivity $\lambda_f^{(1)}=0.55$, $\lambda_f^{(2)}=1.0$ and $\lambda_f^{(3)}=1.8$ are obtained at the previous step after minimization over the "winter" interval. Also, an approximation to the coefficients $b^{(i)}=0.7, T_*^{(i)}=-0.03, i=1,2,3$ in (1.3) is obtained by analyzing soil texture and type, and dynamics of the measured temperatures near $0°C$, see Figure 1.7. We emphasize that the approximation to the parameters b and T_* is tentative and is going to be improved during the consequent steps.

We note that it is not necessary to find a minimum in the four dimensional space accurately but rather only to estimate its location as significant uncertainties in other parameters still exist. Therefore, we look for the minimum by evaluating the cost function on $(\lambda_t^{(1)}, \eta^{(1)})$, $(\eta^{(1)}, \eta^{(2)})$ and $(\eta^{(2)}, \eta^{(3)})$ planes as follows.

First, we set $\eta^{(1)}=0.6$, $\eta^{(2)}=0.6$, $\eta^{(3)}=0.3$ and $\lambda_t^{(1)}=0.12$, which correspond to the middle of their variability ranges. Then, we evaluate the cost function J on the $(\lambda_t^{(1)}, \eta^{(1)})$ plane,

by varying $\lambda_t^{(1)}, \eta^{(1)}$ in the control, while all other variables in $\mathcal{C}$ are fixed. In the left plot in Figure 1.9, we plot isolines of J on all three planes $(\lambda_t^{(1)}, \eta^{(1)})$, $(\eta^{(1)}, \eta^{(2)})$, and $(\eta^{(2)}, \eta^{(3)})$.

At the $(\lambda_t^{(1)}, \eta^{(1)})$ plane, the cost function attains its minimal value on a boundary of this plane, see Figure 1.9, upper left, and is minimal in the center of the planes $(\eta^{(1)}, \eta^{(2)})$, $(\eta^{(2)}, \eta^{(3)})$. The last two planes allows us to find that $\eta^{(1)}$=0.6, $\eta^{(2)}$=0.55 and $\eta^{(3)}$=0.27, whereas contours at the first plane show that the value of $\lambda_t^{(1)}$ lies between 0.11 and 0.13, see Figure 1.9, left column. We suppose that $\lambda_t^{(1)}$ is 0.12 and proceed further. After updating the control with the computed values, we evaluate the cost function on the same set of planes one more time; parameters in the control before minimization are shown in Table 1.3 the "Summer and Fall" 2^{nd} row. After computing the cost function, we draw its isolines and show them in Figure 1.9, right. Note that at this step the cost function attains its minima located in the center of the computational grid. We update the control with $\eta^{(1)}$=0.6, $\eta^{(2)}$=0.55, $\eta^{(3)}$=0.27, $\lambda_t^{(1)}$=0.12. Note that the location of the minimum did not change significantly. Our experience shows that changes of soil properties by 5%-10% or less are insignificant, since the corresponding difference in soil temperatures is comparable with uncertainties of measurements. Therefore, we do not have to do additional iterations on the same set of planes, and we proceed to the next step and reduce uncertainties in coefficients T_* and b.

For the sake of brevity, we omit details in consequent steps associated with "fall" and "extended summer and fall" intervals, since the search of parameters is completed similar to as described in the "summer and fall" step. We emphasize that we are just interested in calculation of an initial approximation to the control which could serve as a starting point in the global minimization of the cost function. By no means, do we try to substitute the global minimization by this heuristic procedure. However, a good starting point can save computational time and improve accuracy of a final result.

1.7.3 Global minimization and sensitivity analysis

While evaluating an initial approximation, we sought minima of the cost functions $J(\mathcal{C})$ measuring discrepancy over periods $\{\Delta_k\}$. In this subsection, we perform global minimization of the cost function with respect to all parameters in $\mathcal{C}$ over the entire period of measurements 22 July 2001 until 15 May 2002 used for calibration. Also, we analyze sensitivity of an initial approximation derived from minimizing the cost function globally with respect to all parameters.

In global minimization problems, a starting point from which iterations begin is given by the initial approximation evaluated in the previous subsection, see Table 1.3, the last row. As a result of global minimization problem, we obtain the parameters (thermal properties, porosity and coefficients specifying the unfrozen water content for each soil horizon) which can depend on values t_s and t_e determining the period over which discrepancy between observed and modeled temperatures is measured. In global minimization problems, the constant t_e is associated with an end of "winter" interval during which the soil is completely frozen. But since, the soil is frozen for several months for a cold permafrost region, the cost function does not significantly depend on t_e if t_e varies within two week limits. However, the value of t_s is associated with beginning of "summer and fall" interval during which the ground is thawed. Since, the ground is thawing during a relatively short period of time for cold permafrost regions, we consider several values of t_s and minimize the cost function with respect to all parameters.

Results of minimization are listed in Table 1.4. It shows that the results of global minimization do not significantly depend on constants t_s, if the interval $[t_s, t_e]$ represents thawed and frozen states of the soil. Using averaged values of the thermal properties, we compute the temperature dynamics for the entire period of observations. Comparison of the calculated and measured temperatures at different depths and at time intervals used for calibration are shown in Figure 1.10,1.11 and 1.12. During the winter, the calculated temperature closely follows the observed temperature within the uncertainty of thermistor measurements. During the summer, the difference between the measured and calculated temperatures is larger but does not exceed $0.3°C$ for sensors in the mineral soil. This larger discrepancy between the measured and computed temperatures can be partially explained by over-simplifying physics and neglecting water dynamics in the upper organic horizons.

Finally, in order to show that the found initial approximation (the last row in Table 1.3) lies close to the true values of soil properties, we use it to compute the soil temperature dynamics through 22 February 2005. Note that the time interval from 22 May 2002 until 22 February 2005 was not used to find the soil properties. In Figure 1.13, we plot the measured and calculated temperature dynamics at 0.55 meter depths. The plots with solid symbols mark temperature dynamics computed for the found initial approximation, and for the best guess values (in the middle of the variability range, shown in Table 1.1). We note that the guessed values are used to provide benchmark temperature dynamics against which we show the effectiveness of our approach. The benchmark temperature is much warmer during

summer, and the freeze-up occurs several days later than in the measured temperature. The benchmark temperature dynamics during winter closely follow the measured temperature dynamics, since the middle of the variability range, for which the benchmark temperature was computed, almost matches the found initial approximation. The difference between the measured temperature dynamics and the one calculated for the found initial approximation is typically less than $0.25°C$.

1.8 Discussion and limitation of the proposed method

We concentrate on finding soil thermal properties by minimizing the multivariate cost function J. There are many well known methods that find a minimum of J, including stochastic, heuristic and gradient type algorithms (*Goldberg*, 1989; *Fletcher*, 2000; *Robert and Casella*, 2004). Since we focus on a gradient type algorithm, a special care is necessary to select the initial approximation to the soil properties. For example, if the gradient type algorithm is started outside the basin of attraction of the proper minimum, then due to existence of multiple local minima it can converge to physically non-realistic combination of parameters in $\mathcal{C}$. Stochastic and heuristic algorithms can possibly avoid the problem of selecting the initial approximation, since they are not get trapped in a neighborhood of the local minimum. However, a quality control of soil properties recovered by either stochastic or heuristic algorithm arises. For example, it is feasible that several local minima can have the same value and correspond to substantially different combinations of parameters in the control vector $\mathcal{C}$. Thus, straight forward application of these algorithms can result in soil properties that are different from the physically realistic soil properties several fold.

We find an initial approximation to the thermal properties. This initial approximation can be later used in gradient type algorithm both as a starting point and a regularization. We admit that we find one of the possible realizations for the initial approximations. However, in the process of its computation, we obtain limiting boundaries on parameters in $\mathcal{C}$ which can constrain multivariate minimization, independent on the type of algorithm, i.e. stochastic, heuristic, or the gradient type.

We describe a technique to find an initial approximation to the thermal properties of soil horizons. This technique approximates the thermal conductivity, porosity, unfrozen water content curve in horizons where no direct temperature measurements are available. One of the limitations is that it requires values of heat capacities, since at certain time periods it is possible to estimate thermal diffusivity only but not thermal conductivity and heat

capacity separately.

Since, due to a short distance between points at which the upper and lower boundary conditions are specified, there is uncertainty in evaluation of the thermal conductivity for the frozen ground. This uncertainty is related to a progressive lag in the phase of the temperature wave, defined by the Second Fourier Law (*Carslaw and Jaeger*, 1959). The longer the lag, the better the thermal conductivity can be estimated. For the Happy Valley site, the temperature lag at 1 meter depth is about 10 days. Our experience suggests that the 20-30 day time lag is adequate to estimate thermal conductivity robustly. In the case of shorter time lags, we advocate placing of a thermal conductivity sensor in the mineral soil horizon. The thermal conductivity sensor consists of a heating element and a thermocouple embedded in a needle. More information regarding the sensor can be found in (*Thermal Logic*, 2001) and in references therein. One of the limitations on usage of the thermal conductivity sensor is that it generates correct values of the thermal conductivity for thawed or completely frozen soil in which active phase change processes do not occur.

It should be noted that recovery of the thermal properties of the organic cover (e.g. moss layer) is given as an integrated approach in the following sense. Complex physical processes occurring in the organic cover that include non-conductive heat transfer (*Kane et al.*, 2001) are taken into account by estimating some effective thermal properties which are constants for the entire season. We acknowledge that the estimated thermal properties of the organic layer could be different in nature, but we recover them in such a way that the temperature in the active layer and permafrost should correspond to the measured one.

In the proposed model we used 1-D assumption regarding the heat diffusion in the active layer, which sometimes is not applicable due to hummocky terrain in the Arctic tundra. Another assumption used in the model is that frost heave and thaw settlement is negligibly small and there is no ice lens formation in the ground during freezing. Therefore, the proposed method could be only applied where these assumption are satisfied.

The proposed method allows computation of a volumetric content η of water which changes its phase during freezing or thawing. Water content of liquid water that is tightly bound to soil particles and is not changing its phase can not be estimated, see Figure 1.1.

1.9 Conclusions

We present a technique to calculate an approximation to the soil thermal properties, porosity, and parametrization of the unfrozen water content in order to use it in gradient type

iterative minimization methods both as a starting point and as a regularization. To compute the approximation, we minimize the multivariate cost function describing discrepancy between the measured and calculated temperatures over a certain time interval. We find the minimum by adopting a coordinate-wise iterative search technique to the specifics of our inverse problem. At each iteration, we select a particular set of soil properties and associate with them a certain time interval over which we minimize the cost function. After employing the proposed sequence of iterations, it is possible to find the approximation to all thermal properties and soil porosity.

Although there are several limitations to the proposed approach, we applied it to recover soil properties for Happy Valley site near Dalton highway in Alaska. The difference between the simulated and measured temperature dynamics over the periods of calibration is typically less than $0.3°C$. The difference between the simulated and measured temperatures over the consecutive time interval not used in calibration is less than $0.5°C$ which shows a good agreement with measurements, and validates that the found initial approximation lies close to the true values of soil properties.

In order to compute the cost function, it is necessary to calculate the soil temperature dynamics. Therefore, we developed a new finite element discretization of the Stefan-type problem on fixed coarse grids using enthalpy formulation. One of the advantages of the new method is that it allows computation of the temperature dynamics for the classical Stefan problem without any smoothing of the enthalpy. Also, new approach shows equal or better performance compared to other finite element models of the ground thawing and freezing processes.

1.10 Acknowledgements

We would like to thank J. Stroh, S. Marchenko, A. Kholodov, and P. Layer for all their advice, critique and reassurances along the way. We are thankful to reviewers and the editor for valuable suggestions making the manuscript easier to read and understand. This research was funded by ARCSS Program and by the Polar Earth Science Program, Office of Polar Programs, National Science Foundation (OPP-0120736, ARC-0632400, ARC-0520578, ARC-0612533, IARC-NSF CA: Project 3.1 Permafrost Research), by NASA Water and Energy Cycle grant, and by the State of Alaska.

Bibliography

ACIA (2004), *Impacts of a Warming Arctic: Arctic Climate Impact Assessment*, 139 pp., Cambridge University Press.

Alifanov, O. (1995), *Inverse Heat Transfer Problems*, 348 pp., Springer-Verlag, Berlin.

Alifanov, O., E. Artyukhin, and S. Rumyantsev (1996), *Extreme Methods for Solving Ill-Posed Problems with Application to Inverse Heat Transfer Problems*, 306 pp., Begell House, New York.

Andersland, O., and D. Anderson (1978), *Geotechnical Engineering for Cold Regions*, 566 pp., McGraw-Hill.

Anderson, D., and N. Morgenstern (1973), Physics, chemistry and mechanics of frozen ground: a review, in *Proceedings of the 2nd International Conference on Permafrost*, pp. 257–288, Yakutsk, USSR.

Avriel, M. (2003), *Nonlinear Programming: Analysis and Methods*, 554 pp., Dover Publications.

Bazaraa, M., H. Sherali, and C. M. Shetty (1993), *Nonlinear Programming: Theory and Algorithms*, 2nd ed., 656 pp., Wiley.

Boike, J., and K. Roth (1997), Time domain reectometry as a field method for measuring water content and soil water electrical conductivity at a continuous permafrost site, *Permafrost Periglac.*, *8*, 359–370.

Brown, J., O. Ferrians, J. J. Heginbottom, and E. Melnikov (1997), Circum-arctic map of permafrost and ground-ice conditions, U.S. Geological Survey Circum-Pacific Map CP-45, 1:10,000,000, Reston, Virginia.

Carslaw, H., and J. Jaeger (1959), *Conduction of Heat in Solids*, 520 pp., Oxford University Press, London.

Carson, J. (1963), Analysis of soil and air temperatures by fourier techniques, *J. Geophys. Res.*, *68*, 2217–2232.

Ciarlet, P. (1978), *The Finite Element Method for Elliptic Problems*, 530 pp., North-Holland, Amsterdam.

Comini, G., S. D. Giudice, R. Lewis, and O. Zienkiewicz (1974), Finite element solution of non-linear heat conduction problems with special reference to phase change, *Int. J. Numer. Meth. Eng.*, *8*, 613–624.

Dalhuijsen, A., and A. Segal (1986), Comparison of finite element techniques for solidification problems, *Int. J. Numer. Meth. Eng.*, *23*, 1807–1829.

de Vries, D. (1963), *W.R. van Wijk (editor) Physics of the Plant Environment*, chap. Thermal properties of soils, pp. 210–235, Wiley, New York.

Dennis, J., and R. Schnabel (1987), *Numerical Methods for Unconstrained Optimization and Nonlinear Equations*, 394 pp., Prentice-Hall.

Fletcher, R. (2000), *Practical Methods of Optimization*, 450 pp., Wiley.

Galushkin, Y. (1997), Numerical simulation of permafrost evolution as a part of sedimentary basin modeling: permafrost in the pliocene-holocene climate history of the urengoy field in the west siberian basin, *Can. J. Earth Sci.*, *34*, 935–948.

Goldberg, D. (1989), *Genetic Algorithms in Search, Optimization, and Machine Learning*, 432 pp., Addison Wesley.

Goodrich, W. (1982), The influence of snow cover on the ground thermal regime, *Can. Geotech. J.*, *19*, 421–432.

Gupta, S. (2003), *The Classical Stefan Problem*, 404 pp., Elsevier, Amsterdam.

Hinkel, K. (1997), Estimating seasonal values of thermal diffusivity in thawed and frozen soils using temperature time series, *Cold Reg. Sci. Technol.*, *26*, 1–15.

Hinzman, L., D. Kane, R. Gleck, and K. Everett (1991), Hydrological and thermal properties of the active layer in the alaskan arctic, *Cold Reg. Sci. Technol.*, *19*, 95–110.

Hobbs, P. (1974), *Ice Physics*, 856 pp., Claredon Press, Oxford.

Hurley, S., and R. J. Wiltshire (1993), Computing thermal diffusivity from soil temperature measurements, *Computers and Geosciences*, *19*, 475–477.

Jaeger, J. C., and J. H. Sass (1964), A line source method for measuring the thermal conductivity and diffusivity of cylindrical specimens of rock and other poor conductors, *J. Appl. Phys.*, *15*, 1187–1194.

Javierre, E., C. Vuik, F. Vermolen, and S. van der Zwaag (2006), A comparison of numerical models for one-dimensional stefan problems, *J. Comput. Appl. Math.*, *192*(2), 445–459.

Kane, D., L. Hinzman, and J. Zarling (1991), Thermal response of the active layer in a permafrost environment to climatic warming, *Cold Reg. Sci. Technol.*, *19*(2), 111–122.

Kane, D., K. Hinkel, D. Goering, L. Hinzman, and S. Outcalt (2001), Non-conductive heat transfer associated with frozen soils, *Global Planet. Change*, *29*, 275–292.

Kolmogorov, A., and S. Fomin (1975), *Introductory Real Analysis*, 403 pp., Prentice-Hall, New York.

Lagarias, J., J. Reeds, M. Wright, and P. Wright (1998), Convergence properties of the nelder-mead simplex method in low dimension, *SIAM J. Optimiz.*, *9*(1), 112–147.

Lemmon, E. (1979), *R.W. Lewis and K. Morgan (ed.), Numerical Methods in Thermal Problems*, chap. Phase change technique for finite element conduction code, pp. 149–158, Pineridge Press, Swansea, UK.

Ling, F., and T. Zhang (2003), Impact of the timing and duration of seasonal snow cover on the active layer and permafrost in the alaskan arctic, *Permafrost Periglac.*, *14*, 141–150.

Lovell, C. (1957), Temperature effects on phase composition and strength of partially frozen soil, *Highway Research Board Bulletin*, *168*, 74–95.

Lunardini, V. (1987), *Freezing of soil with an unfrozen water content and variable thermal properties*, CRREL Report, vol. 88-2, 30 pp., US Army Cold Regions Research and Engineering Lab.

Mölders, N., and V. Romanovsky (2006), Long-term evaluation of HTSVS frozen ground/permafrost component using observations at barrow, alaska., *J. Geophys. Res.*, *111*, D04105, doi:10.1029/2005JD005957.

McGaw, R. W., S. I. Outcalt, and E. Ng (1978), Thermal properties of wet tundra soils at barrow, alaska, in *Proceedings of 3rd International Conference on Permafrost*, vol. 1, pp. 47–53, National Research Council of Canada, Ottawa,Canada.

Morgan, K., R. Lewis, and O. Zienkiewicz (1978), An improved algorithm for heat conduction problems with phase change, *Int. J. Numer. Meth. Eng.*, *12*, 1191–1195.

Mundim, M., and M. Fortes (1979), *R.W. Lewis and K. Morgan (ed.), Numerical Methods in Thermal Problems*, vol. 6, chap. Evaluation of finite element method utilized in the solution of solid-liquid phase change problems, pp. 90–100, Pineridge Press, Swansea, UK.

Nelson, F., and S. Outcalt (1987), Anthropogenic geomorphology in northern alaska, *Polar Geography*, *3*(1), 17–48.

Oleson, K., et al. (2004), *Technical description of the Community Land Model (CLM)*, NCAR Tech. Note NCAR/TN-461+STR, 173 pp., NCAR.

Osterkamp, T., and V. Romanovsky (1996), Characteristics of changing permafrost temperatures in the alaskan arctic, usa, *Arctic Alpine Res.*, *28*, 267–273.

Osterkamp, T., and V. Romanovsky (1997), Freezing of the active layer on the coastal plain of the alaskan arctic, *Permafrost Periglac.*, *8*(1), 23–44.

Permyakov, P. (2004), Methods of determining the characteristics of dispersed media at a phase transition, *Russian Physics Journal*, *47*(3), 240–246.

Pham, Q. (1995), Comparison of general-purpose finite element methods for the stefan problem, *Numer. Heat Tr. B-Fund.*, *27*(4), 417–435.

Pinder, G., and W. Gray (1977), *Finite Element Simulation in Surface and Subsurface Hydrology*, 295 pp., Academic Press, New York.

Rank, E., C. Katz, and H. Werner (1983), On the importance of the discrete maximum principle in transient analysis using finite element methods, *Int. J. Numer. Meth. Eng.*, *19*, 1771–1782.

Robert, C., and G. Casella (2004), *Monte Carlo Statistical Methods*, 645 pp., Springer-Verlag.

Romanovsky, V., and T. Osterkamp (1995), Interannual variations of the thermal regime of the active layer and near-surface permafrost in northern alaska, *Permafrost Periglac.*, *6*, 313–335.

Romanovsky, V., and T. Osterkamp (1997), Thawing of the active layer on the coastal plain of the alaskan arctic, *Permafrost Periglac.*, *8*, 1–22.

Romanovsky, V., and T. Osterkamp (2000), Effects of unfrozen water on heat and mass transport processes in the active layer and permafrost, *Permafrost Periglac.*, *11*, 219–239.

Samarskii, A., and P. Vabishchevich (1996), *Computational Heat Transfer, Mathematical Modeling*, vol. 1, 418 pp., Wiley.

Sass, J., A. Lachenbruch, and R. Munroe (1971), Thermal conductivity of rocks from measurements on fragments and its application to heat-flow determinations, *J. Geophys. Res.*, *76*(14), 3391–3401.

Sazonova, T., V. Romanovsky, J. Walsh, and D. Sergueev (2004), Permafrost dynamics in the 20th and 21st centuries along the east siberian transect, *J. Geophys. Res.*, *109*, D01108, doi:10.1029/2003JD003680.

Schmugge, T., T. Jackson, and H. McKim (1980), Survey of methods for soil moisture determination, *Water Resour. Res.*, *16*(6), 961–979.

Smith, M., and A. Tice (1988), *Measurement of the unfrozen water content of soilscomparison of NMR and TDR methods*, CRREL Report, vol. 88-18, 16 pp., US Army Cold Regions Research and Engineering Lab.

Stafford, J. (1988), Remote, non-contact and in-situ measurement of soil moisture content: a review, *J. Agr. Eng. Res.*, pp. 151–172.

Thacker, W. (1989), The role of the hessian matrix in fitting models to measurements, *J. Geophys. Res.*, *94*, 6177–6196.

Thacker, W., and R. Long (1988), Fitting dynamics to data, *J. Geophys. Res.*, *93*(2), 1227–1240.

Thermal Logic (2001), *Thermal conductivity sensor user's manual*, 25pp., PO Box 781, Pullman, WA, 99163, 3 ed.

Tice, A., J. Oliphant, Y. Nakano, and T. Jenkins (1982), *Relationship between the ice and unfrozen water phases in frozen soil as determined by pulsed nuclear magnetic resonance and physical desorption data*, CRREL Report, Vol. 82-15, 12 pp., US Army Cold Regions Research and Engineering Lab.

Tikhonov, A., and A. Samarskii (1963), *Equations of Mathematical Physics*, 776 pp., Pergamon.

Tikhonov, A., A. Leonov, and A. Yagola (1996), *Nonlinear Ill-Posed Problems*, 392 pp., Chapman & Hall, London.

Topp, G. C., J. L. Davis, and A. P. Annan (1980), Electromagnetic determination of soil water content: measurements in coaxial transmission lines, *Water Resour. Res.*, *16*, 574–582.

Ulaby, F., R. Moore, and A. Fung (1982), *Microwave Remote Sensing*, vol. 2, 1064 pp., Addison-Wesley, Reading, MA.

Voller, V., and C. Swaminathan (1990), Fixed grid techniques for phase change problems: a review, *Int. J. Numer. Meth. Eng.*, *30*, 875–898.

Watanabe, K., and M. Mizoguchi (2002), Amount of unfrozen water in frozen porous media saturated with solution, *Cold Reg. Sci. Technol.*, *34*, 103–110.

Williams, P. (1967), *Properties and behaviour of freezing soils*, 120 pp., Norwegian Geotechnical Institute, Publ. 72.

Yershov, E. (1998), *General Geocryology*, 604 pp., Cambridge University Press, Cambridge.

Yoshikawa, K., P. Overduin, and J. Harden (2004), Moisture content measurements of moss (sphagnum spp.) using commercial sensors, *Permafrost Periglac.*, *15*, 309–318.

Zhang, T., and T. E. Osterkamp (1995), Considerations in determining the thermal diffusivity from temperature time series using finite difference methods, *Cold Reg. Sci. Technol.*, *23*, 333–341.

Zhuang, Q., V. Romanovsky, and A. McGuire (2001), Incorporation of a permafrost model into a large-scale ecosystem model: evaluation of temporal and spatial scaling issues in simulating soil thermal dynamics, *J. Geophys. Res.*, *106*, 33,649–33,670.

Zienkiewicz, O., and R. Taylor (1989), *The Finite Element Method*, vol. 1, 648 pp., McGraw-Hill, London.

Table 1.1: A typical thickness of soil layers and commonly occurring range of thermal properties in a cryosol soil on the North Slope, Alaska.

Layer	Layer thickness	Thermal conductivity in the frozen state, λ_f	Porosity, η	Coefficient in (1.3) b
Moss or organic layer	0.05	$[0.1, 0.7]$	$[0.1, 0.7]$	$[1.0, 0.5]$
Mineral-organic mixture	0.20	$[0.9, 1.6]$	$[0.2, 0.6]$	$[0.8, 0.5]$
Mineral soil	> 1.0	$[1.3, 2.4]$	$[0.2, 0.4]$	$[0.7, 0.5]$

Table 1.2: Typical choice of parameters in the control $\mathcal{C}$ for "cold" permafrost regions.

Periods	$\mathcal{C}_j$	Typical Δ_k	Characteristic	Step
"Winter"	$\{\lambda_f^{(i)}\}$	December-April	Completely frozen ground, $T < -5°C$	1
"Summer and Fall"	$\{\eta^{(i)}\}, \lambda_t^{(1)}$	May-November	Developing/-ed active layer and its freezing	2
"Fall"	$\{b^{(i)}, T_*^{(i)}\}$	September-December	Active layer freezing, $T > -5°C$	3
"Extended Summer and Fall"	$\{\eta^{(i)}, T_*^{(i)}\}$	May-January	Developing/-ed active layer and its freezing	4

Table 1.3: Values of parameters in the control at the beginning of each minimization step. The listed steps are typical to recover the initial approximation to the soil properties. The parameters which values are in the parenthesis with the same subindex define minimization plane. For example, in the third row $\lambda_t^{(1)}$ and $\eta^{(1)}$ are in the parenthesis and have the same subindex equal to 1. Therefore, this pair define a minimization plane $(\lambda_t^{(1)}, \eta^{(1)})$. On this plane we minimize the cost function depending on $\lambda_t^{(1)}$ and $\eta^{(1)}$, while value of other parameters are fixed and given in other sections of the current row.

Iterations	$\eta^{(1)}$	$\eta^{(2)}$	$\eta^{(3)}$	$\lambda_t^{(1)}$	$\lambda_f^{(1)}$	$\lambda_f^{(2)}$	$\lambda_f^{(3)}$	$b^{(1)}$	$b^{(2)}$	$b^{(3)}$	$T_*^{(1)}$	$T_*^{(2)}$	$T_*^{(3)}$
Winter	0.40	0.70	0.25	0.10	-	-	-	0.7	0.7	0.7	−0.03	−0.03	−0.03
Summer and Fall, 1^{st}	$(0.60)_{1,2}$	$(0.60)_{2,3}$	$(0.30)_3$	$(0.12)_1$	0.55	1.00	1.80	0.7	0.7	0.7	−0.03	−0.03	−0.03
Summer and Fall, 2^{nd}	$(0.60)_1$	$(0.55)_{1,2}$	$(0.27)_{2,3}$	$(0.12)_3$	0.55	1.00	1.80	0.7	0.7	0.7	−0.03	−0.03	−0.03
Fall, 1^{st}	0.60	0.55	0.27	0.12	0.55	1.00	1.80	$(0.7)_1$	$(0.7)_2$	$(0.7)_3$	$(-0.03)_1$	$(-0.03)_2$	$(-0.03)_3$
Fall, 2^{nd}	0.60	0.55	0.27	0.12	0.55	1.00	1.80	$(0.7)_1$	$(0.6)_2$	$(0.75)_3$	$(-0.03)_1$	$(-0.03)_2$	$(-0.03)_3$
Ext. Summer and Fall 1^{st}	$(0.60)_1$	$(0.55)_2$	$(0.27)_3$	0.12	0.55	1.00	1.80	0.65	0.6	0.75	$(-0.02)_1$	$(-0.03)_2$	$(-0.03)_3$
Ext. Summer and Fall 2^{nd}	$(0.70)_1$	$(0.55)_2$	$(0.27)_3$	0.12	0.55	1.00	1.80	0.65	0.6	0.75	$(-0.025)_1$	$(-0.03)_2$	$(-0.03)_3$
Final Result	0.70	0.55	0.27	0.12	0.55	1.00	1.80	0.65	0.6	0.75	−0.025	−0.025	−0.03

Table 1.4: Global minimization with respect to all parameters in the control. Each realization is specified by the time interval $[t_s, t_e]$ over which the discrepancy between the data and computed temperature dynamics is evaluated. In all case, the constant t_e is 15 May 2002.

t_s	$\eta^{(1)}$	$\eta^{(2)}$	$\eta^{(3)}$	$\lambda_t^{(1)}$	$\lambda_f^{(1)}$	$\lambda_f^{(2)}$	$\lambda_f^{(3)}$	$b^{(1)}$	$b^{(2)}$	$b^{(3)}$	$T_*^{(1)}$	$T_*^{(2)}$	$T_*^{(3)}$
August,18	0.703	0.560	0.272	0.120	0.562	0.983	1.797	0.655	0.596	0.750	−0.0251	−0.0253	−0.0301
August,22	0.721	0.557	0.272	0.122	0.559	0.973	1.809	0.673	0.558	0.757	−0.0256	−0.0249	−0.0295
August,26	0.718	0.546	0.272	0.122	0.559	0.962	1.801	0.657	0.597	0.755	−0.0250	−0.0251	−0.0303
August,30	0.712	0.549	0.272	0.121	0.556	0.967	1.801	0.655	0.601	0.755	−0.0251	−0.0251	−0.0302
September,3	0.712	0.544	0.274	0.123	0.559	0.980	1.816	0.665	0.551	0.750	−0.0255	−0.0255	−0.0298
September,7	0.718	0.534	0.274	0.123	0.560	0.966	1.789	0.660	0.603	0.747	−0.0250	−0.0252	−0.0297

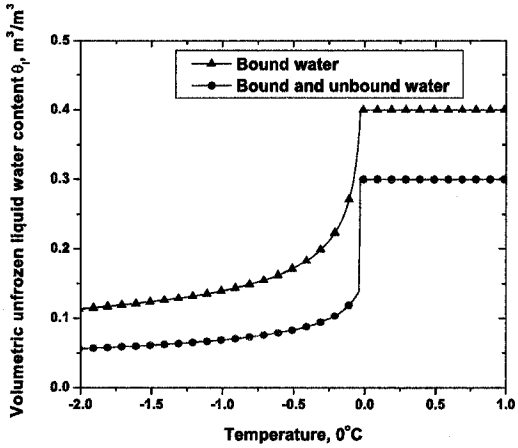

Figure 1.1: Typical volumetric content of the unfrozen liquid water in soils as a function of temperature. The curve marked by triangles is associated with soils in which all water is bound in soil pores, and hence the water content gradually decreases with decreasing temperature in $°C$. To compute this curve we used parametrization (1.3) in which T_*=$-0.03°C$ and b=0.3. The curve marked by circles is related to soils in which some percentage of water is not bound to the soil particle and changes its phase at the temperature T_*, while other part of liquid water is bound in soil pores and freezes gradually as the temperature decreases.

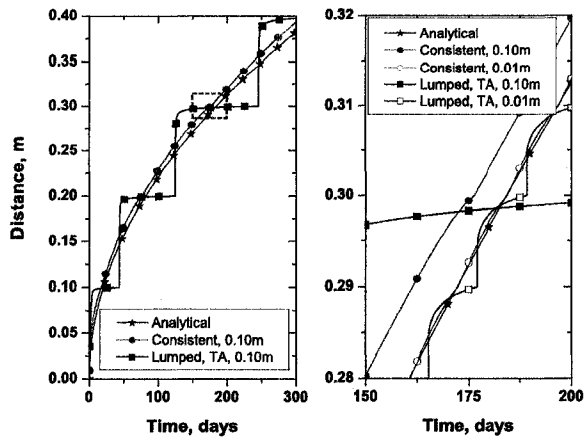

Figure 1.2: Comparison of analytical (stars) and numerical solutions. Initially, the soil has $-5°C$ temperature, and at the time t=0, the temperature at its upper boundary is changed to $1°C$. At the lower boundary located at 5 meter depth, zero flux boundary condition is specified. On the left plot, we show a location of the $0°C$ isotherm calculated for a uniform spatial discretizations with 0.1m grid element. The numerical solutions are computed by the proposed method (circles) and by the scheme using the lumped approach with temporal enthalpy averaging (squares). In the right plot, we show an enlarged area within the dotted rectangle and a location of the $0°C$ isotherm calculated for a uniform spatial discretizations with 0.1m (filled) and 0.01m (hollow) grid elements.

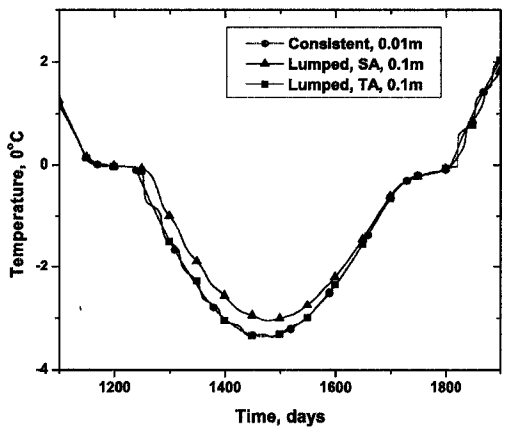

Figure 1.3: Computed soil temperature dynamics at 0.3 meter depth. Uniform 0.01 and 0.1 meter meshes are used to compute temperatures by the consistent (circles) and mass lumped approaches, respectively. The spatial (SA) and temporal (TA) enthalpy averaging in lumped schemes are marked my triangles and squares, respectively. Initially the temperature is zero, the upper boundary condition is given by Dirichlet type boundary condition with a slowly varying sinusoid having the amplitude of $3°C$ and the period of there years; zero heat flux is specified at 2 meter depth.

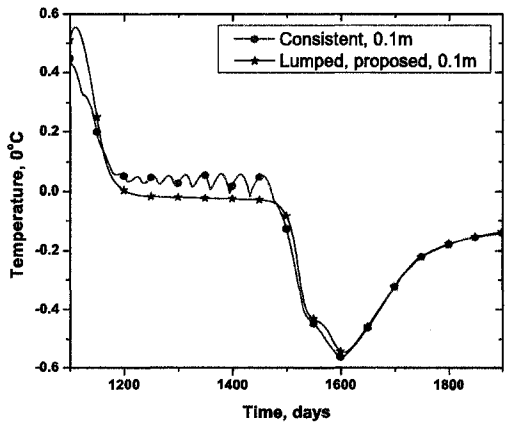

Figure 1.4: Temperature dynamics at 1 meter depth computed by the proposed consistent (circles) and the mass lumped schemes (stars). The mass lumped scheme is based on (1.23). In order to emphasize numerical oscillations occurring in the case of small time steps in the consistent approach, we use a uniform grid with 0.1m grid elements. The oscillations are due to violation of the discrete maximum principle in the consistent scheme during active phase change processes. The initial and boundary conditions are the same as stated in caption of Figure 1.3.

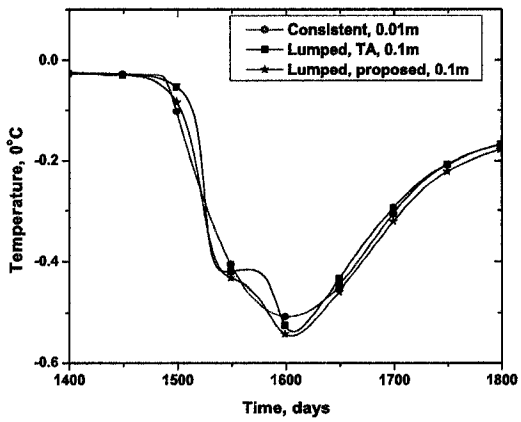

Figure 1.5: Temperature dynamics at 1 meter depth computed by the consistent approach (circles), the proposed mass lumped approach (stars) and the mass lumped approach with temporal enthalpy averaging (squares). The temperatures computed mass lumped approach are found on uniform grid with 0.1m grid elements, whereas in the consistent approach, the length of grid elements is 0.01m. The initial and boundary conditions are the same as stated in caption of Figure 1.3.

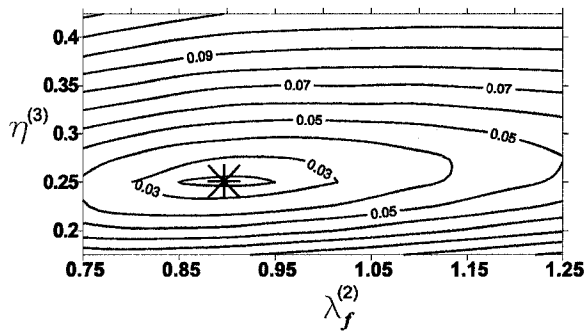

Figure 1.6: Isolines of the cost function $J(\mathcal{C})$ computed using the synthetic temperature data $T_{\mathcal{S}}$. The minimum of the cost function is marked by the start and is located at $\lambda_f^{(2)} = 0.9$ and $\eta^{(3)} = 0.25$, which is coincide with the values of $\lambda_f^{(2)}, \eta^{(3)}$ used to compute $T_{\mathcal{S}}$.

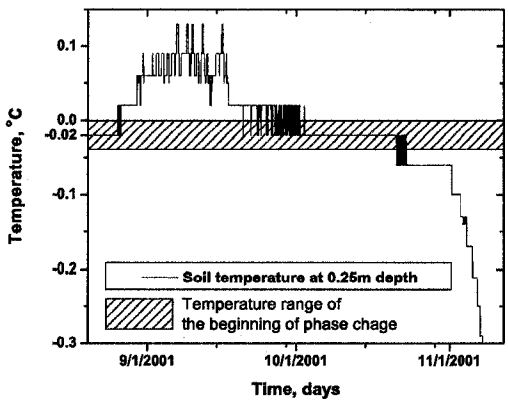

Figure 1.7: Temperature dynamics at 0.25 meter depth at Happy Valley site during the summer of 2001 year. The graph shows that uncertainty in temperature measurements is $\pm 0.02°C$. Within this uncertainty, the shadowed region represents a temperature range where the soil starts to freeze. Therefore, the temperature, T_*, of freezing point depression lies within the shadowed regions, i.e. in $[-0.04°C\ 0°C]$.

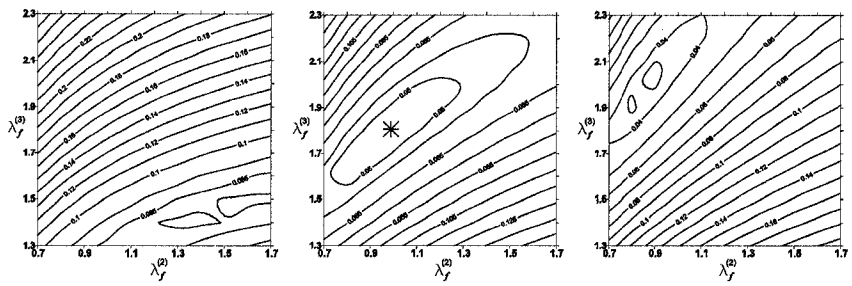

Figure 1.8: The isolines of the cost function J on the plane $(\lambda_f^{(2)}, \lambda_f^{(3)})$ for different values of the thermal conductivity $\lambda_f^{(1)}$ keeping constant at each plot. The values of $\lambda_f^{(1)}$ from the left to the right are 0.35, 0.55 are 0.70, respectively. The star in the central plot marks a selected combination of the thermal conductivities.

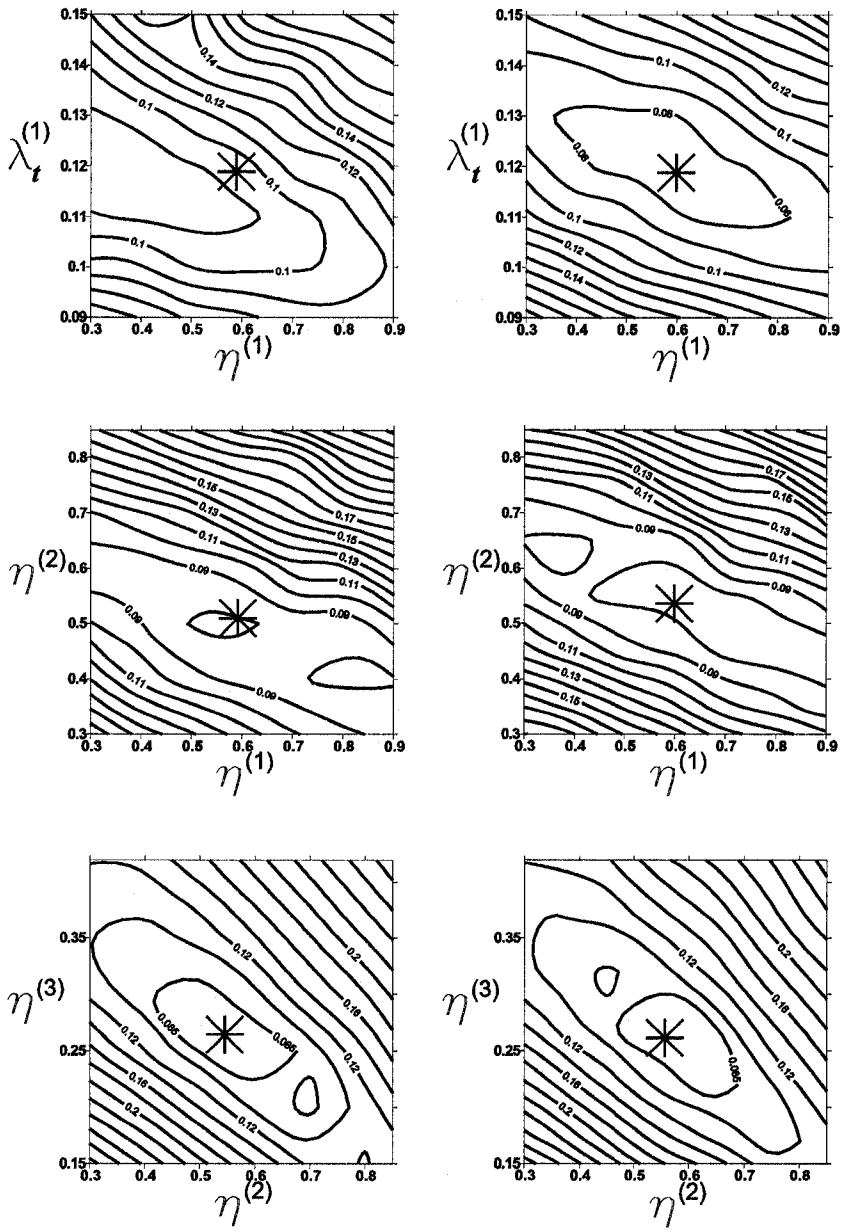

Figure 1.9: Selection of the thermal conductivity $\lambda_t^{(1)}$ and the soil porosity $\eta^{(1)}, \eta^{(2)}, \eta^{(3)}$ by minimizing the cost function associated with the "summer and fall" interval. The left and right column are associated with the first and the second iterations, respectively. The stars mark selected values of parameters after completing the iteration. Note that at the second iteration stars and minima are all coincide.

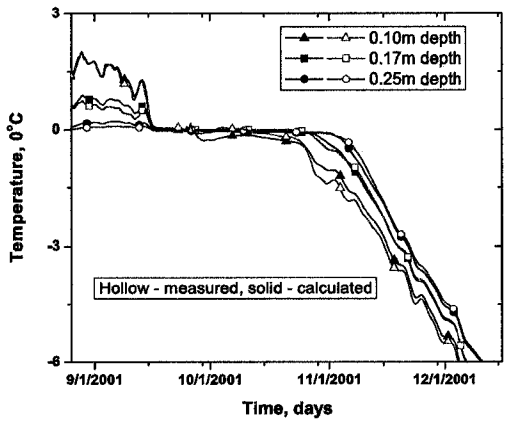

Figure 1.10: Measured (hollow) and calculated (solid) temperature at 0.10, 0.17 and 0.25 meter depth. The time interval is associated with the "summer and fall" period.

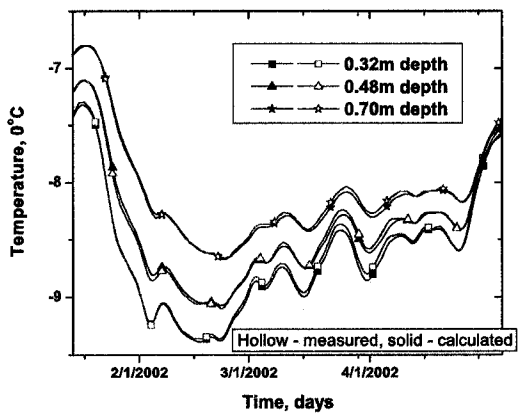

Figure 1.11: Measured (hollow) and calculated (solid) temperature at 0.32, 0.48, and 0.70 meter depth. The time interval is associated with the "winter" period.

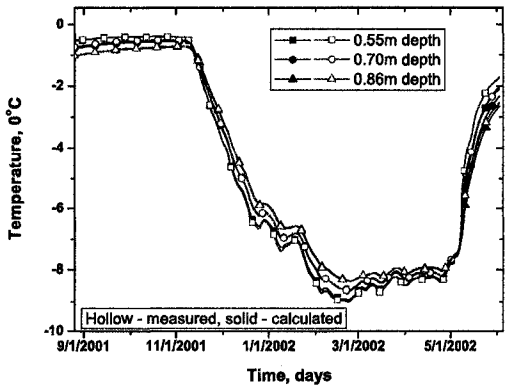

Figure 1.12: Measured (hollow) and calculated (solid) temperature at 0.55, 0.70 and 0.86 meter depth during the entire period of measurements used for calibration.

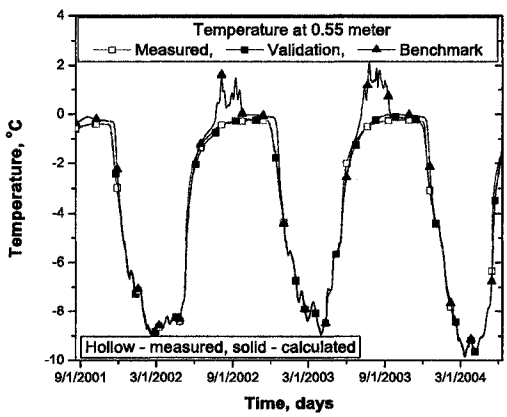

Figure 1.13: Measured (hollow) and calculated (solid) temperature at 0.55 meter depth during the entire period of measurements. The validation represents temperature dynamics computed for the found approximation to the soil thermal properties. The benchmark represents temperatures computed for the best guess soil properties, i.e. in the middle of ranges listed in Table 1.1.

Chapter 2
Assimilation of in-situ temperature data to estimate thermal properties of active layer and permafrost[2]

2.1 Abstract

A variational data assimilation algorithm is developed to reconstruct thermal properties, porosity, and parametrization of the unfrozen water content for fully saturated soils. The algorithm is tested with simulated synthetic temperatures. The simulations are performed to determine the robustness and sensitivity of the algorithm to estimate soil properties from in-situ high resolution-in-time temperature records in the active layer, and once-a-year measurements in a relatively deep borehole. The algorithm is applied to estimate soil properties at several sites along the Dalton Highway. The presented approach is quite general and can be applied to many problems requiring finding an optimal set of soil properties, and uncertainties in found soil properties.

2.2 Introduction

The volume and variety of soil temperature data has drastically increased in recent years. These data are typically composed of two types of observations: high-temporal-resolution temperature records at several depths beneath the soil surface, and instantaneous temperature profiles in a borehole, whose depth ranges from 10 to 100 meters, see Figure 2.1. Recent increase in collection of these data raises the question of how to analyze and utilize them efficiently. One of the important applications of the measured soil temperature is to reconstruct physical properties of soil such as liquid water content and the thermal properties of the ground material. Once the soil properties are known, they can be used to reconstruct soil temperature dynamics in the past and also to predict its future changes.

There are several methods for determining soil moisture content. Conventional Time Domain Reflectometry (*Topp et al.*, 1980) and drying methods are commonly used to estimate water content in homogeneous soils at shallow depths (*Boike and Roth*, 1997; *Yoshikawa et al.*, 2004). Moreover, accurate measurement of the total water content can be accomplished by thermalization of neutrons or by gamma ray attenuation, but transportation of

[2] D.J. Nicolsky, V.E. Romanovsky and G.G. Panteleev "Assimilation of in-situ temperature data to estimate thermal properties of active layer and permafrost", submitted to Cold Regions Science and Technology Journal

radioactive equipment into Arctic regions is impracticable (*Boike and Roth*, 1997). A review of state-of-the-art methods for measuring soil water content can be found in (*Gardner*, 1986; *Topp and Ferre*, 2002). However, the above-mentioned well-established methods rely on installation of special equipment in the field, or on laboratory experiments, and hence are not applicable for recovering soil water content from various soil temperature records.

Thermal properties can also be measured in the laboratory or in-situ experiments including the Needle Probe (*Herzen and Maxwell*, 1959), Divided Bar (*Birch*, 1950), borehole relaxation (*Wilhelm*, 1990), non-linear fitting (*Da-Xin*, 1986), thermal pulse (*Silliman and Neuzil*, 1990), and estimation from thermal gradients (*Somerton*, 1992) methods. Reviews of some of these methods can be found in (*Beck*, 1988). Similar to methods measuring water content, the methods for determining thermal properties are not applicable for recovering thermal properties from typical temperature measurements, i.e. temperature records at different depths. Methods that estimate thermal properties from temperature records include the Simple Fourier Methods (*Carson*, 1963), Perturbed Fourier Method (*Hurley and Wiltshire*, 1993), and Graphical Finite Difference Method (*McGaw et al.*, 1978; *Zhang and Osterkamp*, 1995; *Hinkel*, 1997). They estimate coefficients in the heat equation and yield accurate results for the thermal diffusivity (ratio of the thermal conductivity to the heat capacity) only when the phase change of water does not occur.

One alternative capable of estimating both thermal properties and water content of soil is variational assimilation of temperature observations into a model of soil freezing and thawing. A goal of the variational assimilation is to adjust/optimize a set $\mathcal{C}$ of model parameters in order to minimize a difference

$$J(\mathcal{C}) \approx \|T_o - T\|^2$$

between the observed T_o and modeled T temperatures. The set $\mathcal{C}$ includes parameters related to thermal conductivity, soil porosity and coefficients determining unfrozen water content for partially frozen soil. *Beck* (1964) and *Nagler* (1965) have applied the least square variational approach to estimate thermal properties in a heat conduction problem without phase change. In this chapter, we compute soil temperature, T, by employing the 1-D heat equation with phase change of water (*Carslaw and Jaeger*, 1959) and minimize the discrepancy $J(\mathcal{C})$ by optimizing $\mathcal{C}$.

Numerous books in mechanics (*Gladwell*, 1993), mathematics (*Anderson and Thomson*, 1992; *Murio*, 1993), oceanography (*Wunsch*, 1996), heat transfer (*Beck et al.*, 1985; *Alifanov*, 1995; *Alifanov et al.*, 1996) and geology (*DuChateau*, 1996) are devoted to iden-

tification of parameters through variational approaches. In addition, *Thacker and Long* (1988) and *Thacker* (1989) establish a link between mathematical formulation of the variational data assimilation and statistical formalism. We emphasize that unlike many other methods, the variational approach, when combined with statistical knowledge of errors in temperature measurements, permits the estimation of *a posteriori* errors in the optimized solution (*Thacker*, 1989).

Results from (*Beck et al.*, 1985; *Alifanov*, 1995; *Alifanov et al.*, 1996) include a detailed mathematical and theoretical analysis of variational temperature assimilation for the heat equation without explicit phase change terms. Some analysis of parameter estimation in heat conduction problems with phase change can be found in (*Pavlov et al.*, 1980; *Ouyang*, 1992; *Permyakov*, 2004). However, it is hard to find a discussion of variational assimilation being used to recover soil properties from in-situ temperature measurements in the active layer and permafrost.

We apply a variational technique to estimate thermal conductivity, porosity, and coefficients describing unfrozen water content at four locations along the Dalton Highway in Alaska. To evaluate the thermal properties, we use daily temperature measurements and a once-a-year temperature profile in 60 meter boreholes. Also, we conduct several numerical experiments and explore the robustness of recovering the thermal properties. The recovered properties that are associated with the minimum of $J(\mathcal{C})$ are sought by an iterative method. Since there could be several local minima, a thoughtful selection of an initial approximation of $\mathcal{C}$ as well as a certain regularization is necessary (*Nicolsky et al.*, 2007). We add to $J(\mathcal{C})$ a regularization that incorporates *a priori* estimate of values in the optimal control vector. Besides the regularization, we assume that the soil properties are constants within each soil horizon. This assumption decreases a hundred fold the number of variables in the control vector on which the cost function depends, and hence simplifies the problem.

Section-wise the remainder of this chapter is organized as follows. In Section 2.3, we describe the model of soil freezing and thawing, provide some details of its numerical realization, and formulate the inverse model. In Section 2.4, we show the results of twin experiments. In Section 2.5, we apply the approach to find thermal properties for several locations near the Dalton Highway in Alaska. Finally, in Section 2.6, we state conclusions.

2.3 Data assimilation techniques

In this section, we describe key components of the data assimilation technique. The main idea of the data assimilation technique is to optimize the set of model parameters, $\mathcal{C}$, in order to obtain the smallest possible value of $J(\mathcal{C})$, where the temperature T is computed by the model described in the next subsection.

2.3.1 Model of soil freezing and thawing

In many practical applications, heat conduction is the dominant mode of energy transfer in a ground material. Within certain assumptions (*Andersland and Anderson*, 1978; *Kudryavtsev*, 1978) the soil temperature $T, [°C]$ can be simulated by a 1-D heat equation with phase change (*Carslaw and Jaeger*, 1959):

$$C\frac{\partial}{\partial t}T(x,t) + L\frac{\partial}{\partial t}\theta(T,x) = \frac{\partial}{\partial x}\lambda\frac{\partial}{\partial x}T(x,t), \quad x \in [0,l], \quad t \in [0,\tau]. \tag{2.1}$$

The quantities $C{=}C(T,x)$ $[Jm^{-3}K^{-1}]$ and $\lambda{=}\lambda(T,x)$ $[Wm^{-1}K^{-1}]$ represents the volumetric heat capacity and thermal conductivity of soil, respectively; L $[Jm^{-3}]$ is the volumetric latent heat of fusion of water, and θ is the volumetric water content. The heat equation (2.1) is supplemented by initial temperature distribution $T(x,0){=}T_0(x)$, and boundary conditions at the ground surface $x{=}0$ and at the depth l. We use the Dirichlet boundary conditions, i.e. $T(0,t){=}T_u(t)$, $T(l,t){=}T_l(t)$. Here, $T_0(x)$ is the temperature at $x \in [0,l]$ at time $t{=}0$; T_u and T_l are observed temperatures at the ground surface and at the depth l, respectively.

One of the commonly used measures of liquid water in the freezing soil is the volumetric unfrozen water content (*Williams*, 1967; *Anderson and Morgenstern*, 1973; *Osterkamp and Romanovsky*, 1997; *Watanabe and Mizoguchi*, 2002). There are many approximations to θ_l in the fully saturated soil (*Lunardini*, 1987; *Galushkin*, 1997). The most common approximations are associated with power or exponential functions. Based on our positive experience in *Romanovsky and Osterkamp* (2000), we parameterize θ_l by a power function $\theta_l(T){=}a|T|^{-b}; a,b{>}0$ for $T{<}T_*{<}0°C$ (*Lovell*, 1957). The constant T_* is called the freezing point depression. In thawed soils ($T{>}T_*$), the amount of water in the saturated soil is equal to the soil porosity η. Therefore, we assume that

$$\theta(T,x) = \eta(x)\phi(T,x), \quad \phi(T,x) = \begin{cases} 1, & T \geq T_* \\ |T_*(x)|^{b(x)}|T|^{-b(x)}, & T < T_* \end{cases}, \tag{2.2}$$

where ϕ represents the liquid pore water fraction. For example, small values of b describe

the liquid water content in fine-grained soils, whereas large values of b are related to coarse-grained materials in which almost all water freezes at the temperature T_*.

We adopt the parametrization of thermal properties proposed by (*de Vries*, 1963; *Sass et al.*, 1971) with some modifications. We express thermal conductivity λ of the soil and its volumetric heat capacity C as

$$C = C_f(1-\phi) + C_t\phi, \qquad \lambda = \lambda_f^{1-\phi}\lambda_t^{\phi}, \tag{2.3}$$

where C_f and C_t are the effective volumetric heat capacities, respectively, and λ_f and λ_t are the effective thermal conductivities of soil for frozen and thawed states, respectively. For most soils, seasonal deformation of the soil skeleton is negligible, and hence temporal variations in the total soil porosity, η, for each horizon are insignificant. Therefore, the thawed and frozen thermal conductivities for the fully saturated soil are obtained from

$$\lambda_f{=}\lambda_s^{1-\eta}\lambda_i^{\eta}, \quad \lambda_t{=}\lambda_f\left[\frac{\lambda_l}{\lambda_i}\right]^{\eta}, \quad C_f{=}C_s(1{-}\eta){+}C_i\eta, \quad C_t{=}C_f{+}\eta(C_l{-}C_i). \tag{2.4}$$

where subscripts i, l, and s mark heat capacity C, thermal conductivity λ for ice at $0°C$, liquid water at $0°C$ and solid soil particles, respectively.

Evaporation from the ground surface and from within the upper organic layer can cause partial saturation of upper soil horizons (*Hinzman et al.*, 1991; *Kane et al.*, 2001). Therefore, formulae (2.4) need not hold in the presence of live vegetation and within organic soil layers, and possibly not within organically enriched mineral soil (*Romanovsky and Osterkamp*, 1997). Besides organic and organically enriched mineral soil layers, there are other horizons, all of which can have distinctive physical properties, texture and mineral composition. We assume that there are several horizons, namely: an organic layer, an organically enriched mineral soil layer, and a series of mineral soil layers. We assume that physical and thermal properties do not vary within each horizon, and hence $\lambda_f(x)$, $C_f(x)$, $\eta(x), T_*(x), b(x)$ can be assumed to be constants within each soil horizon:

$$\lambda_f(x){=}\lambda_f^{(i)}, \quad C_f(x){=}C_f^{(i)}, \quad \eta(x){=}\eta^{(i)}, \quad b(x){=}b^{(i)}, \quad T_*(x){=}T_*^{(i)}, \tag{2.5}$$

where the index i marks the index of the soil layer. Table 2.1 shows a typical soil horizon geometry and the commonly occurring ranges for the porosity η, thermal conductivity λ_f and the coefficients b, T_* parameterizing the unfrozen water content.

2.3.2 Inverse problem

A starting point in any inverse problem is selection of parameters to be recovered from available data. We note that if phase change effects are negligibly small then the heat capacity C and thermal conductivity λ cannot be resolved separately by analyzing the observed temperature time series; only the thermal diffusivity λ/C can be found (*Hinkel*, 1997). Therefore, in order to remove ambiguity in determining the soil properties, we set the heat capacity $C_f^{(i)}$ equal to a value that is typical for a soil type in the i-th layer. Consecutively, we define the *control vector* $\mathcal{C}$ as a set consisting of thermal conductivity $\lambda_f^{(i)}$, and parameters $\eta^{(i)}, T_*^{(i)}, b^{(i)}$ describing the unfrozen water content for each soil horizon, or

$$\mathcal{C} = \{\lambda_f^{(i)}, \eta^{(i)}, T_*^{(i)}, b^{(i)}\}_{i=1}^n. \tag{2.6}$$

For each physically realistic control vector $\mathcal{C}$, it is possible to compute temperature dynamics and compare it to the measured data. The available measured data are organized as two vectors: $\boldsymbol{d}_a$ and $\boldsymbol{d}_b$, associated with high-resolution-in-time temperature records, and once-a-year measurements in the borehole, respectively. In this chapter, we mark quantities related to the active layer and bore hole measurements by subscripts a and b, respectively. The data are related to the control vector $\mathcal{C}$ by

$$\boldsymbol{m}_a(\mathcal{C}) - \boldsymbol{d}_a = \boldsymbol{e}_a, \quad \boldsymbol{m}_b(\mathcal{C}) - \boldsymbol{d}_b = \boldsymbol{e}_b,$$

where $\boldsymbol{m}$ is the modeled counterparts of the data, and $\boldsymbol{e}$ is the misfit vector. In theory, if there are no sampling errors or model inadequacies, the misfit vector $\boldsymbol{e}$ can be reduced to zero. If there are errors in the data or in the model, the aim is to minimize $\boldsymbol{e}$ by varying the control vector $\mathcal{C}$.

Assuming that the errors $\boldsymbol{e}$ have a Gaussian probability distribution, we define the cost function J according to (*Beck and Arnold*, 1977; *Tikhonov et al.*, 1996) as

$$J = J_a + J_b + J_r, \tag{2.7}$$

where J_a, J_b are related to model/data misfit, and J_r is the regularization term:

$$J_\alpha(\mathcal{C}) = \frac{1}{2}\big(\boldsymbol{m}_\alpha(\mathcal{C}) - \boldsymbol{d}_\alpha\big)^t \boldsymbol{R}_\alpha^{-1}\big(\boldsymbol{m}_\alpha(\mathcal{C}) - \boldsymbol{d}_\alpha\big), \quad \alpha = a, b \tag{2.8}$$

$$J_r(\mathcal{C}) = \frac{1}{2}\big(\mathcal{C} - \mathcal{C}_0\big)^t \boldsymbol{R}_m^{-1}\big(\mathcal{C} - \mathcal{C}_0\big). \tag{2.9}$$

Here, the superscript t stands for the transposition operator, $\boldsymbol{R}_\alpha$ and $\boldsymbol{R}_m$ are covariance matrices for the data $\boldsymbol{d}_\alpha$ and control vector, respectively. Finally, $\mathcal{C}_0$ is an initial approxi-

mation vector containing *a priori* estimates of soil properties based on soil texture, mineral composition and porosity (*Nicolsky et al.*, 2007).

Physically, terms J_a and J_b describe a mean square deviation of the computed soil temperatures from the measured ones, while the term J_r incorporates information about the soil properties that could be derived from the field/laboratory experiments, or from existing soil property databases and published data (*Kersten*, 1949). Typically, $\boldsymbol{R}_m$ is a diagonal matrix with the expected variances $\{\sigma_m^2\}$ of each control vector variable down the main diagonal. For example, if *a priori* estimates in $\mathcal{C}_0$ are known with large uncertainties, then the expected variances $\{\sigma_m^2\}$ are large, and hence contribution of the term J_r to the cost function J is small. The opposite is also true. Namely, if the initial approximation $\mathcal{C}_0$ is known with a good degree of accuracy, then contribution of J_r is large and a minimum of J is close to the *a priori* estimates in $\mathcal{C}_0$.

Statistical interpretation of the least square method considers the cost function as an argument of the Gaussian probability distribution (*Thacker*, 1989; *Wunsch*, 1996). Under this statistical interpretation, the optimal control vector $\hat{\mathcal{C}}$ defined by

$$J(\hat{\mathcal{C}}) = \min_{\mathcal{C}} J(\mathcal{C})$$

is the most probable combination of the soil properties for the given temperature realization and prior error statistics. To compute the optimal control vector, we calculate the gradient

$$\nabla J = \left\{ \frac{\partial J}{\partial \lambda_f^{(i)}}, \frac{\partial J}{\partial \eta^{(i)}}, \frac{\partial J}{\partial T_*^{(i)}}, \frac{\partial J}{\partial b^{(i)}} \right\}_{i=1}^{n}$$

of the cost function and minimize cost function J by the Quasi-Newton minimization algorithm (*Fletcher*, 2000). To calculate the gradient ∇J, we construct and solve the adjoint model (*Jarny et al.*, 1991; *Marchuk*, 1995; *Wunsch*, 1996). The adjoint code is built analytically by transposition of the operator of the tangent linear model, which was obtained by direct differentiation of the forward model code, briefly described in Appendix 2.8.

In order to estimate the thermal properties uniquely, the boundary conditions must satisfy some requirements, i.e. be monotonous functions of time (*Muzylev*, 1985). In nature, the rapidly changing weather conditions enforce the surface temperature which does not fulfil this necessary requirement. Consequently, the cost function can have several minima due to non-linearities in the heat equation (2.1). Therefore, the iterative minimization algorithm can converge to an improper minimum if the iterations are started from an arbitrary selected initial guess $\mathcal{C}_g$. Nevertheless, with the initial guess $\mathcal{C}_g$ within the basin

of attraction of the global minimum, the iterative optimization method should converge to the proper minimum even if the model is nonlinear (*Thacker*, 1989). Usually, the initial guess $\mathcal{C}_g$ is selected to be in the neighborhood of the initial approximation $\mathcal{C}_0$. Thus, the right choice of the initial approximation $\mathcal{C}_0$ is important for efficient convergence. In (*Nicolsky et al.*, 2007), we provide a detailed step-by-step algorithm to compute the initial approximation $\mathcal{C}_0$.

To obtain physically meaningful results, the covariances matrix $\boldsymbol{R}_\alpha$ has to be defined appropriately as follows. By definition, if all elements in temperature data $\boldsymbol{d}_a$ vector are statistically independent, then $\boldsymbol{R}_\alpha$ is a diagonal matrix with expected variances σ_α^2 of $\boldsymbol{e}_\alpha$ along the main diagonal. Since temperature disturbances at the ground surface decay exponentially with depth, the soil temperature does not change significantly over hourly time intervals at depths over 0.10 meters (*Carslaw and Jaeger*, 1959; *Kudryavtsev*, 1978; *Yershov*, 1998). Thus, hourly collected temperature observations are not statistically independent. We note that a typical time scale over which air temperature changes randomly is approximately ten days (*Blackmon et al.*, 1984). For the Alaska North Slope Region, these air temperature fluctuations can penetrate up to the depth of 0.3-0.5 meters and significantly (and randomly) change soil temperature in the upper meter on a monthly time scale. Hence, the covariance matrix $\boldsymbol{R}_a$ is approximately a sparse matrix with some diagonal structures, the sizes of which are equal to the number of temperature measurements collected in one month. For the sake of simplicity, we approximate $\boldsymbol{R}_a$ by a diagonal matrix with σ_a^2 down on a main diagonal multiplied by weights. The weight of each particular measurement is such that the sum of weights corresponding to measurements within each month is equal to one. In our case, we assume that σ_a are equal uncertainties in temperature measurements due to the limited precision of sensors. Also, since our temperature measurements are equidistantly distributed through time, we set weights equal to $1/n$, where n is a number of measurements within each month.

Considering a variable c_i in the control vector $\mathcal{C}=\{c_i\}_{i=1}^m$ as stochastic and non-correlated, it is possible to define errors of the optimally estimated parameters $\hat{\mathcal{C}}=\{\hat{c}_i\}_{i=1}^m$. According to *Thacker* (1989), the error covariance of the corresponding variables of the control vector can be calculated as diagonal elements of the inverse Hessian matrix $\boldsymbol{H}^{-1}$, where $\boldsymbol{H}=\{h_{ij}\}_{i,j=1}^m$, and $h_{ij}=\partial^2 J/\partial c_i \partial c_j$. The most simple method to compute $\boldsymbol{H}$ is to approximate it via finite-differences (*Schröter*, 1989). Following this approach, we individually perturb the components c_i of the control vector in the vicinity of the optimal values

$\hat{c}_i$. After that, the finite-difference approximation of the Hessian can be defined as

$$h_{ij} \approx \frac{1}{2\delta}\Big(\nabla_j J(\hat{\mathcal{C}} + \delta \mathcal{I}_i) - \nabla_j J(\hat{\mathcal{C}} - \delta \mathcal{I}_i)\Big),$$

where δ is a positive real-valued number, $\mathcal{I}_i = (0, 0, \ldots, 1, \ldots, 0)$ is an m-dimensional zero-vector whose i-th element is one, and the quantity $\nabla_j J$ represents the j-th component of cost function's gradient ∇J. The inverse of the Hessian $\boldsymbol{H}$ can be easily computed since the number m of variables in the control vector $\mathcal{C}$ is typically less than a hundred.

2.4 Twin experiments

The effectiveness of temperature data assimilation in determining soil thermal properties has to be assessed. A convenient methodology, termed the identical twin experiments, has been proposed in meteorology by *Bengtsson et al.* (1981); *Ghil and Malanotte-Rizzoli* (1991); and *Panteleev et al.* (2004). We adopt this methodology and apply it to compare true soil properties to their estimated values.

2.4.1 Identical twin experiment

In the identical twin experiment, we select a control vector $\tilde{\mathcal{C}}$, called the true control vector, and compute the soil temperature dynamics corresponding to it. From the computed temperatures, we assemble the true data $\tilde{\boldsymbol{d}}_\alpha$ to imitate observations $\boldsymbol{d}_\alpha$. Another set of temperature dynamics are then computed using a control vector $\mathcal{C}$ that is a perturbed copy of $\tilde{\mathcal{C}}$. We note that temperatures computed for the control $\mathcal{C}$ are called the false temperatures, and there is discrepancy between $\boldsymbol{m}_\alpha(\mathcal{C})$ and the true data $\tilde{\boldsymbol{d}}_\alpha$, i.e. $\tilde{\boldsymbol{e}}_\alpha = \boldsymbol{m}_\alpha(\mathcal{C}) - \tilde{\boldsymbol{d}}_\alpha \neq 0$. Therefore, the cost function $J(\mathcal{C})$ (defined by (2.7-2.9) in which $\boldsymbol{d}_\alpha$ is substituted by $\tilde{\boldsymbol{d}}_\alpha$) is not equal to zero. The Quasi-Newton optimization scheme is then used to minimize the cost function $J(C)$ and to find the optimal control vector $\hat{\mathcal{C}}$.

In the identical twin experiment, we observed ground surface temperature T_u near Deadhorse, Alaska to compute the soil temperature dynamics. The modeled ground material has four different layers corresponding to lithology at the Deadhorse site ($148°27'W$, $70°10'N$). The layers are organically enriched mineral soil between 0–0.2 meters, silt between 0.2–0.9 meters, sandy silt between 0.9–2.7 meters, and gravel between 2.7–50.0 meters. The lower boundary condition T_l is set by measured temperatures at 50.0 meter depth. For each soil layer, we select values of parameters in the true control vector $\tilde{\mathcal{C}}$ to be equal to the median values of those listed in Table 2.1. Once the true control is chosen, we compute soil temperature in the upper 50.0 meters beneath the soil surface during the period between August 1,

1997 and June 1, 2002. Consecutively, we define the true data $\tilde{\boldsymbol{d}}_{\boldsymbol{a}}$ as a set of the computed temperature dynamics at depths of 0.15, 0.3, 0.38, 0.46, 0.53, 0.69, 0.84 and 0.99 meters which are used to measure temperature at the Deadhorse site. Additionally, in the middle of June each year we select from the computed temperatures once-a-year soil temperature profiles (between 5.0 and 50.0 meters below the ground surface) to define the true data $\tilde{\boldsymbol{d}}_{\boldsymbol{b}}$. To imitate noisy measurements, we add normally distributed white noise (with $0.1°C$ standard deviation in upper meter, and with $0.03°C$ standard deviation in deep boreholes) to the true data $\tilde{\boldsymbol{d}}_{\boldsymbol{a}}$ and $\tilde{\boldsymbol{d}}_{\boldsymbol{b}}$. Finally, we add noise to the boundary conditions T_u and T_l used to force the model. These noisy temperature data $\tilde{\boldsymbol{d}}_{\boldsymbol{a}}$ and $\tilde{\boldsymbol{d}}_{\boldsymbol{b}}$ and boundary conditions were then used to recover the control vector $\tilde{\mathcal{C}}$ by minimizing the cost function J. We note that for the sake of simplicity, the cost function does not have a regularization term J_r in this experiment.

We considered an assembly of twenty identical twin experiments. Each of one differs by a realization of the added noise, and the initial guess $\mathcal{C}_g$ from which the minimization of J is started. Each twin experiment produces a set $\hat{\mathcal{C}} = \{\hat{\lambda}_f^{(i)}, \hat{\eta}^{(i)}, \hat{T}_*^{(i)}, \hat{b}^{(i)}\}_{i=1}^4$ of recovered soil properties. Results $\hat{\mathcal{C}}$ from all identical twin experiments are shown in Figure 2.2. In these plots, recovered soil properties are marked by circles, and their true values are marked by crosses. We observe that the soil porosity η is found correctly in the upper three layers, where active phase change occurs. Additionally, the results show that it is impossible to estimate η for the deep 2.7−50.0 meter layer since the ground material found there is constantly frozen. The thermal conductivity is estimated correctly for all layers. The quantities b and T_* used to parameterize the unfrozen water content ϕ are found correctly only for the second and third layers. One of the explanations for a significant spread of b and T_* in the first layer is that freezing/thawing occurs in the upper layer quite rapidly, and the number of available temperature records used for assimilation is not large enough to resolve near-$0°C$ temperature dynamics in the upper layer. In the deep 2.7−50.0 meter layer, the coefficients b and T_* are not found since there is no active phase change at such depths.

We emphasize that in this identical twin experiment, we started all searches in the vicinity of the true control vector, i.e. within ±30% of the true values measured entry-wise. Therefore, this experiment shows that the iterative minimization algorithm converges to the proper minimum if the initial guess is close to its true value even though the data were noisy. In real-life experiments where the true control vector is unknown, knowledge of a

good initial guess (commonly equal to the initial approximation) is important.

2.4.2 Fraternal twin experiment

In the identical twin experiment, we generated the true data and then assimilated it by a model that has exactly the same geometry of soil layers. In nature, the boundaries between soil layers are not strictly defined, and hence locations of these boundaries have some uncertainties. Moreover, we assume that the soil properties are constant within each layer, whereas in nature they often "smoothly" vary with depth. In this section, we analyze sensitivity of recovery of soil properties with respect to the geometry of soil layers by considering the fraternal twin experiment (*Arnold and Dey*, 1986).

Briefly, the methodology of the fraternal twin experiment is as follows. The true soil temperature data $\tilde{\boldsymbol{d}}_{\boldsymbol{a}}$ and $\tilde{\boldsymbol{d}}_{\boldsymbol{b}}$ are computed by a model in which soil properties λ_f, η, b, and T_* smoothly vary with depth. These true data are then assimilated into a model in which soil properties are constant within each soil layer.

Before we further consider the fraternal twin experiments, we note that soil temperature records collected in an organic layer can not be always properly modeled by heat equation (2.1) due to non-heat conductive heat transport (*Hinzman et al.*, 1991; *Kane et al.*, 2001; *Romanovsky and Osterkamp*, 2001). Therefore, in the fraternal twin experiment, we specify the "surface" boundary condition at some depth, below which non-conductive heat transfer is negligibly small. From the field observation, we know that for Alaskan Coastal plain this depth is $0.2 - 0.3$ meters and located at the boundary of the organic/mineral and mineral layer (*Romanovsky and Osterkamp*, 1997, 2001).

In the fraternal twin experiments, two experiments, **A** and **B**, are considered in which we simulate temperature dynamics in ground material located within $0.30 - 50.0$ meters below the ground surface. In experiment **A**, we assume that the ground material is sand-gravel and has higher thermal conductivity comparing to the sand-silt profile specified in **B**, see the right plots in Figure 2.3. Additionally, we assume that the modeled ground materials in both experiments have different soil porosity profiles, shown in the left plots in Figure 2.3. In these plots, profiles plotted by smooth lines with stars are used to compute the true soil temperature dynamics. Additionally, we assume that dependence of the unfrozen water content on temperature is the same at any depth, i.e. $\theta = \theta(T)$. But, the unfrozen water content curves $\theta = \theta(T)$ differ between simulations **A** and **B**.

In each experiment, after computing the soil temperature dynamics, we add to the

temperatures normally distributed white noise, having characteristics as in the identical twin experiment, and then assemble the true data $\tilde{\boldsymbol{d}}_{\boldsymbol{a}}$ and $\tilde{\boldsymbol{d}}_{\boldsymbol{b}}$. We note that the true data $\tilde{\boldsymbol{d}}_{\boldsymbol{a}}$ is assembled by temperature records at 0.38, 0.46, 0.53, 0.69, 0.84 and 0.99 meter depths. The data $\tilde{\boldsymbol{d}}_{\boldsymbol{b}}$ is defined as in the identical twin experiment, i.e. once-a-year temperature profiles in the middle of June of each year between 5.0 and 50.0 meters below the ground surface. The observed temperature dynamics at the Deadhorse site at 0.30 meter depth is used to set the upper boundary condition T_u. The lower boundary condition, T_l, is set at 50.0 meter depth using the measured temperatures.

Once the true data $\tilde{\boldsymbol{d}}_{\boldsymbol{a}}$ and $\tilde{\boldsymbol{d}}_{\boldsymbol{b}}$ are computed, we assume that the modeled ground material has several soil layers (increasing with depth thicknesses) between 0.30 and 50.0 meters such that soil properties are constants within each layer. The goal of this experiment is to recover soil properties of each layer based on $\tilde{\boldsymbol{d}}_{\boldsymbol{a}}$ and $\tilde{\boldsymbol{d}}_{\boldsymbol{b}}$. However, analyzing results of the identical twin experiment, we recognize that it is impossible to recover soil porosity and the parametrization of the unfrozen water content for deep soil layers which are always frozen. Hence, we try to recover two numbers: the first one is associated with the soil porosity of the first layer, and the second one approximates the soil porosity of all other layers. We recover two constants approximating b and T_* for all layers (dependence of the unfrozen water content on temperature is assumed to be independent on depth). Also, we find a constant for each soil layer such that these constants approximate smoothly varying thermal conductivity.

Based on knowledge regarding soil texture and mineral composition of the modeled soil, we compose the initial approximation $\mathcal{C}_0$ for experiments **A** and **B**. Value of parameters in the initial approximation $\mathcal{C}_0$ for each layer is selected based on its texture listed in Table 2.1.

As in the identical twin experiment, we investigate dependence of recovered soil properties on the initial guess $\mathcal{C}_g$ that is chosen within $\pm 30\%$ of the initial approximation $\mathcal{C}_0$. We completed twenty fraternal twin experiments and plotted the recovered thermal conductivities and soil porosities in Figure 2.3 by step-wise functions, where each "step" is associated with a soil horizon. These experiments reveal that the recovered soil properties are averaged values of the soil properties used to calculate the true data. Instead of plotting recovered values of b and T_*, we plot dependence of the unfrozen water content on temperature. The recovered dependence closely matches the one used to compute the true temperature data, see Figure 2.4.

2.5 Reconstruction of thermal properties for sites along the Dalton Highway

To illustrate how the developed technique could be used for specific applications, we apply it to recover soil properties at four sites on the coastal plain of the Alaska Arctic adjacent to the Beaufort Sea. The sites are located along the Dalton Highway and include West Dock ($148°33'W$, $70°22'N$), Deadhorse ($148°27'W$, $70°10'N$), Franklin Bluffs ($148°43'W$, $69°39'N$) and Imnaviat Creek sites($149°20'W$, $68°37'N$). The soil temperature data were obtained from 1996 to 2007 with sensors measuring hourly temperature at several depths within an active layer and upper permafrost with $0.05°C$ uncertainty. The temperature data also include annually measured temperatures (with $0.02°C$ uncertainty) in 60.0 meter boreholes located at the same sites. Detailed descriptions of site conditions, methods of measurements and data processing have been published in (*Romanovsky and Osterkamp*, 1995) for all sites except for the Imnaviat Creek site.

Temperature measurements inside a deep borehole are conducted by lowering a temperature probe into a small diameter pipe filled with a convection preventive fluid. Due to minor ground surface disturbance and presence of a metal pipe, temperature measurements in the upper 5.0 meters below the ground surface can be biased. Uncertainty in temperature measurements between 5.0 and 10.0 meters is $0.03°C$ and lower than 10.0 meters the uncertainty is $0.02°C$ or less.

2.5.1 Imnaviat Creek site

The temperature sensors were installed on August 26, 2006 at depths 3.0, 5.0, 7.0, 10.0, 15.0, 20.0, 30.0, 40.0, 50.0, and 60.0 meters, and hourly temperature measurements were taken through June 25, 2007. Since, only one year of temperature dynamics is available for this site to assimilate, and since temperature change below 30.0 meters is less than the uncertainty of measurements, we can assimilate data only between 5.0 and 30.0 meters. Therefore, we set upper and lower boundary conditions: $T_u(t)$ and $T_l(t)$ at 3.0 and 40.0 meters, respectively. During the drilling of this borehole, it was observed that the ground material is primarily ice with a small number of boulders, and hence we assume that it can be modeled by a single layer.

At the depth of 3.0 meters and below, the ground material is constantly frozen. Therefore, based on results from the sensitivity analysis in Section 2.4, we can not estimate soil porosity and parametrization of unfrozen water uniquely. We assume that the soil porosity η=0.90, and the unfrozen water content decreases sharply at T_*=$-0.01°C$, i.e. b=5. We

applied the data assimilation technique and obtained

$$\lambda_f = 2.64 \pm 0.06.$$

The difference between the modeled and observed temperature time series is less than $0.06°C$. Note that thermal conductivity λ_f for pure ice at $-5°C$ is 2.2 (*Lide*, 1999), and the inclusion of small boulders can increase this value.

2.5.2 West Dock, Deadhorse and Franklin Bluffs sites

Temperature sensors were placed at 0.30, 0.38, 0.46, 0.53, 0.69, 0.84, and 0.99 meter depths at the Deadhorse and Franklin Bluffs sites, and at 0.30, 0.37, 0.52, 0.68 and 0.83 meter depths at the West Dock site. At these depths, in this analysis, hourly temperature measurements were used during the following time intervals: at West Dock between August 7, 1997 and August 18, 2002, at Deadhorse between July 8, 1997 and June 2, 2002, and at Franklin Bluffs between July 2, 1998 and September 2, 2004. Drilling records were used to determine lithology, see Table 2.2. Results of previous investigations (*Lachenbruch et al.*, 1982; *Lachenbruch and Marshall*, 1986; *Zhang*, 1993; *Osterkamp and Romanovsky*, 1996) were used to determine the initial approximation $\mathcal{C}_0$. After applying the variational approach, we list the estimated soil properties in the active layer and upper permafrost in Table 2.2 and compare them to the corresponding values in $\mathcal{C}_0$. We note that the first layer, at the West Dock site, we obtained a good correlation with previous results reported by *Romanovsky and Osterkamp* (1997), whereas for the first layer at the Deadhorse and Franklin Bluffs sites our estimated values of $\lambda_f^{(1)}$ are higher than the previously reported by 10%, and 20%, respectively. Also we note that for the West Dock and Deadhorse sites we obtain relatively high thermal conductivities λ_f for the deeper soil layers, see Table 2.1. These values of λ_f are 10% higher than previous estimates in (*Osterkamp and Romanovsky*, 1996). We note that for the deep layers between 17.0 and 50.0 meters at the Franklin Bluffs site, the ground material is a mixture of shale and silt. Usually, the thermal conductivity of shale is lower than the one corresponding for gravel which is widely distrubited at the Deadhorse and West Dock sites. Hence we obtain lower values of the thermal conductivity at the Franklin Bluffs site. Our obtained optimal values of the thermal conductivities are 25% lower than the ones given in (*Osterkamp and Romanovsky*, 1996), but are still in the range of commonly occurring values (*Andersland and Anderson*, 1978). The soil porosity estimated by our approach is within a range of its typical variability (*Romanovsky and Osterkamp*, 1997).

Using the estimated properties, soil temperature dynamics are calculated for the entire period of measurements involved in this analysis. Results are shown in the left plot of Figure 2.5. In this plot, we compare the calculated and measured permafrost temperatures at depths of 0.52 and 0.68 meters. In the right plot of Figure 2.5, we display a histogram of differences between the measured and computed optimal temperature dynamics at 0.52 and 0.68 meters. The mean value of the differences is about $0.01°C$, and their standard deviations are less than $0.08°C$. In the left plot of Figure 2.6, we show measured and calculated optimal permafrost temperature profiles at the West Dock site on July 3, 1998, June 16, 1999, June 14, 2000, and on June 18, 2001. The largest deviation of the computed temperature from the measured one is a few tenths of a degree in the upper 10.0 meters below the soil surface, due to coarsely discretized soil lithology. In the right plot of Figure 2.6, we show computed and measured permafrost temperature profiles at the Franklin Bluffs. At this site the thermal conductivity of the deep soil layer is smaller, so the permafrost warming is at much slower rate than at Deadhorse and West Dock, see Figure 2.6.

Based on the above examples, we showed the applied variational approach robustly estimates soil properties for various soil types. However, some limitations exist and they are discussed in the next section.

2.6 Discussion and conclusions

We applied a data assimilation technique to determine soil porosity, thermal conductivity, and parametrization of the unfrozen water content of the active layer and permafrost. Data assimilation permits recovery of these soil properties in layers, for which no direct and continuous temperature measurements are available. However, in each case sensitivity of the recovered parameters on the available data has to be analyzed. Based on the results of the performed sensitivity analysis for a typical configuration of soil layer and in-situ observations (the high-temporal-resolution temperature records at several depths below the soil surface, and occasional measurements in a adjacent deep borehole) we conclude that it is possible to estimate thermal conductivity for all soil layers. However, soil porosity and parametrization of the unfrozen water content can be identified only for intermediate layers where active phase change occurs. For other combinations of soil layers and ground surface conditions, additional sensitivity analysis has to be performed in order to establish a set of recoverable parameters.

To regularize recovery of the soil properties, the cost function used in the variation

approach has to incorporate initial approximation to the soil properties based on available data (*Kersten*, 1949). Another approach to calculate the initial approximation is proposed in (*Nicolsky et al.*, 2007), whereby a series of simpler subproblems is solved to find $\mathcal{C}_0$ and to find a range of variables in $\mathcal{C}$.

One limitation of the variational approach that was used in this work is that it requires certain values of heat capacities in order to find a unique value of the thermal conductivity and soil porosity. Also, the applied approach computes the volumetric content of water which changes its phase during freezing or thawing. Water content of liquid water that is tightly bound to soil particles and is not changing its phase can not be estimated within the proposed model (2.1). Additionally, we used 1-D assumption regarding the heat diffusion in the active layer, which sometimes is not applicable due to hummocky terrain in the Arctic tundra. Another assumption used in the model is that the frost heave and thaw settlement is negligibly small and there is no ice lens formation in the ground during freezing. Therefore, the proposed method could only be applied where these assumption are satisfied.

Although there are several limitations to the presented approach, we applied it to find soil properties for the West Dock, Deadhorse, Franklin Bluffs and Imnaviat Creek sites along the Dalton Highway in Alaska. The difference between the assimilated and measured temperature dynamics is typically less than $0.3°C$ and it is mostly due to oversimplified lithology and physics of soil freezing and thawing. The presented algorithm provided the most probable estimates of the soil properties. The ability to estimate errors in the calculated soil properties is an attractive feature of our algorithm and may be taken advantage of in practice.

2.7 Acknowledgement

We would like to thank Jacob Stroh, Sergei Marchenko, Martin Truffer, Edward Bueler and Paul Layer for all their advice, critique and reassurances along the way. This research was funded by ARCSS Program and by the Polar Earth Science Program, Office of Polar Programs, National Science Foundation (OPP-0120736, ARC-0632400, ARC-0520578, ARC-0612533, IARC-NSF CA: Project 3.1 Permafrost Research), by NASA Water and Energy Cycle grant, and by the State of Alaska.

2.8 Appendix A. Numerical model of soil freezing

Following finite element framework (*Zienkiewicz and Taylor*, 1989), we approximate

$$T(x,\tau) \approx \sum_{i=1}^{n} \psi_i(x)\boldsymbol{t}_i(\tau),$$

where $\boldsymbol{t}_i(\tau)$ is a "value" of temperature at the i-th finite element grid, and ψ_i is the basis function. After some standard manipulations, we derive a system of differential equations

$$\boldsymbol{M}(\boldsymbol{t})\frac{d}{d\tau}\boldsymbol{t}(\tau) = -\boldsymbol{K}(\boldsymbol{t})\boldsymbol{t}(\tau), \qquad \boldsymbol{t} = \boldsymbol{t}(\tau) \tag{2.10}$$

where $\boldsymbol{t}(\tau) = \{\boldsymbol{t}_i(\tau)\}_{i=1}^{n}$ is the vector consisting of temperature values, $\boldsymbol{M}(\boldsymbol{t}) = \{m_{ij}(\boldsymbol{t})\}_{ij=1}^{n}$ and $\boldsymbol{K}(\boldsymbol{t}) = \{k_{ij}(\boldsymbol{t})\}_{ij=1}^{n}$ are the $n \times n$ capacitance and stiffness matrices, respectively. A further refinement, which is often used in finite element modeling of phase change problems, is to exploit a "lumped" formulation, i.e. the capacitance matrix $\boldsymbol{M}$ is diagonal:

$$m_{ij}(\boldsymbol{t}) = \delta_{ij}c_i(\boldsymbol{t})\int_0^l \psi_i dx, \qquad c_i(\boldsymbol{t}) \approx C(\boldsymbol{t}_i, x_i) + L\frac{d\theta}{dT}(\boldsymbol{t}_i), \tag{2.11}$$

where δ_{ij} is one if $i = j$, or zero otherwise. *Dalhuijsen and Segal* (1986) provides justification for the lumped formulation on noting that it is computationally advantageous and avoids oscillations in numerical solutions when used in conjunction with the backward Euler scheme:

$$\begin{aligned} \left[\boldsymbol{M}^{(k)} + d\tau_k \boldsymbol{K}^{(k)}\right]\boldsymbol{t}^{(k)} &= \boldsymbol{M}^{(k)}\boldsymbol{t}^{(k-1)}, & k > 1 \\ \boldsymbol{t}^{(k)} &= \boldsymbol{t}_0, & k = 0. \end{aligned} \tag{2.12}$$

The main difficulty in numerical modeling of soil freezing/thawing is in consistent calculation of the derivative $d\theta/dT$ in (2.11), where $\theta(T)$ is not a continuously differentiable function defined by (2.2). In many reviews, it is proposed to employ the *enthalpy temporal averaging* to calculate $c_i(\boldsymbol{t})$. We suggest an approach that incorporates ideas of temporal averaging just to evaluate the rapidly changing $\theta(T)$ by defining c_i as

$$c_i(\boldsymbol{t}^{(k)}) = C(\boldsymbol{t}_i^{(k)}, x_i) + L\frac{\theta_r(\boldsymbol{t}_i^{(k)}) - \theta_r(\boldsymbol{t}_i^{(k-1)})}{\boldsymbol{t}_i^{(k)} - \boldsymbol{t}_i^{(k-1)}}. \tag{2.13}$$

We note that an advantage of this definition is that it does not compute temporal averaging of the heat capacity, and hence reduces numerical computations, and at the same time preserves numerical accuracy of the original idea. Even though that we avoid direct computation of the derivative $d\theta/dT$ by replacing it by the finite difference in (2.13), the calculation of $d\theta/dT$ is still necessary to obtain a solution of the adjoint model used to construct the gradient of the cost function.

We emphasize again that $\theta(T)$ is not a continuously differentiable function, and hence some regularization of θ is required to avoid lost of accuracy in solving the adjoint problem. We propose the following regularization of the unfrozen water content $\theta(T)$ in (2.2):

$$\theta_r(T) = \eta |T_*|^b |r(T)|^{-b}, \qquad r(T) = T_* + \begin{cases} (T - T_*)e^{-\alpha(T-T_*)^{-2}} & T < T_* \\ 0 & T \geq T_* \end{cases},$$

where if $\alpha \to 0$ then $r(T) \to \min(T, T_*)$, and hence $\theta_r(T) \to \theta(T)$, see Figure 2.7. Here, $r(T)$ is an infinitely differentiable function, and consequently θ posses the same property. One of the advantages of this is that we increase a convergence rate of solving the non-linear heat equation (2.12) by Richardson iterations, precisely find a solution to the adjoint problem, and hence find the location of the global minimum more faster than without regularization.

Bibliography

Alifanov, O. (1995), *Inverse Heat Transfer Problems*, 348 pp., Springer-Verlag, Berlin.

Alifanov, O., E. Artyukhin, and S. Rumyantsev (1996), *Extreme Methods for Solving Ill-Posed Problems with Application to Inverse Heat Transfer Problems*, 306 pp., Begell House, New York.

Andersland, O., and D. Anderson (1978), *Geotechnical Engineering for Cold Regions*, 566 pp., McGraw-Hill.

Anderson, D., and N. Morgenstern (1973), Physics, chemistry and mechanics of frozen ground: a review, in *Proceedings of the 2nd International Conference on Permafrost*, pp. 257–288, Yakutsk, USSR.

Anderson, T., and G. Thomson (1992), *The Inverse Problem of the Calculus of Variations for Ordinary Differential Equations*, 110 pp., American Mathematical Society, Providence.

Arnold, C., and C. Dey (1986), Observing systems simulation experiments: past, present, and future, *B. Am. Meteorol. Soc.*, *67*, 687–695.

Beck, A. (1988), *Handbook of Terrestrial Heat Flow Density Determination*, chap. Methods for determining thermal conductivity and thermal diffusivity, pp. 87–124, Kluwer, Dordrecht.

Beck, J. (1964), The optimum analytical design of transient experiments for simultaneous determinations of thermal conductivity and specific heat, Ph.D. Thesis, Michigan State University.

Beck, J., and K. Arnold (1977), *Parameter Estimation in Engineering and Science*, 501 pp., Wiley, New York.

Beck, J., C. S. Clair, and B. Blackwell (1985), *Inverse Heat Conduction: Ill-Posed Problems*, 326 pp., Wiley, New York.

Bengtsson, L., M. Ghil, and E. Källén (1981), *Dynamic Meteorology: Data Assimilation Methods*, 330 pp., Springer-Verlag, New York.

Birch, F. (1950), Flow of heat in the front range, colorado, *Geol. Soc. Am. Bull.*, *61*, 567–630.

Blackmon, M., Y. Lee, and J. Wallace (1984), Horizontal structure of 500-mb height fluctuations with long, intermediate and short-time scales, *J. Atmos. Sci.*, *41*(6), 961–979.

Boike, J., and K. Roth (1997), Time domain reectometry as a field method for measuring water content and soil water electrical conductivity at a continuous permafrost site, *Permafrost Periglac.*, *8*, 359–370.

Carslaw, H., and J. Jaeger (1959), *Conduction of Heat in Solids*, 520 pp., Oxford University Press, London.

Carson, J. (1963), Analysis of soil and air temperatures by fourier techniques, *J. Geophys. Res.*, *68*, 2217–2232.

Da-Xin, L. (1986), Non-linear fitting method of finding equilibrium temperature from BHT data, *Geothermics*, *15*, 657–664.

Dalhuijsen, A., and A. Segal (1986), Comparison of finite element techniques for solidification problems, *Int. J. Numer. Meth. Eng.*, *23*, 1807–1829.

de Vries, D. (1963), *W.R. van Wijk (editor) Physics of the Plant Environment*, chap. Thermal properties of soils, pp. 210–235, Wiley, New York.

DuChateau, P. (1996), *Parameter Identification and Inverse Problems in Hydrology, Geology and Ecology*, 324 pp., Kluwer, Dordrecht.

Fletcher, R. (2000), *Practical Methods of Optimization*, 450 pp., Wiley.

Galushkin, Y. (1997), Numerical simulation of permafrost evolution as a part of sedimentary basin modeling: permafrost in the pliocene-holocene climate history of the urengoy field in the west siberian basin, *Can. J. Earth Sci.*, *34*, 935–948.

Gardner, W. (1986), *Methods of Soil Analysis, Part 1: Physical and Mineralogical Methods*, chap. Water content, pp. 493–544, 2nd ed., American Society of Agronomy, Soil Science Society of America, Madison, WI.

Ghil, M., and P. Malanotte-Rizzoli (1991), Data assimilation in meteorology and oceanography, *Adv. Geophys.*, *33*, 141–266.

Gladwell, G. (1993), *Inverse Problems in Scattering: An Introduction*, 380 pp., Kluwer, Dordrecht.

Herzen, R. V., and A. Maxwell (1959), The measurement of thermal conductivity of deep-sea sediments by a needle-probe method, *Geophys. Res. Lett.*, *64*, 1557–1563.

Hinkel, K. (1997), Estimating seasonal values of thermal diffusivity in thawed and frozen soils using temperature time series, *Cold Reg. Sci. Technol.*, *26*, 1–15.

Hinzman, L., D. Kane, R. Gleck, and K. Everett (1991), Hydrological and thermal properties of the active layer in the alaskan arctic, *Cold Reg. Sci. Technol.*, *19*, 95–110.

Hurley, S., and R. J. Wiltshire (1993), Computing thermal diffusivity from soil temperature measurements, *Computers and Geosciences*, *19*, 475–477.

Jarny, Y., M. Özişik, and J. Bardon (1991), General optimization method using adjoint equation for solving multidimensional inverse heat conduction, *Int. J. Heat Mass Tran.*, *34*, 2911–2919.

Kane, D., K. Hinkel, D. Goering, L. Hinzman, and S. Outcalt (2001), Non-conductive heat transfer associated with frozen soils, *Global Planet. Change*, *29*, 275–292.

Kersten, M. (1949), *Thermal properties of soils*, Bulletin 28, 277 pp., University of Minnesota, Engineering Experiment Station.

Kudryavtsev, V. (1978), *Obshcheye Merzlotovedeniya (General Permafrost Science)*, 404 pp., Moscow University Editions, Moscow, in Russian.

Lachenbruch, A., and B. Marshall (1986), Changing climate: geothermal evidence from permafrost in the alaskan arctic, *Science*, *234*, 689–696.

Lachenbruch, A., J. Sass, B. Marshall, and T. Moses (1982), Permafrost, heat flow, and the geothermal regime at prudhoe bay, alaska, *J. Geophys. Res.*, *87*(B11), 9301–9316.

Lide, D. (1999), *Handbook of Chemistry and Physics*, 79 ed., 2576 pp., CRC.

Lovell, C. (1957), Temperature effects on phase composition and strength of partially frozen soil, *Highway Research Board Bulletin*, *168*, 74–95.

Lunardini, V. (1987), *Freezing of soil with an unfrozen water content and variable thermal properties*, CRREL Report, vol. 88-2, 30 pp., US Army Cold Regions Research and Engineering Lab.

Marchuk, G. (1995), *Adjoint Equations and Analysis of Complex Systems*, 484 pp., Kluwer Academic Publication.

McGaw, R. W., S. I. Outcalt, and E. Ng (1978), Thermal properties of wet tundra soils at barrow, alaska, in *Proceedings of 3rd International Conference on Permafrost*, vol. 1, pp. 47–53, National Research Council of Canada, Ottawa,Canada.

Murio, D. (1993), *The Mollification Method and the Numerical Solution of Ill-Posed Problems*, 272 pp., Wiley, New York.

Muzylev, N. (1985), The uniqueness of a solution to an inverse nonlinear heat conduction problem, *Zhurnal Vychislitel'noi Matematiki i Matematicheskoi Fiziki*, *25*, 1346–1352, in Russian.

Nagler, R. (1965), Transient techniques for determining the thermal conductivity of homogeneous polymeric materials at elevated temperatures, *J. Appl. Polym. Sci.*, *9*, 801–819.

Nicolsky, D., V. Romanovsky, and G. Tipenko (2007), Using in-situ temperature measurements to estimate saturated soil thermal properties by solving a sequence of optimization problems, *The Cryosphere*, *1*, 14–58.

Osterkamp, T., and V. Romanovsky (1996), Characteristics of changing permafrost temperatures in the alaskan arctic, usa, *Arctic Alpine Res.*, *28*, 267–273.

Osterkamp, T., and V. Romanovsky (1997), Freezing of the active layer on the coastal plain of the alaskan arctic, *Permafrost Periglac.*, *8*(1), 23–44.

Ouyang, T. (1992), Analysis of parameter estimation heat conduction problems with phase change using the finite element method, *Int. J. Numer. Meth. Eng.*, *33*(10), 2015–2037.

Panteleev, G., B. deYoung, C. Reiss, and C. Taggart (2004), Passive tracer reconstruction as a least squares problem with a semi-lagrangian constraint: an application to fish eggs and larvae, *J. Mar. Res.*, *62*, 787–814.

Pavlov, A., P. Permyakov, and A. Stepanov (1980), Determination of the thermophysical characteristics of alternatively freezing and thawing dispersed media by the method of solving inverse problems of heat conduction, *Journal of Engineering Physics and Thermophysics*, *39*, 885–889.

Permyakov, P. (2004), Methods of determining the characteristics of dispersed media at a phase transition, *Russian Physics Journal*, *47*(3), 240–246.

Romanovsky, V., and T. Osterkamp (1995), Interannual variations of the thermal regime of the active layer and near-surface permafrost in northern alaska, *Permafrost Periglac.*, *6*, 313–335.

Romanovsky, V., and T. Osterkamp (1997), Thawing of the active layer on the coastal plain of the alaskan arctic, *Permafrost Periglac.*, *8*, 1–22.

Romanovsky, V., and T. Osterkamp (2000), Effects of unfrozen water on heat and mass transport processes in the active layer and permafrost, *Permafrost Periglac.*, *11*, 219–239.

Romanovsky, V., and T. Osterkamp (2001), *(eds), R. Paepe and V. Melnikov, Permafrost Response on Economic Development, Environmental Security and Natural Resources*, chap. Permafrost: changes and impacts, pp. 297–315, Kluwer Academic.

Sass, J., A. Lachenbruch, and R. Munroe (1971), Thermal conductivity of rocks from measurements on fragments and its application to heat-flow determinations, *J. Geophys. Res.*, *76*(14), 3391–3401.

Schröter, J. (1989), *In D.L. Anderson and J. Willebrand, Oceanic Circulation Models: Combining Data and Dynamics*, chap. Driving of nonlinear time dependent ocean models by observation of transient tracers - A problem of constrained optimization., pp. 257–285, Kluwer Academic.

Silliman, S., and C. Neuzil (1990), Borehole determination of formation thermal conductivity using a thermal pulse from injected fluid, *J. Geophys. Res.*, *95*(B6), 8697–8704.

Somerton, W. (1992), *Thermal Properties and Temperature-Related Behavior of Rock/Fluid Systems*, no. 37 in Developments in Petroleum Science, 258 pp., Elsevier, Amsterdam.

Thacker, W. (1989), The role of the hessian matrix in fitting models to measurements, *J. Geophys. Res.*, *94*, 6177–6196.

Thacker, W., and R. Long (1988), Fitting dynamics to data, *J. Geophys. Res.*, *93*(2), 1227–1240.

Tikhonov, A., A. Leonov, and A. Yagola (1996), *Nonlinear Ill-Posed Problems*, 392 pp., Chapman & Hall, London.

Topp, G., and P. Ferre (2002), *Methods of Soil Analysis Part 4, Physical Methods*, chap. Water content, pp. 417–545, SSSA Book Series No. 5, Soil Science Society of America, Madison, WI.

Topp, G. C., J. L. Davis, and A. P. Annan (1980), Electromagnetic determination of soil water content: measurements in coaxial transmission lines, *Water Resour. Res.*, *16*, 574–582.

Watanabe, K., and M. Mizoguchi (2002), Amount of unfrozen water in frozen porous media saturated with solution, *Cold Reg. Sci. Technol.*, *34*, 103–110.

Wilhelm, H. (1990), A new approach to the borehole temperature relaxation method, *Geophys. J. Int.*, *103*(2), 469–481.

Williams, P. (1967), *Properties and behaviour of freezing soils*, 120 pp., Norwegian Geotechnical Institute, Publ. 72.

Wunsch, C. (1996), *The Ocean Circulation Inverse Problem*, 458 pp., Cambridge University Press, Cambridge.

Yershov, E. (1998), *General Geocryology*, 604 pp., Cambridge University Press, Cambridge.

Yoshikawa, K., P. Overduin, and J. Harden (2004), Moisture content measurements of moss (sphagnum spp.) using commercial sensors, *Permafrost Periglac.*, *15*, 309–318.

Zhang, T. (1993), Climate, seasonal snow cover and permafrost temperatures in alaska north of the brooks range, Ph.d. thesis, University of Alaska.

Zhang, T., and T. E. Osterkamp (1995), Considerations in determining the thermal diffusivity from temperature time series using finite difference methods, *Cold Reg. Sci. Technol.*, *23*, 333–341.

Zienkiewicz, O., and R. Taylor (1989), *The Finite Element Method*, vol. 1, 648 pp., McGraw-Hill, London.

Table 2.1: Range of thermal properties for common soil types at the North Slope, Alaska.

Layer	Thermal conductivity, λ_f	Porosity, η	b in (2.2)	T_* in (2.2)
Mineral-organic mixture	$[0.7, 1.8]$	$[0.2, 0.6]$	$[0.8, 0.5]$	$[-0.05, -0.01]$
Mineral soil(silt)	$[1.3, 2.4]$	$[0.2, 0.4]$	$[0.7, 0.5]$	$[-0.1, -0.01]$
Mineral soil(gravel)	$[2.5, 3.5]$	$[0.2, 0.4]$	$[0.7, 0.5]$	$[-0.1, -0.01]$
Mineral soil(shale)	$[1.0, 2.0]$	$[0.1, 0.3]$	$[0.7, 0.5]$	$[-0.1, -0.01]$

Table 2.2: Thermal properties of the ground material estimated from the best fit of the numerical model to the data

West Dock site

Depth	Soil type	λ_f	η	b	T_*
0.3-1.0	silt	1.86±0.01	0.34±0.01	0.75±0.01	−0.045±0.001
1.0-8.5	silt/sand/gravel	3.21±0.03	0.14±∞		
8.5-50.0	gravel/sand	3.57±0.05			

Deadhorse site

Depth	Soil type	λ_f	η	b	T_*
0.3-1.0	silt/sand	2.37±0.01	0.38±0.01	0.61±0.01	−0.045±0.001
1.0-2.7	sand/silt	3.27±0.04	0.11±∞		
2.7-27.0	gravel	3.84±0.03			
27.0-50.0	sand/gravel	3.50±0.06			

Franklin Bluffs site

Depth	Soil type	λ_f	η	b	T_*
0.3-1.2	silt	2.03±0.01	0.32±0.01	0.56±0.01	−0.029±0.001
1.2-14.0	gravel	3.64±0.03	0.14±∞		
14.0-17.0	silt	1.04±0.04			
17.0-21.0	shale	0.90±0.05			
21.0-50.0	silt/shale	1.03±0.05			

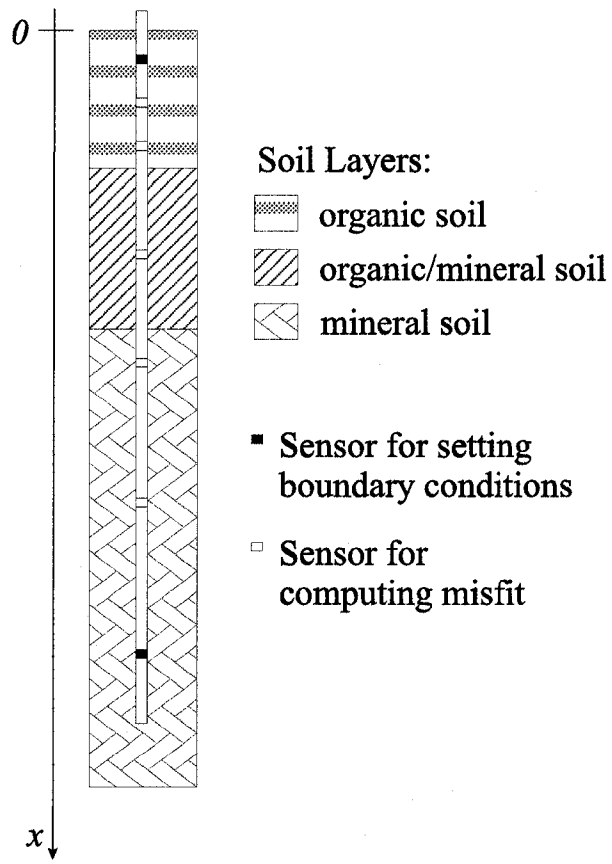

Figure 2.1: A schematics of a typical installation for measurement of soil temperature, with sensors located at different soil layers.

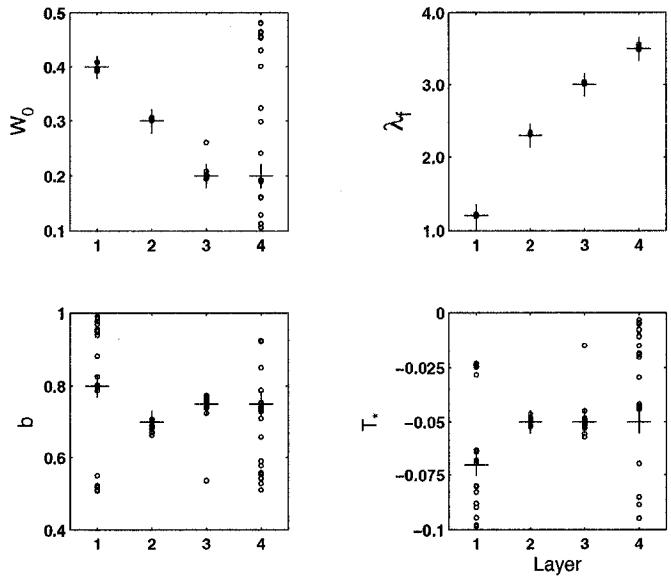

Figure 2.2: Recovered thermal properties and soil porosity in the twin experiment. The circles are recovered values, the crosses are the true values.

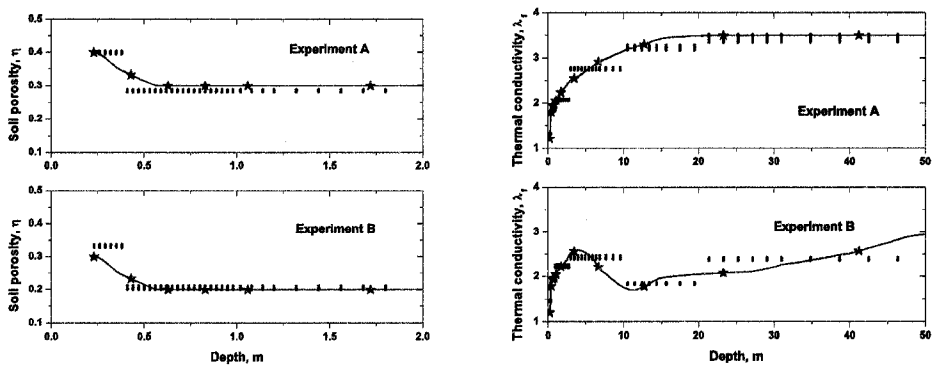

Figure 2.3: Volumetric water content (left) and thermal conductivity (right) used to compute true temperature data are marked by lines with stars. The dots are related to recovered values under assumption that the soil properties are constants within each soil layer.

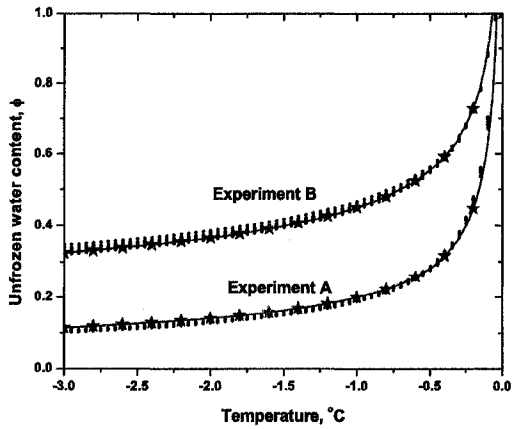

Figure 2.4: The true parametrization of unfrozen water content is marked by lines with stars. Dotted lines are recovered unfrozen water content for experiments **A**and **B**.

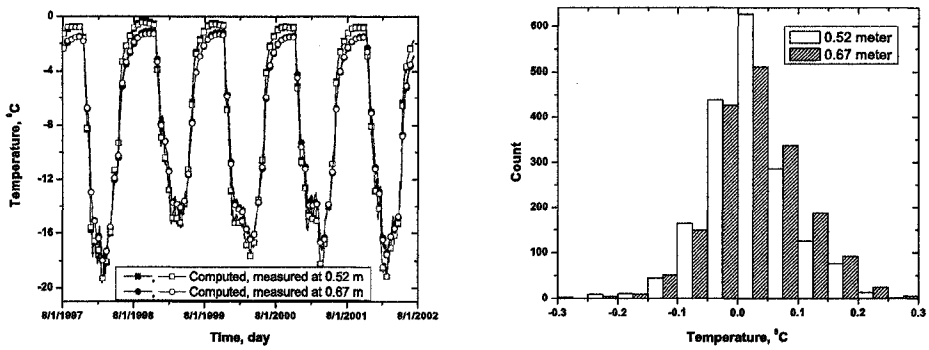

Figure 2.5: Measured and optimally computed soil temperature dynamics at 0.52 and 0.68 meter depth the West Dock site are shown at the left plot. The histogram of differences between the measured and computed temperature dynamics are plotted at the right.

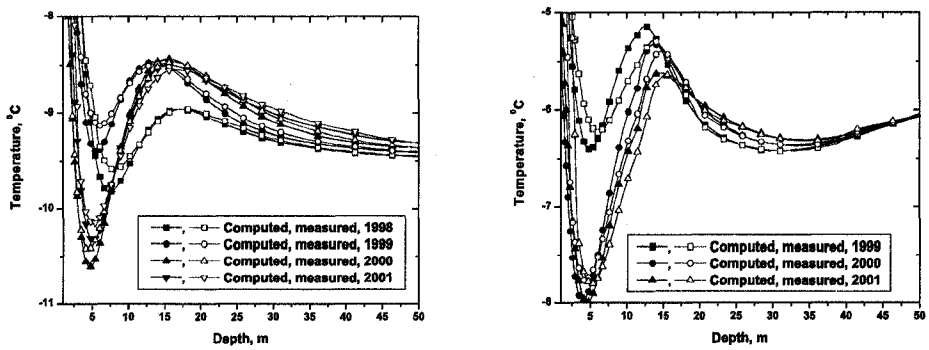

Figure 2.6: Measured and computed soil temperature profiles at a bore hole at the West Dock (left) and Franklin Bluffs site (right) during several consecutive years.

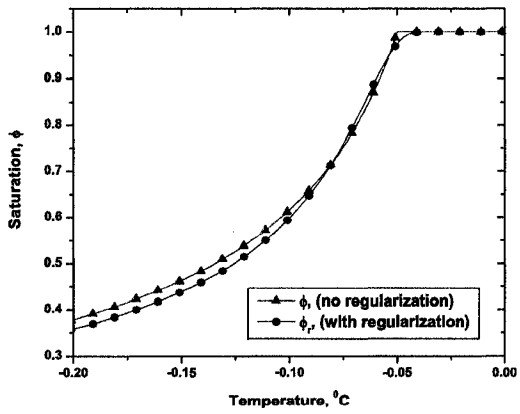

Figure 2.7: Dependence of non-regularized ϕ and regularized ϕ_r saturation on temperature.

Chapter 3

Modeling biogeophysical interactions in non-sorted circles in the Low Arctic[3]

3.1 Abstract

We investigate bio-geophysical processes that cause differential frost heave in non-sorted circles north of the Alaska's Brooks Range. The main objective is the development of a numerical thermo-mechanical model of a non-sorted circle. The presented model includes mass, momentum, and energy conservation laws for water, ice and soil. We applied this model to simulate differential frost heave at the Franklin Bluffs site and obtained a good quantitative agreement with measured dynamics of soil temperature, water content, and frost heave. For other locations such as at the Sagwon Bluffs and Howe Island sites we obtained qualitative agreement with frost heave measurements. The performed sensitivity analysis shows that the most active development of differential frost heave occurs for non-sorted circles within waterlogged areas, as observed in field measurements. For well drained sites, model results and field observations show that the differential frost heave is much smaller in magnitude compared to that of the water-logged sites. Sensitivity of the presented model with respect to alternation of the vegetation cover shows that a strong heterogeneity in the vegetation cover promotes active development of the differential frost heave. For non-sorted circles with vegetation on top of the circle, the computed differential heave is less pronounced. The radius of the non-sorted circle influences the magnitude of the frost heave. The maximum computed frost heave in the center of the non-sorted circle corresponds to 1-1.5 meter diameter non-sorted circles. For non-sorted circles with larger diameters, computed frost heave in the center of a circle is smaller compared to the heave at the circle circumference. This phenomenon promotes development of live vegetation in the center of the non-sorted circle, as observed in nature.

3.2 Introduction

Extensive areas of the Arctic landscape are characteristically patterned into small-scale ground features called non-sorted circles. Non-sorted circles are 0.5 to 3.0 meter diameter patches of barren or sparsely vegetated soil formed by frost action (*van. Everdingen R.*, 2005) and ordinarily develop on poorly drained tundra sites, see Figure 3.1. These features are associated with development of specific micro-relief, vegetation, and soil that strongly

[3] D.J. Nicolsky, V.E. Romanovsky, G.S. Tipenko and D.A. Walker, "Modeling biogeophysical interactions in non-sorted circles in the Low Arctic", in review, Journal of Geophysical Research - Biogeoscience.

affect the active-layer thermal and hydrological properties, and soil microclimate. Therefore, they are an important component of the Arctic landscape. Changes to these systems in relation to changes in climate could affect energy and carbon mass exchange at the tundra surface with possible feedbacks to the climate. However, the formation, development, maintenance of such ground patterns, and their interaction with vegetation is poorly understood (*Walker et al.*, 2004). The objective of this study is to numerically model observed frost heave in non-sorted circles and gain understanding of interactions between water fluxes, temperature dynamics as influenced by the plant canopy, and the motion of soil particles and as a result the heave of ground surface.

As a part of the biocomplexity of patterned ground project (*Walker*, 2007), we observed non-sorted circles at several locations near the Dalton Highway in Alaska (Figure 3.2). We instrumented several non-sorted circles at these sites with sensors that measure soil temperature, moisture content and the maximum frost heave (*Walker et al.*, 2004). Our measurements revealed that the maximum frost heave in a circle interior was 2 to 8 times greater compared to frost heave of the tundra surrounding the circle, (see the right plot in Figure 3.2). This phenomenon is referred to as the differential frost heave. The largest frost heave occurred in poorly drained circles with fine-grained sediments at Franklin Bluffs and Sagwon Bluffs. In contrast, at a site with near surface gravel deposits and available water supply near West Dock, Alaska North Slope, we observed no signs of non-sorted circle occurrence, and at a well drained site with fine sediment located at Howe Island, we observed "non-heaving" non-sorted circles.

Our field observations support the idea that the frost heave of saturated soil often cannot be explained solely by the expansion of liquid water transforming into ice crystals. It has been shown that under freezing conditions, liquid water can be transported towards the partially frozen soil (*Powers and Helmuth*, 1953; *Litvan*, 1972; *Williams and Smith*, 1989; *Dash et al.*, 1995). At temperatures below 0 °C confined water can partially remain liquid provided that it has lower pressure relative to the adjacent ice, provoking in turn a cryogenic suction of distant water from the unfrozen soil. This type of liquid water transport has been identified as the driving force of the frost heave (*Taber*, 1918, 1929, 1930). Other early contributions to frost heave research are described in (*Beskow*, 1935). Although the systematic studies were initiated in 1920s, efforts towards producing predictive tools did not start till decades later. One approach described frost heave capillary theory based on the Laplace surface tension formula (*Penner*, 1959; *Everett*, 1961). Similar ideas were explored

in (*O'Neill and Miller*, 1985; *Fowler*, 1989), where it was suggested that the transport of unfrozen liquid water is due to water pressure gradients arising from temperature-dependent variations in the curvature of the pore ice-water interfaces. In addition to the curvature-pressure model, there are other numerous experimental (*Williams*, 1982; *Watanabe and Mizoguchi*, 2000; *Viklander and Eigenbrod*, 2000) and theoretical (*Konrad and Morgenstern*, 1981; *Wettlaufer and Worster*, 1995; *Li et al.*, 2002; *Peterson and Krantz*, 2003; *Rempel et al.*, 2004; *Coussy*, 2005; *Michalowskin and Zhu*, 2006) studies of freezing ground, but many of them lack description of soil rheology. In this study we apply a general thermo-mechanical model (*Blanchard and Fremond*, 1982; *Frémond and Mikkola*, 1991; *Mikkola and Hartikainen*, 2001) of frost heave to simulate the observed frost heave in non-sorted circles. In this paper, we assume that the soil is a homogeneous mixture of liquid water, ice and soil skeleton. We assume that the skeleton and ice undergo small deformations described by linear elasticity, and the linear momentum conservation principles can be exploited in the quasi-static from. In our model, we also neglect ice flow relative to the soil skeleton. The body forces due to gravity are neglected too. The liquid water is an incompressible and non-viscous fluid that changes its phase and is always in thermodynamical equilibrium with ice. The chemical potential of the liquid water is modified due to adsorption to the soil skeleton.

Based on observations from field experiments and results of our numerical simulations, we conclude that heterogeneity in surface characteristics and soil properties due to the presence of a heterogeneous plant canopy together with presence of water-logged conditions are among the primarily requirements necessary for occurrence of differential frost heave observed in non-sorted circles. In this chapter we provide a description of non-sorted circles, a numerical model of the frost heave, and sensitivity study of the developed numerical model. Section-wise this chapter is organized as follows. In Section 3.3, we highlight key physical processes and mechanisms presumably causing the differential frost heave in non-sorted circles. In Section 3.4, we briefly review a general thermo-mechanical model of soil freezing. In Section 3.5, we summarize the system of governing equations, parametrization of soil properties, and boundary conditions. Section 3.6 addresses the finite element implementation of the thermo-mechanical model of soil freezing. In Section 3.7, we focus on hydrologically closed systems, in which the cryogenic forces causing the water migration are not considered. In Section 3.8, we analyze effects of the cryogenic suction in hydrologically open and closed systems. In Section 3.9, we apply the model to a specific non-sorted circle

located at the Franklin Bluffs site. In Section 3.10, we evaluate sensitivity of the model with respect to soil properties, and its geometrical dimensions. Finally, in Section 3.11, we provide conclusions and state the main results.

3.3 Physical description of non-sorted circles and involved physical processes

In this section, we highlight key physical processes and mechanisms presumably causing the differential frost heave in non-sorted circles. Before proceeding to this task we provide some definitions and describe soil thermal, hydrological and rheological properties.

The area surrounding the circle is called the inter-circle area and has a relatively thick mat of vegetation as well as a layer of organically enriched soil (see Figure 3.1). Incorporation of the organic material into soil leads to heterogeneity in thermal properties, structure and water holding capacity of soil. For example, different soil textures indicate distinctive thermal conductivities, soil porosity, and dependence of the unfrozen liquid water content on temperature. Besides variances in thermal and hydrological properties, the non-sorted circle has heterogeneous rheological properties due to structural change that takes place during annual freeze-thaw cycles. This structural change is caused by freezing water that creates a microscopic structure in a form of a sequence of ice lenses. Figure 3.3 shows the ice lenses in a soil core samples from a non-sorted circle at the Franklin Bluffs site, Alaska. Each ice lens separates soil particles, causes the observed lenticular soil structure, and hence lessen structural solidity of soil. *Graham and Au* (1985) and *Qi et al.* (2006) showed that soil has a long-term memory of its previous freeze/thaw cycles, which in particular reduce bonding between soil particles. To account for the reduction in bonding, we assume that the soil is more structurally solid if it has fewer ice lenses. From a soil core obtained by drilling in winter, we observed that the circle has many more ice lenses than in the inter-circle area, and these lenses can be found even at the significant depth of 0.5 meters (see Figure 3.3). Therefore, we assume that soil in the inter-circle is more structurally solid than in the circle. Despite these heterogeneities, the difference between observed active-layer depths (maximum depth of summer thaw) of the circle and inter-circle does not exceed 0.3 meters in the majority of cases.

It is well known that frost heave is caused by volumetric water expansion during freezing. However, as mentioned earlier, the observed frost heave heights do not seem to be exclusively dependent on the active-layer depth, and on volumetric water content in the soil before freezing. For example, from field observations at the Franklin Bluffs site, we know that

the active-layer thicknesses for the circle and inter-circle areas are 0.9 and 0.8 meters, respectively, and volumetric water content in these areas during summer is almost the same. Therefore, if water does not migrate, the frost heave is computable and its height is about 3.0-3.5 cm for both circle and inter-circle areas, which contradicts the observations within a circle at Franklin Bluffs site, see Figure 3.2. Thus, we hypothesize that the key physical process responsible for the differential frost heave is *water redistribution in the non-sorted circle* due to heterogeneity in soil properties and in ground surface conditions, first of all in vegetation cover. In Figure 3.4, we show fundamental physical processes occurring in the non-sorted circle in the fall when it freezes. We describe nature of these processes and their implications to the observed values of the differential frost heave as follows.

When the ground surface temperature becomes lower than 0 °C water, trapped in soil pores starts to freeze, in Figure 3.4 the direction of the heat flux during freezing is shown by red dashed arrows. In several classical works, it was demonstrated that gradual freezing of water at sub-zero temperatures which takes place under temperature gradients create cryogenic suction inducing flow of water towards a freezing region along the temperature gradient (e.g., *O'Neill and Miller*, 1985). Since the circle lacks an organic layer, frost propagates through it faster, causes stronger water migration into the circle, and consequently results in more intensive ice-lens formation, and results in more frost heave within the circle than in the inter-circle area. A secondary consequence of the heave is the reduced thickness of the snowpack above the circle compared to the inter-circle area (Figure 3.4). The heterogeneous snow distribution further enhances the thermal heterogeneity of the soil surface. An absence of a vegetation mat within the heaving areas in conjunction with difference in the snow thickness results in observed lower winter soil temperatures in the circle than in the inter-circle. The thermal difference between the circle and inter-circle areas affects cryogenic suction and drives water movement from the inter-circle to the circle (the direction of liquid water motion is shown by blue solid arrows). Reaching a freezing region, water forms ice lenses which exert uplifting forces causing deformation of the soil skeleton. We highlight directions of soil particle velocities by black dash-dotted arrows in Figure 3.4. In our model we exploit a simplest rheological model of the soil skeleton and assume that its deformations are well simulated by linear elasticity theory, in which the soil stiffness takes into account structural differences and lessened soil bonding caused by the ice lenses.

Besides the thermal differences which cause liquid water migration towards the circle, hydraulic properties of the soil also determine a water flux affecting the liquid water mi-

gration. One of the key hydraulic parameters is the coefficient of hydraulic conductivity k_h and its dependence on unfrozen water content for partially frozen ground. In this study we exploit parametrization of k_h given by

$$k_h = k_0 \theta_w^{\alpha}, \tag{3.1}$$

where k_0 is the hydraulic conductivity of the thawed soil, θ_w is the volumetric liquid water content and $\alpha \in [3, 9]$ (*Konrad and Duquennoi*, 1993). Analyzing this formula we conclude that the hydraulic conductivity k_h increases with an increase of unfrozen water content θ_w, a function of both temperature and porosity. Another hydrological soil property that is important to sustain water migration is the availability of water inside the non-sorted circle or at its boundary. Note that from observations it is known that the higher values of frost heave have been measured at poorly drained sites. Therefore, lateral boundary conditions play an important role in allowing water to migrate into the circle due to cryogenic suction and to create ice lenses. In our model, we simulate the non-sorted circles either as hydrologically open or closed systems by setting to zero either the pressure or water flux, respectively, on external boundaries. In the next section, we will briefly describe the general thermo-mechanical model of freezing soil. An interested reader can consult other works, where the theory is discussed in detail (*Hartikainen and Mikkola*, 1997; *Mikkola and Hartikainen*, 2001; *Jussila*, 2006).

3.4 Review of a general thermo-mechanical model of soil freezing

We consider a mixture of several constituents: water w, ice i and soil s particles occupying a region Ω_t in space at time t, see right plot in Figure 3.5. We assume that at each point of Ω_t constituents coexist with each other and each of them occupies a part V_k, $k \in \{w, i, s\}$ of a representative volume V in Ω_t. We mark all quantities related to the k-th constituent with subscript k and denote by θ_k the volume fraction satisfying $\theta_k V = V_k$. Note that the non-negative volume fractions also satisfy the saturation condition

$$\theta_i + \theta_w + \theta_s = 1, \tag{3.2}$$

or equivalently $\eta + \theta_s = 1$, where $\eta = \theta_w + \theta_i$ is called the soil porosity. Assuming that all constituents are incompressible, the density ρ_k is equal to $\bar{\rho}_k \theta_k$, where $\bar{\rho}_w$=1000[2], $\bar{\rho}_i$=900, and $\bar{\rho}_s$ is a constant depending on the soil type.

[2]Units for all types of physical quantities are in the S.I. system of units, unless otherwise stated.

Denoting by $\boldsymbol{v}_k$ the spatial velocity, we formulate mass conservation principles for water, ice and soil particles as follows

$$\frac{\partial \rho_w}{\partial t} + \nabla\cdot(\rho_w \boldsymbol{v}_w) = \hat{\rho}, \qquad \frac{\partial \rho_i}{\partial t} + \nabla\cdot(\rho_i \boldsymbol{v}_i) = -\hat{\rho}, \qquad \frac{\partial \rho_s}{\partial t} + \nabla\cdot(\rho_s \boldsymbol{v}_s) = 0, \tag{3.3}$$

where $\hat{\rho}$ is the rate of mass exchange between liquid water and ice. Note that the quantity $\hat{\rho}$ is not zero only during freezing or thawing, when phase change between water and ice occurs. Taking into account that soil particles and ice move with the same velocity $\boldsymbol{v}_i = \boldsymbol{v}_s = \boldsymbol{v}$, we combine equations in (3.3) to derive

$$\nabla \cdot \big(\theta_w(\boldsymbol{v}_w - \boldsymbol{v})\big) + \nabla \cdot \boldsymbol{v} = -\gamma \frac{\hat{\rho}}{\bar{\rho}_i}, \qquad \gamma = 1 - \frac{\bar{\rho}_i}{\bar{\rho}_w}. \tag{3.4}$$

One of the variables in the water mass conservation laws (3.4) is $\boldsymbol{v}$, which can be calculated taking into account soil rheology. Since the ground heaves slowly with $\|\boldsymbol{v}\| \ll 1$, the velocity $\boldsymbol{v}$ can be approximated by $\boldsymbol{v} = \frac{\partial}{\partial t}\boldsymbol{u}$, where $\boldsymbol{u}$ is the displacement of soil particles, satisfying a quasi-static linear momentum conservation principle

$$\nabla \cdot \boldsymbol{\sigma} = 0, \qquad \boldsymbol{\sigma} = \hat{\boldsymbol{\sigma}} - \boldsymbol{I}P \tag{3.5}$$

where $\boldsymbol{\sigma}$ is the total stress tensor, $\hat{\boldsymbol{\sigma}}$ is the effective stress tensor, P is the pore pressure, and $\boldsymbol{I}$ stands for the identity second order tensors. Assuming that the soil is isotropic and undergoes small deformations, we approximate the effective stress tensor $\hat{\boldsymbol{\sigma}}$ as follows

$$\hat{\boldsymbol{\sigma}} = \frac{E}{1+\nu}\big(\boldsymbol{\epsilon} + \frac{\nu}{1-2\nu}\mathrm{tr}(\boldsymbol{\epsilon})\boldsymbol{I}\big), \qquad \mathrm{tr}(\boldsymbol{\epsilon}) = \nabla \cdot \boldsymbol{u}, \qquad \boldsymbol{\epsilon} = \frac{1}{2}\big(\nabla \boldsymbol{u} + (\nabla \boldsymbol{u})^t\big), \tag{3.6}$$

where $\boldsymbol{\epsilon}$ is the strain tensor, E and ν are the Young's modulus and Poisson's ratio of the soil, respectively. Here, the symbol t denotes the transpose operator.

Pore pressure P is defined in (*Mikkola and Hartikainen*, 2001) as

$$P = \sum_{k\in\{i,w,s\}} p_k, \tag{3.7}$$

where p_k is the thermodynamics pressure defined accordingly to

$$p_k = \theta_k \sum_{j\in\{w,i,s\}} \rho_j \frac{\partial \psi_j}{\partial \theta_k},$$

where ψ_k is the Hemlhotz free energy (*Landau and Lifshitz*, 1984). Considering a certain ansatz for the Hemlhotz free energy it is possible to derive that

$$p_k = \theta_k \Big[\rho_w \frac{LT}{T_0}\frac{\partial f}{\partial \theta_k} + p\Big], \tag{3.8}$$

where p can be considered as hydrostatic type of pressure, T is the soil temperature, T_0 is the temperature of water fusion and is 273.15 K, L is the latent heat of fusion, and f is a certain function of volume fractions described later in the chapter. A detailed discussion regarding the physical meanings of commonly occurring pressure terms p_k, p can be found in (*Bennethum and Weinstein*, 2004). Let us note that from a physical point of view the hydrostatic pressure p means restriction (3.2) of interpenetration of the constituents through each other (*Frémond and Mikkola*, 1991). Also, we emphasize that from (3.8) it is possible to derive a well-known relationship

$$\frac{p_w}{\theta_w} - \frac{p_s}{\theta_s} = \rho_w \frac{LT}{T_0}\Big[\frac{\partial f}{\partial \theta_w} - \frac{\partial f}{\partial \theta_s}\Big],$$

for a binary model consisting of liquid and solid. The right hand side can be interpreted as the surface tension of water in the pores.

The expression for the function f is based on the following arguments. Inside a pore, water is bound to the soil particles with the strength decreasing with distance from the pore wall. In terms of energy, it is possible to state that the energy of water decreases with distance from the soil particle (*Hobbs*, 1974; *Tsytovich*, 1975), or equivalently the more strongly bound water requires a lower temperature to freeze it. Therefore, freezing begins in the middle of the pore where the water is less bound and advances towards the pore walls while the temperature decreases. From private communications with J. Hartikainen and from *Mikkola and Hartikainen* (2001), the general shape of the function f should fulfill the following requirements: f increases as θ_w decreases and goes to infinity as θ_w approaches zero. This implies that a certain layer of the adsorbed water remains unfrozen for all temperatures. In the work (*Mikkola and Hartikainen*, 2001), the function f is given by

$$f(\chi) = a\left(\frac{1}{\chi} - 1\right)^2, \qquad \theta_w = \chi\eta \tag{3.9}$$

where the constant a can be determined by the Clapeyron relations. In the case of $|T - T_0| \ll T_0$, the Clapeyron relation is given by

$$\Big[L + (C_w - C_i)(T - T_0)\Big]\frac{T - T_0}{T_0} + \gamma\frac{p}{\rho_i} = L\frac{T}{T_0}\Big(f + \chi\frac{\partial f}{\partial \chi}\Big), \tag{3.10}$$

where C_w and C_i are the specific heat capacity of water and ice, respectively. This equation gives the relationship between the temperature T, the pressure p, the porosity n, and the relative water content χ. Formula (3.10) can also be used for experimental verification of the function f (*Hartikainen and Mikkola*, 1997).

Returning to the mass conservation principle for water (3.4), we express the velocity of water relative to soil particles by the generalized Darcy's law:

$$\theta_w(\boldsymbol{v}_w - \boldsymbol{v}) = -\frac{k_h}{g\bar{\rho}_w}\Big(\nabla\Big(\frac{p_w}{\theta_w}\Big) + \bar{\rho}_w\frac{LT}{T_0}\nabla f\Big),$$

or

$$\theta_w(\boldsymbol{v}_w - \boldsymbol{v}) = -\frac{k_h}{g\bar{\rho}_w}\Big(\nabla p + \mathcal{F}\Big), \qquad \mathcal{F} = \bar{\rho}_w L\Big(\nabla(\theta_w\frac{T}{T_0}\frac{\partial f}{\partial\theta_w}) + \frac{T}{T_0}\nabla f\Big), \tag{3.11}$$

where g is the gravitational acceleration, and the quantity $\mathcal{F}$ is a water flux due to the matric potential described in (*Huyghe et al.*, 2004). Note, in Terzaghi's consolidation theory the matric potential $\mathcal{F}$ is not considered. The quantity $\mathcal{F}$ vanishes in a homogeneous medium where variations in θ_w are small and the pore structure is coarse. However, near the 0 °C isoline where freezing occurs there is a large gradient of liquid water content θ_w, and consequently the value of $\mathcal{F}$ has to be taken into account.

Since the flux $\mathcal{F}$ depends on temperature, we consider the energy conservation principle for the entire mixture

$$L\hat{\rho} + C\frac{\partial T}{\partial t} = \nabla\cdot(\lambda\nabla T). \tag{3.12}$$

Here, C is the volumetric heat capacity, λ is the thermal conductivity, and the quantity $\hat{\rho}$ is calculated by exploiting the second and third equations in (3.3):

$$\hat{\rho} = \bar{\rho}_i\Big(\frac{\partial\theta_w}{\partial t} - \nabla\cdot\big((1-\theta_w)\boldsymbol{v}\big)\Big). \tag{3.13}$$

Note that for unfrozen soil θ_w is equal to η, whereas for partially frozen ground $\theta_w < \eta$ and is given by the unfrozen water content curve. This curve specifies the temperature dependence of θ_w in partially frozen ground.

3.5 System of governing equations, parametrization of soil properties and boundary conditions

In this section, we derive a system of governing equations, which is solved by the finite element method (*Zienkiewicz and Taylor*, 1989) in a certain domain. Since a non-sorted circle has an axial symmetry, we solve the governing equations in a 2-D domain, shown in the left plot in Figure 3.5. It is the radial cross-section of non-sorted circle from circle's axis of rotation OO' to a lateral boundary AB located in the inter-circle. The circle does not have organically enriched soil and consists of only mineral soil that is marked by 1. To describe soil structure in the inter-circle, we mark an organically enriched layer by number 2, and the mineral soil below it by 3.

We exploit the heat equation (3.12), mass exchange relationship (3.13) and $\theta_w = \theta_w(T, \eta)$ to obtain an equivalent form of the heat equation:

$$C\frac{\partial T}{\partial t} + \bar{\rho}_i L\Big(\frac{\partial \theta_w}{\partial T}\frac{\partial T}{\partial t} + (\frac{\partial \theta_w}{\partial \eta} - 1)\frac{\partial \eta}{\partial t}\Big) = \nabla \cdot (\lambda \nabla T) + \rho_i L \nabla \cdot (\alpha \frac{\partial \boldsymbol{u}}{\partial t}), \tag{3.14}$$

where $\alpha = \eta - \theta_w$ is non zero only for partially frozen soil. Introducing $\beta = \alpha\gamma - 1$, we substitute terms in the mass conservation principle (3.4) by expressions given in (3.11) and (3.13) to obtain an equation with respect to pore pressure p:

$$\gamma\Big(\frac{\partial \theta_w}{\partial T}\frac{\partial T}{\partial t} + (\frac{\partial \theta_w}{\partial \eta} - 1)\frac{\partial \eta}{\partial t}\Big) = \nabla \cdot \Big(\frac{k_h}{g\bar{\rho}_w}(\nabla p + \mathcal{F})\Big) + \nabla \cdot (\beta \frac{\partial \boldsymbol{u}}{\partial t}). \tag{3.15}$$

The above equation is supplemented by an equation

$$\nabla \cdot \hat{\boldsymbol{\sigma}} = \nabla P, \tag{3.16}$$

which relates the hydrostatic pressure p and deformation $\boldsymbol{u}$. Note that the equation pair (3.15-3.16) is commonly occurring in quasi-static poroelasticity theory. Finally, we include the mass conservation principle for the soil skeleton

$$\frac{\partial \eta}{\partial t} - \nabla \cdot \big((1 - \eta)\frac{\partial \boldsymbol{u}}{\partial t}\big) = 0 \tag{3.17}$$

with respect to soil porosity η=1$-\theta_s$ in order to close the above system of equations.

Depending on the choice of parameters λ, k_h, a, E, and C in (3.15-3.17), it is possible to simulate freezing of various types of soil. However, since we are interested in the modeling of non-sorted circles, we provide typical values of these parameters listed in Table 3.1 for sites along the Dalton Highway, Alaska. Besides the typical values, it is also important how these parameters are parameterized. In equation (3.14), the thermal conductivity λ and the volumetric heat capacity C are expressed according to *de Vries* (1963):

$$C = \rho_s C_s + \rho_w C_w + \rho_i C_i, \qquad \lambda = \lambda_s^{\theta_s} \lambda_w^{\theta_w} \lambda_i^{\theta_i},$$

where C_k and λ_k are the specific heat capacities and thermal conductivities, respectively. With respect to the rheological properties E and ν, we assume that the soil is consolidated, and hence the Young's modulus E for soil compression is twice as large as for its tension. Also, since area 3 has fewer ice lenses than areas 1 and 2, area 3 is more structurally solid and has a larger value of Young's modulus E. To find the value of the constant a in (3.9), we exploit the Clayperon equation (3.10) to express θ_w as a function of temperature and fit it to the measured unfrozen water content, see the left plot in Figure 3.6.

In order to solve the above system (3.15-3.17) of partial differential equations, it usually has to be supplemented by certain boundary conditions specified at the ground surface, some depth, and at lateral boundaries of the non-sorted circle. Before describing the boundary conditions, we recall that a single non-sorted circle is an axisymmetrical cylindrical object. Therefore, in order to reduce computational time, we model frost-heave dynamics in a 2-D domain with the axial symmetry. In Figure 3.5, right plot, we show a 2-D computational domain Ω_t associated with non-sorted circle and with an axis of rotation marked by OO'. We formulate the boundary conditions with respect to pressure, temperature, and soil particle displacement on the axis OO', the ground surface $\partial\Omega_{as}$, at the lateral boundary AB and at some depth OA as follows.

First, we consider boundary conditions with respect to temperature T. We assume that the lateral boundary AB is located far away from the circle, and there is no lateral heat flow, i.e. $\boldsymbol{\nu}\cdot(\lambda\nabla T)=0$, where $\boldsymbol{\nu}$ is the outward normal vector to the boundary. At the axis of rotation OO' due to symmetry principle, we impose no heat flux boundary conditions. At the ground surface $\partial\Omega_{as}$ and some depth OA the temperature is set according to its measured values. Our field observations reveal that the ground surface temperatures in a circle and the surrounding it inter-circle are almost constant in spatial directions. However, during freezing there is a notable jump in temperatures at the border between the circle and the inter-circle. Thus, we specify the ground surface temperature at inter-circle and circle by $T^{circle}_{surface}(t)$, and $T^{inter-circle}_{surface}(t)$, respectively. These temperatures were measured at 0.01 meter depth below the surface of mineral soil in the circle, and 0.01 meters below the surface of organic layer in the inter-circle. In Figure 3.6, we plot temperature dynamics of $T^{circle}_{surface}(x,t)$ and $T^{inter-circle}_{surface}(t)$. Note that the temperature $T^{circle}_{surface}(t)$ is typically colder than $T^{inter-circle}_{surface}(t)$, since the circle has a thinner snow cover and no insulative vegetation comparing to the inter-circle.

Second, we specify boundary conditions with respect to pressure p. Below, in Section 3.8, we show that this boundary conditions plays a decisive role in determining frost heave dynamics. Two standard boundary conditions for the pressure p are the Neumann, $\boldsymbol{\nu}\cdot\nabla p=0$, and the Dirichlet, $p=0$, boundary conditions. It is possible to check that if $\boldsymbol{\nu}\cdot\nabla p=0$ and $\boldsymbol{\nu}\cdot\nabla T=0$ are simultaneously specified on the boundary, then this boundary is water impermeable, and the condition $\boldsymbol{\nu}\cdot\theta_w(\boldsymbol{v}-\boldsymbol{v}_w)=0$ holds. On other hand $p=0$ models water permeable boundary but also leads to an additional force term into total stresses $\boldsymbol{\sigma}$ on the boundary and consequent soil deformations. The pore pressure boundary condition $P=0$

would be more realistic than p=0, but its implementation would require certain difficulties. Since we are interested in modeling the differential frost heave between the circle and inter-circle, we impose the lateral boundary condition on AB that is "far away" from the circle, i.e. all disturbances caused by $p = 0$ on the lateral boundary would not affect the solution in the circle.

For example, if liquid water is abundant in the area surrounding the non-sorted circle and it can flow into the non-sorted circle, then we model water-permeable boundary conditions by setting p=0 on the lateral boundary AB. However, if additional water is scarce or not available, and a flow of water into the non-sorted circle is negligibly small, then the water impermeable boundary condition $\boldsymbol{\nu} \cdot \theta_w(\boldsymbol{v} - \boldsymbol{v}_w)$=0 on AB is modeled by setting $\boldsymbol{\nu}\cdot\nabla p$=0 on AB. We note that $\boldsymbol{\nu}\cdot(\lambda\nabla T)$=0 is always set on AB because there is no heat flux across the lateral boundary. Thus, we define a system to be open if p=0 is set on AB, and closed if $\boldsymbol{\nu} \cdot \theta_w(\boldsymbol{v} - \boldsymbol{v}_w)$=0 is modeled on AB. On the axis OO' and OA we set no water flux boundary conditions. At the surface $\partial\Omega_{as}$, we assume that water can flow in and out of the domain Ω_t, i.e. p=0 on $\partial\Omega_{as}$.

Third, we describe boundary conditions with respect to displacement of soil particles. Since there are no physical loads applied to the ground surface and it can move freely, we set $\boldsymbol{\sigma}\cdot\boldsymbol{\nu}$=0 on $\partial\Omega_{as}$. On the lateral boundary AB, far away from the circle, we assume that the soil particles can move freely in vertical direction, but not in the horizontal one. Therefore, u_r=0, $\left(\boldsymbol{\sigma}\cdot\boldsymbol{\nu}\right)_z$=0 is set on AB. Due to symmetry we impose the same boundary condition on the axis of rotation OO': i.e. u_r=0, $\left(\boldsymbol{\sigma}\cdot\boldsymbol{\nu}\right)_z$=0. Note that since the segment OA is located in permafrost, no soil motion can occur, and hence $\boldsymbol{u}$=0. We summarize all boundary conditions in Table 3.2.

3.6 Finite element formulation and the fictitious domain method

At any time t, the mixture of water and soil particles occupying a domain Ω_t undergoes deformation, which leads to dynamic geometry of Ω_t. One of the techniques to solve the system of equations (3.15-3.17) in the changing-in-time domain Ω_t is to implement the fictitious domain method (*Glowinski et al.*, 1994). Following this ideology, we embed Ω_t into a larger fixed-in-time rectangle domain Ω (*Buzbee et al.*, 1971), area $OO''CA$ in Figure 3.5, right plot. A supplement of Ω_t in Ω is called the fictitious domain Ω_a=$\Omega\backslash\Omega_t$. From the physical point of view Ω_a is related to air which is being displaced by heaving ground. Note that as the soil surface heaves, some fixed points in Ω_a initially representing air are

to be associated with soil Ω_t. Therefore, the initial height of Ω_a has to be taller than the maximum displacement of the ground surface $\partial\Omega_{as}$ relative to its position prior to any heaving. An advantage of implementing the fictitious domain method is that the time consuming triangulation of Ω into triangles $\{\mathcal{K}\}$ is completed only once. A second advantage is that we solve the same set of equations (3.14-3.17) in both domains Ω_t and Ω_a.

We implement a standard finite element method (*Zienkiewicz and Taylor*, 1989) and partition the domain Ω into regular non-overlapping triangles $\{\mathcal{K}\}$ with vertices at $\{x_i\}_{i=1}^m$. We consider piece-wise linear continuous functions $\{\varphi_i(x) : x\in\Omega\}_{i=1}^m$, such that $\varphi_i(x_j)=\delta_{ij}$, $i,j=1,\ldots,m$, and $\varphi_i(\boldsymbol{x})$ is linear on each triangular. We expand physical variables T, p, θ_s and $\boldsymbol{u}$ in a basis of $\{\varphi_i\}$:

$$\mathcal{P}(x,t) \approx \sum_{i=1}^{m} \varphi_i(x)\mathcal{P}_i(t), \qquad x \in \Omega, \quad t \geq 0, \tag{3.18}$$

where $\mathcal{P}$ is one of the physical variables, and $\mathcal{P}_i$ is the value of $\mathcal{P}$ at the i^{th} node associated with x_i. Therefore the system of equation (3.14-3.17) can be discretized to form the following non-linear system of differential equations

$$\mathbf{M}\big(\mathbf{X}(t)\big)\,\frac{\partial \mathbf{X}(t)}{\partial t} = \mathbf{K}\big(\mathbf{X}(t)\big)\,\mathbf{X}(t) + \mathbf{F}(t), \qquad \mathbf{X}(0) = \mathbf{X}_0 \tag{3.19}$$

where $\mathbf{M}$ and $\mathbf{K}$ are sparse non-singular matrices, and $\mathbf{X}$ is a vector containing values of all physical variables at all nodes. To solve the system in (3.19) we utilize an implicit time scheme and Picard iterations (*Samarskii and Vabishchevich*, 1996)

$$\mathbf{M}(\mathbf{X}_{n+1})\Big(\mathbf{X}_{n+1} - \mathbf{X}_n\Big) = \Delta t_n\Big(\mathbf{K}(\mathbf{X}_{n+1})\mathbf{X}_{n+1} + \mathbf{F}(\mathbf{X}_{n+1})\Big), \quad \mathbf{X}_n = \mathbf{X}(t_n), \tag{3.20}$$

where t_n is the time at the n^{th} time step, and $\Delta t_n = t_{n+1} - t_n$ is the time increment. Given $\mathbf{X}_n$, we solve the non-linear equation (3.20) with respect to $\mathbf{X}_{n+1}$ by iterations $s = 0, 1, \ldots, s_0$. The iterations are started by the initial guess $\mathbf{X}_{n+1}^0 = \mathbf{X}_n$ and are terminated at s_0 when certain convergence criteria are met. The previous approximation $\mathbf{X}_{n+1}^s$ is used to compute the consecutive one $\mathbf{X}_{n+1}^{s+1}$ as follows. The value of $\mathbf{X}_{n+1}^s$ is used to evaluate the matrices $\mathbf{K}(\mathbf{X}_{n+1}^s)$ and $\mathbf{M}(\mathbf{X}_{n+1}^s)$ and the vector $\mathbf{F}(\mathbf{X}_{n+1}^s)$, which are then utilized to compute the solution $\mathbf{X}_{n+1}^{s+1}$ of

$$\mathbf{M}(\mathbf{X}_{n+1}^s)\Big(\mathbf{X}_{n+1}^{s+1} - \mathbf{X}_n\Big) = \Delta t_n\Big(\mathbf{K}(\mathbf{X}_{n+1}^s)\mathbf{X}_{n+1}^{s+1} + \mathbf{F}(\mathbf{X}_{n+1}^s)\Big)$$

at $s+1$ iteration. At each iteration the convergence criteria $\max_i |T_{n+1,i}^{s+1} - T_{n+1,i}^s| \leq \epsilon_1$ and $\max_i \|\boldsymbol{u}_{n+1,i}^{s+1} - \boldsymbol{u}_{n+1,i}^s\| \leq \epsilon_2$, is checked, where $\epsilon_1, \epsilon_2 > 0$. If it holds, iteration is terminated

at $s_0 = s_{n+1}$. If the number of iterations exceeds a certain number then the time increment Δt_n is halved. The convergence criteria is always reached if the time increment Δt_n is small enough (*Samarskii and Vabishchevich*, 1996).

Since the domain Ω_t is embedded into a larger domain Ω, we are not able to set boundary conditions on $\partial\Omega_{as}$ directly, since it is immersed in Ω. In the framework of the fictitious domain method, one of the ways to resolve this problem is given as follows (*Buzbee et al.*, 1971; *Astrakhantcev*, 1978; *Marchuk et al.*, 1986). First, we set certain boundary conditions on $\partial\Omega_a$ and then specify coefficients in (3.14-3.16) such that we have the conditions, listed in Table 3.2 on the surface $\partial\Omega_{as}$.

We deal with setting $T{=}T_{surface}$ on $\partial\Omega_{as}$ as follows. Note that the thermal conductivity λ is a positive scalar. Generally, however, it can be any positive definite matrix. Therefore, in order to set $T{=}T_{surface}$ on $\partial\Omega_{as}$, we impose $T{=}T_{surface}$ on the boundary $O''C$ (Figure 3.5, right) and set $L{=}0$, $\lambda{=}\mathrm{diag}(\lambda_x, \lambda_y)$ in Ω_a, where $0 < \lambda_x \ll 1$ and $1 \ll \lambda_y$ (*Saulev*, 1963; *Kuznetsov*, 2000; *Sergueev et al.*, 2003). Equivalent to setting the temperature on the ground surface $\partial\Omega_{as}$, we restrict the pressure $p{=}0$ on $\partial\Omega_{as}$ by letting $\rho_i{=}\rho_w$, $L{=}0$ and $k_h{\gg}1$ in Ω_a, and putting $p{=}0$ on segments OO'', $O''C$ and CB. Modeling $\boldsymbol{\sigma}\cdot\boldsymbol{\nu}{=}0$ on $\partial\Omega_{as}$ is done similarly to an approach described in *Ramiere et al.* (2005) by imposing the traction free boundary conditions $\boldsymbol{\sigma}\cdot\boldsymbol{\nu}{=}0$ on $\partial\Omega_f$, a small Young's modulus $0{<}E{\ll}1$ and zeroing out the internal body forces in the fictitious domain Ω_a.

Finally, we consider the continuity equation (3.17). Since there are no internal body forces in Ω_a and $\boldsymbol{\sigma}\cdot\boldsymbol{\nu}{=}0$ is on $\partial\Omega_a$ and $\partial\Omega_{as}$, $\boldsymbol{\sigma}{=}0$ holds in Ω_a. Therefore, $\nabla\cdot\boldsymbol{u}{=}0$ is in Ω_a. Taking a time derivative, we obtain $\nabla\cdot\boldsymbol{v}{=}0$, and hence the mass continuity equation (3.17) becomes an advection equation in Ω_a:

$$\frac{\partial\theta_s}{\partial t} + \boldsymbol{v}\cdot\nabla\theta_s = 0.$$

Note that during freezing, the ground heaves and $\boldsymbol{v}\cdot\boldsymbol{\nu} \geq 0$, where $\boldsymbol{\nu}$ is an outward normal vector to Ω_t on the surface $\partial\Omega_{as}$. Therefore, the characteristics defined by $\boldsymbol{v}$ point outside the domain Ω_t, and hence θ_s in Ω_s does not depend on θ_s in Ω_a.

3.7 Hydraulically closed system, no suction

In this and the following sections, we analyze the model both quantitatively and qualitatively. Since dependence of the frost heave dynamics on thermal, hydraulic and rheological properties and boundary conditions is rather complicated, we consider several particular cases. In this section, we model frost heave of soils in which migration of water towards

the freezing region is not considered, or $\mathcal{F} = 0$. With this condition, the system (3.15-3.16) becomes

$$\gamma\frac{\partial\theta_w}{\partial t} = \nabla\cdot\Big(\frac{k_f}{g\bar{\rho}_w}\nabla p\Big) + \nabla\cdot\Big(\big(\frac{\bar{\rho}_i}{\bar{\rho}_w} + \gamma\theta_w\big)\frac{\partial \boldsymbol{u}}{\partial t}\Big), \quad \nabla\cdot\hat{\boldsymbol{\sigma}} = \nabla p. \tag{3.21}$$

From the physical point of view, the left hand side of the first equation describes the rate of water volume change during freezing or thawing. For example, during freezing water expands and "some material is being injected" into the soil skeleton, which results in the pressure increase and in consequent ground heaving. The opposite is also true. During thawing, ice melts and consequently "some volume is being removed" from the soil, and hence the pressure decreases. Recall that for hydrologically closed systems, the mass of water in the non-sorted circle is conserved by modeling $\boldsymbol{\nu}\cdot\theta_w(\boldsymbol{v}-\boldsymbol{v}_w)$=0 on the external boundary AB. Hence, the maximum frost heave is equal to the total volume of the "injected" material which is the difference between the final ice volume and the initial liquid water volume. Since during freezing water expands by γ=1$-\bar{\rho}_i/\bar{\rho}_w$, or 9%, it is possible to verify whether the model conserves the total water mass. We check that the maximum frost heave is equal to γV_0, where V_0 is the volume of liquid water that became frozen at the end of simulation. To verify the model quantitatively, we consider the following four cases. In these case studies, we investigate how various soil properties affect redistribution of water resulting in the differential frost heave. Note that in all cases, the initial and boundary conditions ($T^{circle}_{surface} = T^{inter-circle}_{surface}$, and $\boldsymbol{\nu}\cdot\theta_w(\boldsymbol{v}-\boldsymbol{v}_w)$=0 on AB) are the same, but soil properties in regions 1, 2 and 3 can be different.

Case 1: Homogeneous soil. We model one-dimensional freezing of a homogeneous soil which was initially thawed up to D=0.5 meters depth. In this case, the thermal conductivities of frozen and thawed soil is 1.1 and 1.55, respectively; the hydraulic conductivity k_0 for thawed soil is 10^{-8}, the coefficient α determining the hydraulic conductivity for partially frozen soil is 5, Young's modulus is E=2·10^6 and the parameter a determining the unfrozen water content is 10^{-4}. Note that existence of the unfrozen water content leads to non-zero water flux $\mathcal{F}$, which was forcefully set to zero in the numerical program. From the physical point of view, this setting of parameters means that unfrozen water can exist in the soil pores, but the water migration is only due to non-zero gradient in the pressure p. Note that as soon as temperature becomes lower than the freezing point, ice appears, the volume occupied by water enlarges, and hence the pressure increases and exerts force onto the soil skeleton. Figure 3.7 shows a snap shot of temperature, pressure and soil porosity at the 15^{th} day after the beginning of freezing. The middle plot shows a region between

0.05 and 0.5 meters with the positive pressure increase. Note that in the region below 0.5 meters, the temperature increases, and as a result soil partially thaws, causing the decrease in the volume occupied by water, and consequently appearance of the region with negative pressure. The right plot in Figure 3.7 shows the snap shot of soil porosity, which depicts an increase in the initial porosity of 0.35 in the region where water freezes and a corresponding decrease where ice melts.

Since the system is hydraulically closed, the maximum frost heave is equal to

$$n_0(1 - \frac{\bar{\rho}_i}{\bar{\rho}_w})D, \tag{3.22}$$

where n_0 is the soil porosity at the beginning of computations. The maximum frost heave is shown in Figure 3.8, left plot. For the homogeneous soil, the frost heave is uniform and is approximately equal to $1.44 \cdot 10^{-2}$ meters, whereas the frost heave predicted by (3.22) is $0.55 \cdot 0.35 \cdot 0.09 \approx 1.73 \cdot 10^{-2}$ meters. Note that the estimate (3.22) considers that all water freezes in frozen ground. Hence the difference between the predicted and simulated frost heave is due to unfrozen water in frozen soil, and is partially due to numerical errors.

Case 2: Heterogeneous rheological properties. We model soil that has lenticular structure in regions 1 and 2; the value of Young's modulus E in domain 3 is larger that in domains 1 and 2, i.e. in the region 3, E=$2 \cdot 10^7$. Different values of the Young's modulus cause water to flow from more stiff material in region 3 towards the less stiff one in the center. Note that the average value of the frost heave in this case is $1.49 \cdot 10^{-2}$ meters which is approximately the same value as for the homogeneous case, see Figure 3.8.

Case 3: Heterogeneous rheological and thermal properties. We modify the second case by decreasing the thermal conductivity for the organic layer, regions 2, to 1.1. Distinct values of the thermal conductivity do not produce the differential frost heave with respect to the previous run. The average value of the frost heave is approximately $1.44 \cdot 10^{-2}$ meters, which is in agreement with predictions calculated by (3.22).

Case 4: Heterogeneous rheological, thermal and hydraulic properties. We further modified the third case. We decrease the parameter a to 10^{-5} in region 2, to simulate the realistic dependence of the unfrozen water content on temperature of the organic layer. This case shows that the differential frost heave is more pronounced than in all previous runs, and there is more significant redistribution of water during freezing. The redistribution of water is related to the dependence of the hydraulic conductivity on the unfrozen water content. In the mineral soil (regions 1 and 3), the unfrozen water content is parameterized by a=10^{-4}, whereas in the organic soil layer a=10^{-5}. Considering that α=5

in (3.1), we have that for temperature -2 °C the hydraulic conductivity in the inter-circle is more than 100 times less than in the circle. Therefore, during freezing, the migration of water through the organic layer is less than through the mineral soil, and the excessive pressure increases in the region below the organic layer forces water into the circle. This produces larger values of differential frost heave. Nevertheless, the average value of the frost heave for the entire domain is still only $1.49 \cdot 10^{-2}$ meters in this simulation.

Note that on average the maximum frost heave for the entire non-sorted circle during all four simulations is the same ($\pm 0.1 \cdot 10^{-2}$meters), and the computed differential heave is due to water redistribution only. We emphasize that the difference in Young's modulus and unfrozen water content in the circle and inter-circle produce the computed differential frost heave. However, its average value is usually less than observed in the field. This is due to two factors: in these simulations, the external boundary was assumed to be water impermeable; migration caused by cryogenic suction of liquid water to the freezing front was absent in the model so far.

3.8 Hydraulically open and closed system

In nature, we observe that the maximum frost heave is larger at sites where near-surface ground water is abundant (*Walker et al.*, 2004). To explain this phenomena, we show that liquid water migration towards the partially frozen region as well as the unlimited water supply are both essential to simulate the observed frost heave. In total, we model four different cases associated with one of the following combinations of the boundary conditions (P=0, or $\boldsymbol{\nu} \cdot \theta_w(\boldsymbol{v} - \boldsymbol{v}_w)$=0) on the external boundary and the cryogenic suction ($\mathcal{F} \neq 0$, or $\mathcal{F}$=0). Recall that the pressure boundary condition $P = 0$ on the external boundary models flow of water in and out of the non-sorted circle, and hence the system is called hydrologically open. The condition P=0 is approximated by setting $p = 0$ despite of possible artificial deformation of soil near AB that is far from the circle. Similarly, the boundary condition $\boldsymbol{\nu} \cdot \theta_w(\boldsymbol{v} - \boldsymbol{v}_w)$=0 defines the hydrologically closed system.

We recall the last case in the previous section, i.e. **Closed system with no suction** and the heterogeneous rheological, thermal and hydrological soil properties. In this case, the computed differential frost heave is 0.03 meters at the center of the circle and less than 0.01 meters in the inter-circle, see left plot in Figure 3.8. However, if the boundary condition with respect to pressure on the external boundary is changed to model water flow through the boundary, or p=0, we model the hydraulically open system with no suction.

Case 1: Open system with no suction. In Figure 3.9, left plot shows the computed maximum frost heave in this case. Note that the maximum frost heave of the hydraulically open system is smaller than the one of the closed system, since positive pressure in Ω_t pushes water outside through $\partial\Omega_t$ on which p=0 is modeled. These numerical experiments show that presence of a water supply at the boundary of the non-sorted circle cannot alone explain the observed values of frost heave (see Figure 3.2).

Case 2: Closed system with suction. Due to presence of the cryogenic suction $\mathcal{F}\neq 0$, there is an induced flow of liquid water from the thawed region to the partially frozen zone. This causes water to move from the thawed region into the partially frozen one. As a result, the pressure p in the thawed region decreases, see Figure 3.10. In the hydraulically closed system without internal sources of water, the boundaries are not water permeable, and hence no additional water can appear in the non-sorted circle. Consequently, the pressure can decrease indefinitely (see Figure 3.10, the left plot).

Case 3: Open system with suction. In the hydraulically open systems with suction, the cryogenic suction creates similar effects as in the closed systems. Namely, it forces the flow of water and creates a low pressure zone in the thawed region. However, unlike the closed systems, the pressure on the external boundary is fixed p=0 and water can flow through the boundary and supply cryogenic suction forces with water in order to compensate deficiency in water volume and associated with it negative pressure. Therefore, in the hydraulically open systems, the pressure in the thawed region is slightly negative compared to the closed systems, see Figure 3.10, right plot. From the right plot in Figure 3.11, we observe that the positive pressure increase exists in the partially frozen region and it creates the uplifting forces which produce the frost heave.

In this section, we have analyzed the model (3.14-3.17) and conclude that the cryogenic suction forces create water flow and also produces low pressure zones in thawed soil. However, the pressure dynamics and hence the uplifting forces strongly depend on the pressure boundary condition. The model shows that it qualitatively captures and predicts commonly occurring physical behavior of both hydraulically closed and open systems. In the next section, we analyze the model quantitatively, using some observations and measurements from a study site at the Franklin Bluffs, Alaska.

3.9 Modeling frost heave of a non-sorted circle at the Franklin Bluffs site

In this section we apply the general model given by (3.14-3.17) to a non-sorted circle located at the Franklin Bluff site on the Dalton Highway in Alaska. The non-sorted circle is approximately 0.6 meter in radius and is developed in water logged non-acidic tundra. In the inter-circle, the organic layer is 0.2 meter in depth (*Walker et al.*, 2004; *Michaelson et al.*, 2007). An array of sensors measuring temperature and moisture dynamics in time are installed at several depths and at several locations across the non-sorted circle. However, since the measured surface temperature rapidly fluctuates, we compute its 5-day running average shown in the right plot in Figure 3.6 and use it as the upper boundary condition for temperature.

Values of the parameter a that determines the unfrozen liquid water content for mineral and organically enriched soil are found by fitting θ_w expressed from (3.10) to the measured liquid water content at 0.35 meter depth in the circle and 0.15 meter depth in the inter-circle, respectively. Thermal conductivities for the frozen mineral and organically enriched soil are set to be 1.9 and 0.9, respectively. The Young's modulus E for the mineral soil inside and outside the circle is $2 \cdot 10^6$ and $20 \cdot 10^6$, respectively, which are typical values for weakly consolidated and consolidated silt-clay mixture. Since the non-sorted circle is located in water logged area we model it as a hydraulically open system. Initial soil temperature distribution with depth was approximated by measured temperature on 09/12/2002, and the soil porosity was set to be 0.35. On this day the active-layer depths in the center of the non-sorted circle and in the surrounding tundra were 0.8 and 0.6 meter, respectively.

We simulated the soil freezing from 09/12/2002 through 12/18/2002, when the temperature in the non-sorted circle became less than -5 °C. The calculated liquid-water content at 0.35 meter depth in the circle and 0.15 meter depth in the inter-circle are compared to the measured data (see Figure 3.12). The difference in timing of the modeled and observed freeze-up at each shown depth is less than 3 days. We also compare the calculated temperature dynamics to the measured one (see Figure 3.13). In general, the discrepancy between the measured and computed temperature at the depth of 0.35 meters in the circle is less than 1 °C. However, since we utilized the smoothed surface temperature (the right plot in Figure 3.6) to force the model, we cannot resolve some details in the measured soil temperature dynamics as for example around 11/20/2002.

In addition to comparing the measured and computed soil temperatures, we show the calculated pressure p dynamics at the same point, i.e. at the depth of 0.35 meters. Note

that initially when the ground surface temperature was above 0 °C, the pressure p was zero (we assume there is no gravity and the pressure on the lateral boundary is zero). However, as soon as ground freezing begins, the cryogenic suction starts to force water migration from a still unfrozen part of the active layer to the partially frozen one. Therefore, the pressure lowers in the entire thawed part of the active layer; the pressure dynamics have slightly negative values of p at this time which can be observed in the left plot in Figure 3.13. When the freezing front reaches the depth/region at which the pressure and temperature dynamics are shown (0.35 meters), the cryogenic suction starts to force water migration into this still partially frozen region. Soil porosity consecutively increases, see the right plot in Figure 3.13. Due to increase of the water mass, and due to its expansion while freezing the pressure p continues to increase, see the left plot in Figure 3.13. Note that the increased porosity is associated with formation of ice lenses and development of the frost heave (the small decrease in soil porosity is due to numerical regularization of the soil mass conservation principle). Value of the computed frost heave in the center of the non-sorted circle is approximately 0.18 meters whereas in the inter-circle it is 0.045 meters. These computed values are in a good agreement with field observations, see Figure 3.2.

In this section, we demonstrated that it is possible to simulate frost heave dynamics of a single non-sorted circle and obtain results which are in agreement with observations. In the next section, we analyze sensitivity of the model with respect to parametrization of soil properties.

3.10 Sensitivity analysis

From numerical experiments, we note that the frost heave dynamics primarily depend on several soil properties listed in Table 3.3. In this section, we present the results obtained from sensitivity study of the frost heave with respect to values of parameters specifying soil properties. We define the calculated frost heave at the Franklin Bluffs site as a reference point against which we compare a series of numerical experiments. In these experiments we modify thermal and hydraulic properties, and also dimensions of the non-sorted circle. In all plots the frost heave associated with the reference case, i.e. the Franklin Bluffs site, is marked by black line with circle symbols.

In the first series of experiments, we analyze dependence of the frost heave on parametrization of the unfrozen water content on temperature for the mineral soil. We consider several values of the coefficient a associated with high, medium and low unfrozen water

content in the soil. Note that parametrization of unfrozen water content depends on mineralogy, solute concentration, texture and other factors. For example, the high unfrozen water content is associated with fine-grained ground material and is modeled by large values of a, see the right plot in Figure 3.14. For coarse-grained materials, such as sand, the unfrozen water content sharply depends on temperature near 0 °C, see plots associated with small values of a. For each shown parametrization, we simulate freezing of the non-sorted circle and compute the maximum frost heave (see the left plot in Figure 3.14). In these numerical experiments all model parameters except for the parametrization of the unfrozen water content were fixed and equal to the values related to the Franklin Bluffs site.

From the computed results we observe that the largest frost heave occurs, when the soil has the high unfrozen water content. This effect has the following explanation. Hydraulic conductivity k_h of the partially frozen soil increases, if the unfrozen water content θ_w becomes higher, and hence more water migrates through the partially frozen region due to cryogenic suction flow $\mathcal{F}$ (non-linearly dependent on θ_w) and forms ice lenses. The above-mentioned dependence of the frost heave on unfrozen water content is commonly observed in nature, i.e. the sand and gravel are not frost-heave susceptible soils, whereas silt is. Note that clays which have even higher unfrozen water content but have low hydraulic conductivity and typically are not capable of developing significant frost heave.

In the second series of experiments, we investigate dependence of the maximum frost heave on parametrization of hydraulic conductivity k_h for the partially frozen ground. One of the typically unknown parameters is the quantity α that determines dependence of the coefficient k_h on the unfrozen liquid water content in (3.1). Large values of α correspond to small values of k_h, and otherwise. Figure 3.15 shows the computed maximum frost heave for several values of α. As in the previous experiment, we observe that the frost heave is higher when the value of k_h is larger which corresponds to smaller values of α. As in the first series of experiments, we observed that the frost heave sharply depends on the soil hydraulic properties. We note that the frost heave does not significantly depend on values of the thermal conductivity of mineral soil, as it was shown in Section 3.7 in the third case.

In our field experiments, we observe that at several sites circles have a thin horizon of the organic soil. From the physical point of view, this layer represents an additional thermal resistance and changes mean temperatures in the soil. Therefore, in the third series of experiment, we analyze dependence of the maximum frost heave on presence of organically enriched soil in the non-sorted circles. We consider several configurations of

organic layers varying in their thicknesses. We additionally place on top of the non-sorted circle an organic layer which uniformly covers the circle and inter-circle. The soil thermal, hydraulic and rheological properties of this additional layer are identical to the properties of the original organically enriched soil in the inter-circle for the Franklin Bluffs site. Note that an increase in insulation layer causes a decrease in the active-layer thickness. From our field studies, we observed that each additional 0.02-0.03 meters of the organic material results in 0.04-0.05 meter decrease of the active layer. In the left plot in Figure 3.16, we show the maximum frost heave developed for various thicknesses of the additional organic layer. We emphasize that observed results are in agreement with observations at non-sorted circles along the Dalton highway in Alaska. For example, the scarcely vegetated circles at the Franklin Bluff area heave by 0.15-0.20 meters, whereas moderately vegetated circles at the Happy Valley site develop only 0.07-0.10 meters of heave during winter. Also, field experiments (*Kade et al.*, 2005, 2006; *Kade and Walker*, 2007) at Sagwon Bluffs involved both the removal and addition of vegetation on non-sorted circles. The removal of vegetation at this location resulted in a 1.4 °C increase in mean summer soil temperature compared to control, and a 6% increase in the depth of the thaw layer, and a 26% increase in frost heave. The addition of a 0.1 meter thick moss layer results in the opposite effect, a 2.8 °C decrease in the mean summer soil surface temperature, a 15% reduction in the thaw layer, and a 52% decrease in heave. Despite the fact that the numerical model is focused on non-sorted circles at the Franklin Bluffs site and the field experiments were conducted at the Sagwon Bluffs site (these sites are only 30 kilometers apart and have similar soil and climate conditions), results from these studies show qualitative agreement, and similar quantitative behavior of frost heave reduction.

In the fourth series of experiments, we investigate sensitivity of frost heave on the radius of the non-sorted circles. We calculate the frost heave for circles which have 0.1, 0.2, 0.3,...,1.0 meter radius. Our calculations support observations which reveal that small scale non-sorted circles heave less comparing to the large diameter ones. The maximum computed frost heave is for circles with the radius of 0.6 meters, see the right plot in Figure 3.16. For circles with the radius larger than 0.6 meters, the maximum frost heave slightly decreases since liquid water has to migrate to the center of the non-sorted circle longer from the lateral boundary where water is abundant. Smaller values of the frost heave, that are computed in the center of the non-sorted circle with a large radius, can promote development of live vegetation.

3.11 Conclusions

We present a numerical thermo-mechanical model of differential frost heave with special emphasis on simulating biocomplexity of non-sorted circle ecosystems. Unlike other models that study 1-D ice lens formation, we consider the 2-D effects of soil freezing. Heterogeneity in soil properties and surface conditions result in a differential frost penetration and 2-D temperature fields. Therefore, the cryogenic suction results in horizontal water redistribution between inter-circle and circle areas. Despite the simplicity (no diffusion of salts, simplified rheology) the model captures and successfully simulates temperature and water dynamics in soil. Also, the model satisfactorily simulates the ground surface motion in relation to frost heave and explains the dependence of the amount of frost heave on specific environmental properties of this ecosystem.

The model was tested using observational data obtained from several sites within the Permafrost \ Ecological North American Arctic Transect. We obtained a good comparison between simulated and observed dynamics of physical processes in the non-sorted circle at the Franklin Bluffs. The model also qualitatively represents "non-heaving" non-sorted circles at the Howe Island site.

The simulated frost heave is sensitive to hydrological soil properties, and to change in the vegetative insulation layer within the circle and inter-circle areas. The results of our sensitivity analysis with respect to addition/removal of vegetation layer to/from the surface of a circle are well correlated with field observations, where a layer of organic material was either added or removed to the non-sorted circle. The performed sensitivity analysis provides deeper understanding of functioning of the non-sorted circle as an ecosystem.

Based on results from the sensitivity analysis, we conclude that the most active development of differential frost heave takes place for non-sorted circles within waterlogged area with strong upper-soil-layer heterogeneity caused by living vegetation. The most important driver of the non-sorted circle ecosystem is the presence of vegetation that, over a significant time, changes the soil mineralogy and thermal and hydrological soil properties, thus changing the amount of differential frost heave and reducing or enhancing all bio-geophysical processes responsible for the formation and evolution of the non-sorted circles.

Testing of our numerical model provides an assurance that this model can be used to study the impact of changes in major natural geophysical and biological drivers on specific properties and dynamics of the non-sorted circles in different ecological systems. The presented model provides a powerful tool to investigate possible future changes in

this ecosystem in relation to observed and projected climatic and biological changes in the Arctic.

3.12 Acknowledgments

We would like to thank Jacob Stroh, Michael Ladouceur, Juha Hartikainen, and Lynn Bennethum for their advice, critique and reassurances along the way. We are thankful to reviewers who helped to clarify certain parts of this manuscript. This research was funded by ARCSS Program and by the Polar Earth Science Program, Office of Polar Programs, National Science Foundation (OPP-0120736, ARC-0632400, ARC-0520578, ARC-0612533, IARC-NSF CA: Project 3.1 Permafrost Research), by NASA Water and Energy Cycle grant, and by the State of Alaska.

Bibliography

Astrakhantcev, G. (1978), Method of fictitious domains for a second-order elliptic equation with natural boundary conditions, *USSR Comp. Math. Math.*, *18*, 114–121.

Bennethum, L., and T. Weinstein (2004), Three pressures in porous media, *Transport Porous Med.*, *54*(1), 1–34.

Beskow, G. (1935), *Soil Freezing and Frost Heaving with Special Application to Roads and Railroads, C, no. 375, Year Book no. 3*, 145 pp., The Swedish Geological Society, Technological Institute, Northwestern University, translated by J.O. Österberg.

Blanchard, D., and M. Fremond (1982), Cryogenic suction in soils, in *Proceedings of the 3rd International Symposium on Ground Freezing*, vol. 1, pp. 233–238, Hanover, New Hampshire.

Buzbee, B., F. Dorr, J. George, and G. Golub (1971), The direct solution of the discrete poisson equation on irregular regions, *SIAM J. Numer. Anal.*, *8*, 722–736.

Coussy, O. (2005), Poromechanics of freezing materials, *J. Mech. Phys. Solids*, *53*, 1689–1718.

Dash, J., H. Fu, and J. Wettlaufer (1995), The premelting of ice and its environmental consequences, *Rep. Prog. Phys.*, *58*, 115–167.

de Vries, D. (1963), *W.R. van Wijk (editor) Physics of the Plant Environment*, chap. Thermal properties of soils, pp. 210–235, Wiley, New York.

Everett, D. (1961), The thermodynamics of frost damage to porous solid, *T. Faraday Soc.*, *57*, 1541–1551.

Fowler, A. (1989), Secondary frost heave in freezing soils, *SIAM J. Appl. Math.*, *49*, 991–1008.

Frémond, M., and M. Mikkola (1991), Thermomechanical modeling of freezing soil, in *Proceedings of the 6th International Symposium on Ground Freezing*, edited by W. C. Yu X., pp. 17–24, Balkema, Rotterdam.

Glowinski, R., T.-W. Pan, and J. Periaux (1994), Fictitious domain method for dirichlet problems and applications, *Comput. Method. Appl. M.*, *111*, 283–303.

Graham, J., and V. Au (1985), Effects of freeze-thaw and softening on a natural clay at low stresses, *Can. Geotech. J.*, *22*(1), 69–78.

Hartikainen, J., and M. Mikkola (1997), General thermomechanical model of freezing soil with numerical applications, in *Ground Freezing*, edited by K. S., pp. 101–105, Balkema, Rotterdam.

Hobbs, P. (1974), *Ice Physics*, 856 pp., Claredon Press, Oxford.

Huyghe, J., R. V. Loon, and F. Baaijens (2004), Fluid-solid mixtures and electrochemomechanics: the simplicity of lagrangian mixture theory, *Comput. Appl. Math.*, *23*, 235–258.

Jussila, P. (2006), Thermodynamics of porous media - I: thermohydraulic model for compacted bentonite, *Transport Porous Med.*, *62*, 81–107.

Kade, A., and D. Walker (2007), Experimental alternation of vegetation on non-sorted circles: effects on cryogenic activity and implications for climate change in the arctic, *Arct. Antarct. Alp. Res.*, in press.

Kade, A., D. Walker, and M. Raynolds (2005), Plant communities and soils in cryoturbated tundra along a bioclimate gradient in the low arctic, alaska, *Phytocoenologia*, *35*, 761–820.

Kade, A., V. Romanovsky, and D. Walker (2006), The n-factor of nonsorted circles along a climate gradient in arctic alaska, *Permafrost Periglac.*, *17*, 279–289.

Konrad, J., and C. Duquennoi (1993), A model for water transport and ice lensing in freezing soils, *Water Resour. Res.*, *29*(9), 3109–3124.

Konrad, J., and N. Morgenstern (1981), The segregation potential of a frozen soil, *Can. Geotech. J.*, *18*, 482–491.

Kuznetsov, Y. (2000), The fictitious domain method, in *Proceedings of the Annual International Meeting on Domain Decomposition Methods*, edited by M. Garbey, Lyon.

Landau, L., and E. Lifshitz (1984), *Statistical Physics*, vol. 5, 544 pp., Butterworth-Heinemann.

Li, N., F. Chen, B. Su, and G. Cheng (2002), Theoretical frame of the saturated freezing soil, *Cold Reg. Sci. Technol.*, *35*, 73–80.

Litvan, G. (1972), Phase transitions of absorbates iv. mechanism of frost hardened cement paste, *J. Am. Ceram. Soc.*, *55*(1), 38–42.

Marchuk, G., Y. Kuznetsov, and A. Matsokin (1986), Fictitious domain and domain decomposition methods, *Sov. J. Numer. Anal. Mat.*, *1*, 1–82.

Michaelson, G., C. Ping, H. Epstein, J. Kimble, V. Romanovsky, C. Tarnocai, and D. Walker (2007), Soil properties and patterned ground across the north american arctic transect: Trends in physiochemical properties, *J. Geophys. Res. - Biogeosciences*, submitted.

Michalowskin, R., and M. Zhu (2006), Frost heave modeling using porosity rate function, *Int. J. Numer. Anal. Met.*, *30*, 703–722.

Mikkola, M., and J. Hartikainen (2001), Mathematical model of soil freezing and its numerical application, *Int. J. Numer. Meth. Eng.*, *52*, 543–557.

O'Neill, K., and R. Miller (1985), Exploration of a rigid ice model of frost heave, *Water Resour. Res.*, *21*, 281–296.

Penner, E. (1959), The mechanism of frost heave in soils, *Highway Research Board Bulletin*, *225*, 1–22.

Peterson, R., and W. Krantz (2003), A mechanism for differential frost heave and its implications for patterned ground formation, *J. Glaciol.*, *49*(164), 69–80.

Powers, T., and R. Helmuth (1953), Theory of volume changes in hardened portland cement paste during freezing, in *Proceedings of the Highway Research Board*, vol. 32, pp. 285–297, Washington, DC.

Qi, J., P. Vermeer, and G. Cheng (2006), A review of the influence of freeze-thaw cycles on soil geotechnical properties, *Permafrost Periglac.*, *17*, 245–252.

Ramiere, I., P. Angot, and M. Belliard (2005), Fictitious domain methods to solve convection-diffusion problems with general boundary conditions, in *17th Computational Fluid Dynamics Conference - AIAA*, pp. AIAA 2005–4709, Toronto.

Rempel, A., J. Wettlaufer, and M. Worster (2004), Premelting dynamics in a continuum model of frost heave, *J. Fluid Mech.*, *498*, 227–244.

Samarskii, A., and P. Vabishchevich (1996), *Computational Heat Transfer, Mathematical Modeling*, vol. 1, 418 pp., Wiley.

Saulev, V. (1963), On solution of some boundary value problems on high performance computers by fictitious domain method, *Siberian Math. J.*, *4*(4), 912–925, in Russian.

Sergueev, D., G. Tipenko, V. Romanovsky, and N. Romanovsky (2003), Mountain permafrost thickness evolution under influence of long-term climate fluctuations (results of numerical simulation), in *Proceedings of the Eighth International Conference On Permafrost*, vol. 2, edited by M. Phillips, S. Springman, and L. Arenson, pp. 1017–1021.

Taber, S. (1918), Ice forming in clays will lift surface weights, *Engineering News-Record*, *80*(6), 262–263.

Taber, S. (1929), Frost heaving, *J. Geol.*, *37*, 428–461.

Taber, S. (1930), The mechanics of frost heaving, *J. Geol.*, *38*(4), 303–317.

Tsytovich, N. (1975), *Mechanics of Frozen Ground*, 426 pp., Scripta/McGraw-Hill, New York.

van. Everdingen R. (2005), *Multi-Language Glossary of Permafrost and Related Ground-Ice Terms*, National Snow and Ice Data Center/World Data Center for Glaciology, Boulder.

Viklander, P., and D. Eigenbrod (2000), Stone movements and permeability changes in till caused by freezing and thawing, *Cold Reg. Sci. Technol.*, *31*(2), 151–162.

Walker, D. (2007), Biocomplexity of small patterned ground features along the north american arctic transect, *J. Geophys. Res. - Biogeosciences*, in review.

Walker, D., et al. (2004), Frost-boil ecosystems: complex interactions between landforms, soils, vegetation and climate, *Permafrost Periglac.*, *15*, 171–188.

Watanabe, K., and M. Mizoguchi (2000), Ice configuration near a growing ice lens in a freezing porous medium consisting of micro glass particles, *J. Cryst. Growth*, *213*, 135–140.

Wettlaufer, J., and M. Worster (1995), Dynamics of premelted films: frost heave in a capillary, *Physics Review E*, *51*, 4679–4689.

Williams, P. (1982), *The Surface of the Earth: An Introduction to Geotechnical Science*, 242 pp., Longman, London.

Williams, P., and M. Smith (1989), *The Frozen Earth*, 306 pp., Cambridge University Press, Cambridge.

Zienkiewicz, O., and R. Taylor (1989), *The Finite Element Method*, vol. 1, 648 pp., McGraw-Hill, London.

Table 3.1: Description and range of soil properties values for non-sorted circles along the Dalton Highway in Alaska

Domain	Soil	Ice lenses	Unfrozen water	λ_s	$E \cdot 10^6$	a
1	Mineral	Many	High content	0.9...1.9	1...5	$1 \cdot 10^{-4}$
2	Organic	Many	Low content	0.3...0.8	1...5	$1 \cdot 10^{-5}$
3	Mineral	Few	High content	0.9...1.9	10...50	$1 \cdot 10^{-4}$

Table 3.2: Boundary conditions

Variable	AB	$\partial\Omega_{as}$	OA	OO'
T	$\boldsymbol{\nu} \cdot (\lambda \nabla T) = 0$	$T = T_{surface}$	T=T_{bottom}	$\boldsymbol{\nu} \cdot (\lambda \nabla T) = 0$
p	$\boldsymbol{\nu} \cdot \theta_w(\boldsymbol{v} - \boldsymbol{v}_w)$=0, or $P = 0$	$P = 0$	$\boldsymbol{\nu} \cdot \theta_w(\boldsymbol{v} - \boldsymbol{v}_w)$=0	$\boldsymbol{\nu} \cdot \theta_w(\boldsymbol{v} - \boldsymbol{v}_w)$=0
$\boldsymbol{u}$	u_r=0, $(\boldsymbol{\sigma} \cdot \boldsymbol{\nu})_z$=0	$\boldsymbol{\sigma} \cdot \nu$=0	$\boldsymbol{u}$=0	u_r=0, $(\boldsymbol{\sigma} \cdot \boldsymbol{\nu})_z$=0

Table 3.3: Key parameters in the model on which the frost heave depends

Type	Parameters	Description
Hydrological	a	Parametrization of the unfrozen water content
	k_0, α	Parametrization of the hydraulic conductivity
Thermal	λ_s, C_s	Thermal conductivity and heat capacity
Rheological	E	Young's modulus

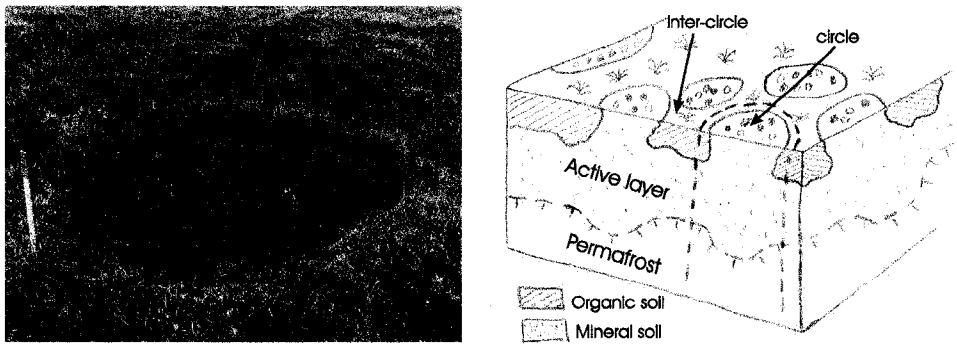

Figure 3.1: A photography (left) and schematic description (right) of non-sorted circle.

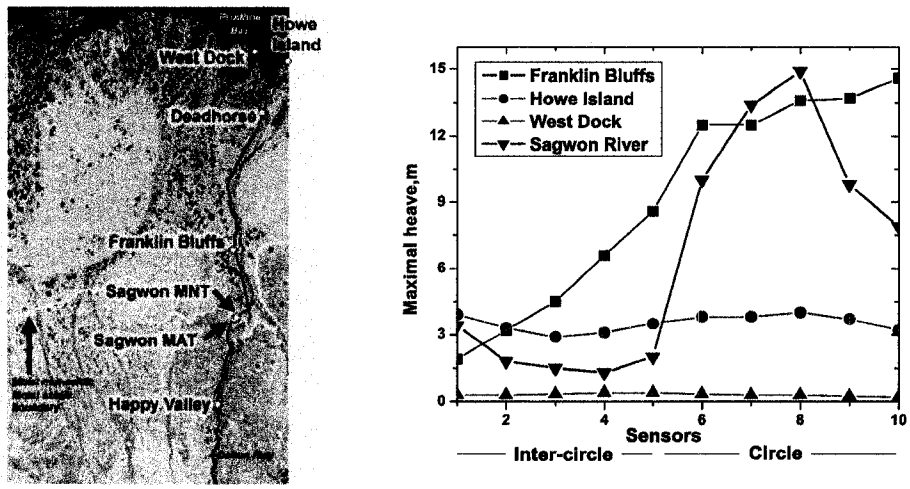

Figure 3.2: Locations of sites (left) at which several non-sorted circles were monitored. Frost heave measurements (right) along the cross-section of a non-sorted circle in April 2002.

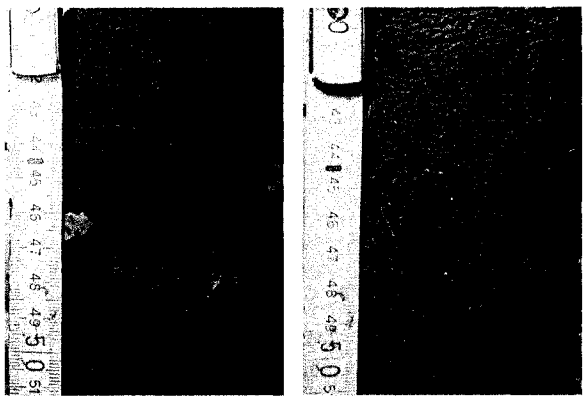

Figure 3.3: Core samples obtained from the inter-circle area (left photo) and circle (right photo) at the Franklin Bluffs site during winter. On the right photograph, a sequence of horizontally oriented ice lenses can be observed. The vertical scale is in centimeters.

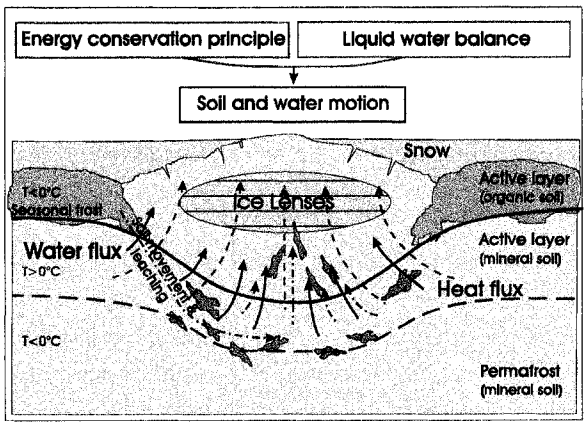

Figure 3.4: A diagram of fundamental physical processes taking place in a freezing non-sorted circle during the fall. Directions of the water flow, heat flux, and soil displacement are marked by blue solid, red dashed and black dot-dashed lines, respectively. Location of the 0 °C isotherm is marked by the solid blue line, whereas location of the permafrost table by the dashed black line.

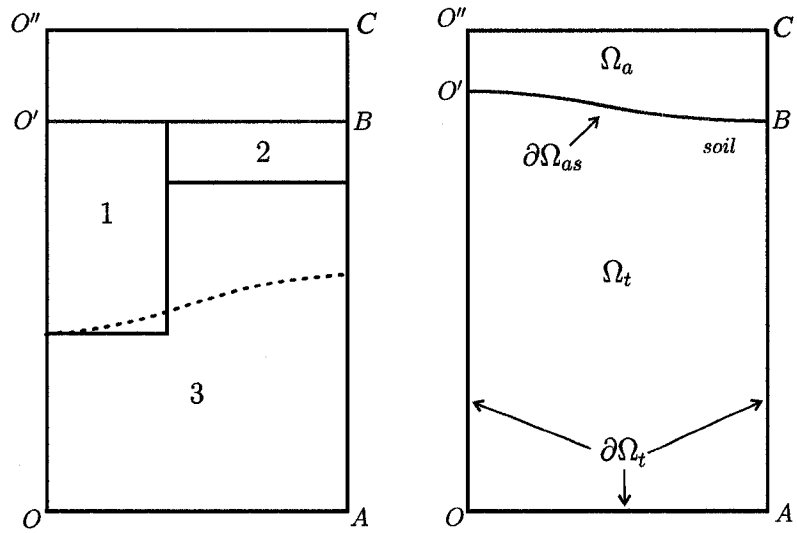

Figure 3.5: The schematic cross section (left) of the non-sorted circle and its computational domain (right). Segment OO'' is the axis of rotation, AB is the external boundary, and the dotted line on the left shows the upper permafrost boundary. Domains 1 and 3 - mineral soil, Domain 2 - organic soil. Regions Ω_a and Ω_t represent air and soil, respectively. The segment $\partial\Omega_{as}$ is the ground surface. The boundary $\partial\Omega_t$ is the boundary of the computational domain associated with the non-sorted circle.

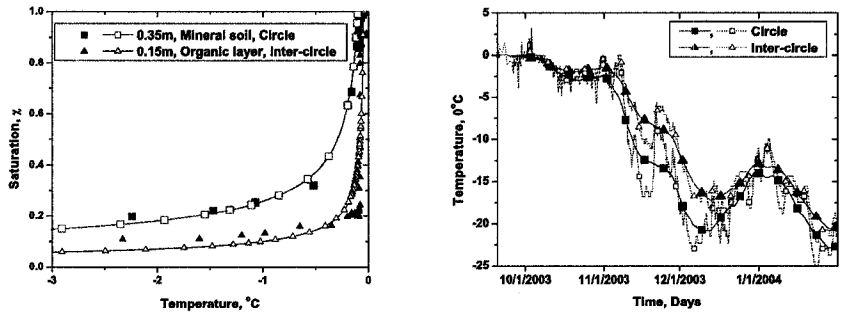

Figure 3.6: Calibration of the unfrozen water content curve by fitting (hollow symbols) $\chi(T)$ expressed from (3.10) to the measured data (filled symbols), left plot. In the right plot, temperature dynamics $T_{surface}^{circle}$, $T_{surface}^{inter-circle}$ on the surface of the non-sorted circle at the center of the circle and in the inter-circle, respectively. The time series $T_{surface}^{circle}$ and $T_{surface}^{inter-circle}$ are records (the five day averaged, filled symbols, solid line) of ground surface temperatures measured (dotted line, hollow symbols) at 0.01 meter depth.

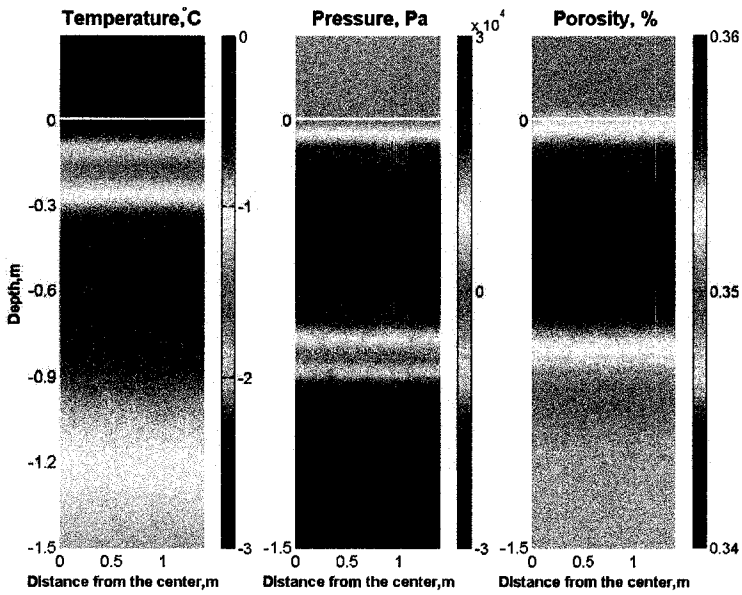

Figure 3.7: The temperature, pressure and soil porosity fields at the 15^{th} day after freezing begins for the hydrologically closed system. Volumetric water expansion during freezing creates a build up of pressure in the thawed region.

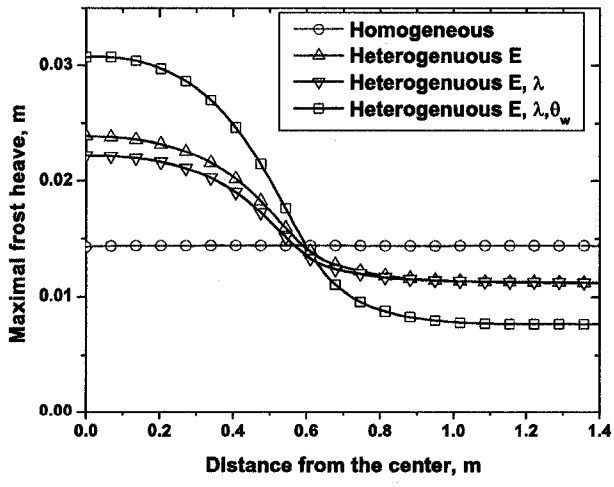

Figure 3.8: The maximum frost heave for different combination of rheological, thermal and hydraulic soil properties.

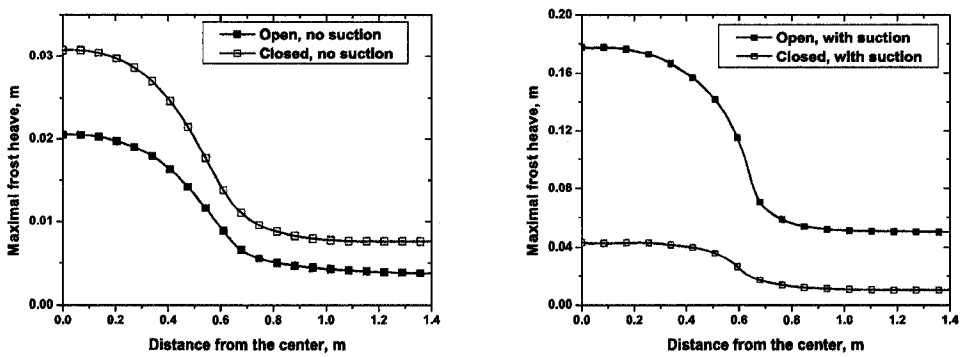

Figure 3.9: Maximum frost heave for hydrologically close (left) and open (right) systems.

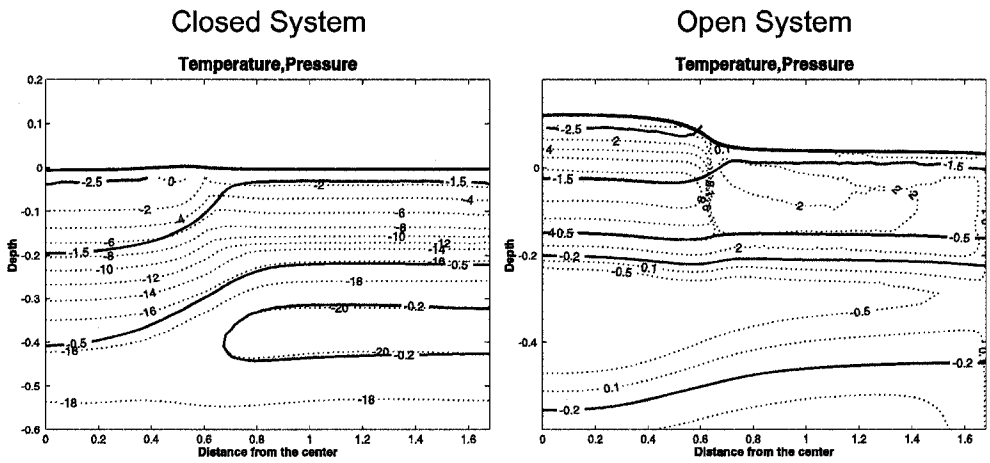

Figure 3.10: Contours of the temperature in °C (solid lines) and pressure in 10^5 Pa (dotted lines) at the 30th days after freezing, for hydraulically closed (left) and open (right) systems.

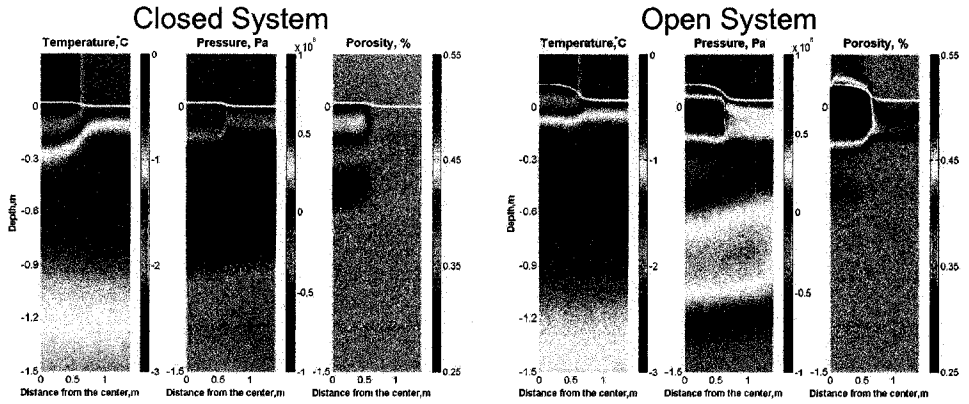

Figure 3.11: The temperature, pressure and soil porosity fields at the 15th day after freezing begins for the hydrologically closed (left) and open (right) system. Since the water migration through the external boundary is not permitted for closed system, the pressure decreases and becomes extremely low, whereas for open systems the migration of water compensates it and hence the uplift is created.

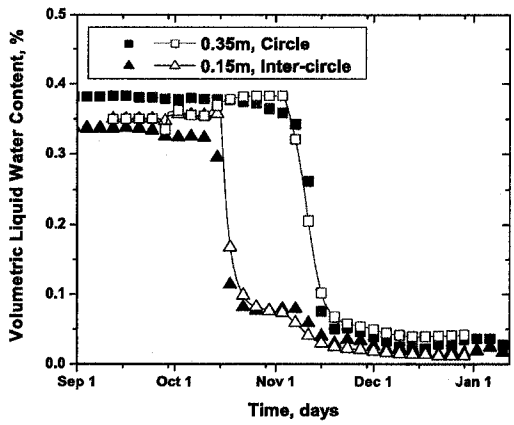

Figure 3.12: Dynamics of the measured (filled symbols) and computed (hollow symbols) liquid water content θ_w at the Franklin Bluffs site at some depths in the center of the circle and in the inter-circle.

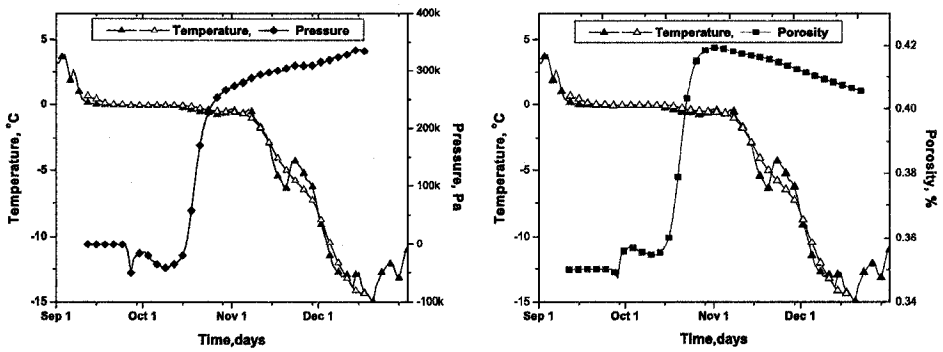

Figure 3.13: The dynamics of the measured (filled symbols) and calculated (hollow symbols) temperature at 0.35 meter depth in the circle, respectively.

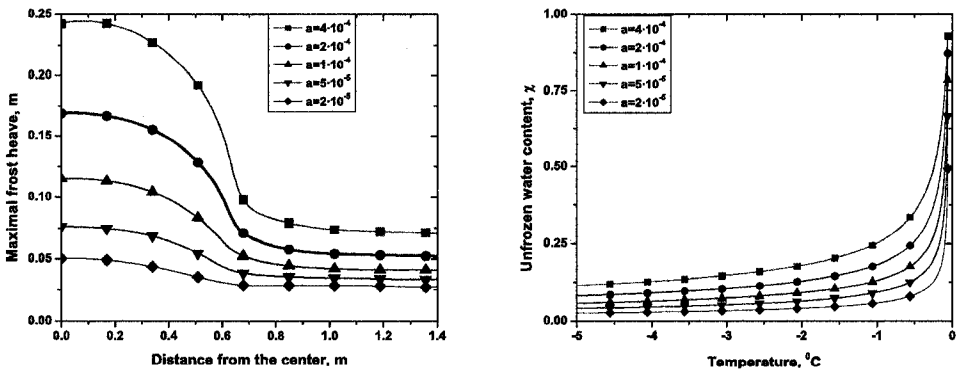

Figure 3.14: Sensitivity of the frost heave on parametrization of the unfrozen water content.

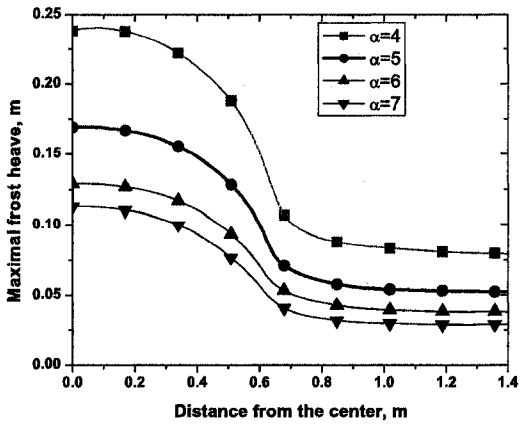

Figure 3.15: Sensitivity of the frost heave on parametrization of the hydraulic conductivity.

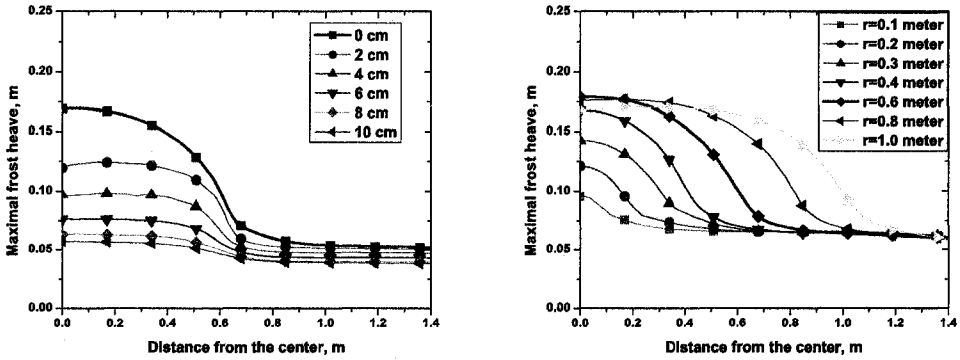

Figure 3.16: Sensitivity of the maximum frost heave on addition of organically enriched soil (left) and on the radius (right) of the non-sorted circle.

Chapter 4

Improved modeling of permafrost dynamics in a GCM land-surface scheme[4]

4.1 Abstract

Global climate models (GCM) are frequently used to understand and predict future climate change, but most GCMs do not attempt to represent permafrost dynamics and its potentially critical feedbacks on climate. In this chapter we evaluate the Community Land Model (CLM3), which is a land-surface scheme, against observations and identify potential modifications to this model that improve fidelity of permafrost and soil temperature simulations. These modifications include increasing the total soil depth by adding new layers, incorporating a surface organic layer, and modifying the numerical scheme to include unfrozen water dynamics and more realistic phase change representation.

4.2 Introduction

Recently, the Arctic Climate Impact Assessment report (*ACIA*, 2004) concluded that climate change is likely to significantly transform the present natural environments, particularly across extensive areas in the Arctic and sub-Arctic. Among the highlighted potential transformations are changes in soil temperature regime and associated changes in permafrost. Soil warming can potentially drive an increase in the active layer thickness and degradation of permafrost as well as have broader impacts on soil hydrology, northern ecosystems and infrastructure. At present, permafrost is widely distributed with permafrost-affected areas covering about 25% of the land surface in the Northern Hemisphere (*Brown et al.*, 1997).

At present, there are two common approaches to simulate soil temperature and permafrost dynamics on regional and global scales. The first approach is well-developed and can be classified as a post-processing approach. In this approach, climatic variables computed by global climate models are used as input parameters for stand-alone permafrost models (*Anisimov and Nelson*, 1997; *Sazonova et al.*, 2004). Given the correct parameters, these stand-alone models are accurate and can be used for a quantitative analysis. The second approach involves simulation and prediction of permafrost dynamics within a coupled global climate model (*Stendel and Christensen*, 2002; *Lawrence and Slater*, 2005; *Mölders*

[4] D.J. Nicolsky, V.E. Romanovsky, V.A. Alexeev, and D.M. Lawrence, 2007, "Improved modeling of permafrost dynamics in a GCM land-surface scheme", published in Geophysical Research Letters, 34(8): L08501

and Romanovsky, 2006). This approach permits the integration of potentially important interrelationships between permafrost, hydrology, and climate. However, in order for these benefits to be fully realized, improvements to ground temperature dynamics in present generation GCMs are required. In this paper, we demonstrate that correcting a few common simplifications in GCM land surface schemes can significantly improve the simulation of permafrost dynamics. Specifically, we evaluate and suggest improvements to the CLM3 (*Oleson et al.*, 2004) which is the land-surface scheme in the Community Climate System Model (*Collins et al.*, 2006).

4.3 Sensitivity analysis

Throughout this paper, we analyze the soil temperature dynamics computed by CLM3 in its offline mode and compare it with in-situ data collected in Alaska. In all our numerical experiments, we use atmospheric forcing data that is based on NCEP/NCAR reanalysis data. To simplify the analysis and remove the influence of trends, we compute 100 years of temperature dynamics by repeatedly forcing the model with the 1998 forcing data that is provided by NCAR with the CLM3 code. The soil temperature initial conditions are specified according to the present day measured temperatures at locations where the temperature dynamics are computed. In the following subsections, we describe a number of modifications to CLM3 that together significantly improve simulated permafrost dynamics.

4.3.1 Soil layer depth

The CLM3 simulates the ground temperature by a 10-layer soil model with the total simulated thickness of the soil column equal to 3.43 meters. Under natural conditions at the Alaska Coastal Plain, the so-called heat waves related to multi-decadal surface temperature variability decay at a depth of approximately 100 meters. The geothermal heat flux can be used as the lower boundary condition at this depth (*Lachenbruch et al.*, 1982). This suggests that in order to capture multi-decadal development of the temperature regime and permafrost thickness, a deeper soil column is required and that the specification of the bottom boundary condition needs to be reconsidered. For calculation of temperature dynamics in the upper 20−30 meters of soil and for time intervals of around a century, the geothermal heat flux at the depth of 100 meters can be ignored and the heat flux at the bottom of the lowest soil layer can be assumed to be zero. This assumption can be particularly valid under the present warming conditions due to the substantially decreased

temperature gradient in the upper 30−100 meters of the ground material (*Osterkamp and Romanovsky*, 1999; *Romanovsky and Osterkamp*, 2001; *Osterkamp*, 2005).

We illustrate the importance of an increased total thickness of the soil with an example simulation of the seasonal temperature dynamics at Deadhorse, Alaska. Typical active layer depths at Deadhorse under present day climate conditions are around 0.6 meters and do not exceed 1 meter. The CLM3 simulates an active layer that is too deep (see the simulated ice content dynamics in Figure 4.1,left). The impact of increasing the model depth to 80m is seen in Figure 4.1, right. To get to 80m, we added 10 layers to the bottom of the existing vertical grid in the original CLM3 model with exponentially increasing thickness of each layer (hereafter CLM3/80). Because of the very low hydraulic permeability of the added permafrost layers, this modification does not lead to significant changes in soil moisture conditions. As a result of this modification, the active layer depth is simulated more realistically, although the simulated active layer is still deeper than that observed due primarily, as we show in the next subsection, to the lack of a surface organic soil layer. A systematic sensitivity analysis of the temperature dynamics with respect to the total soil thickness is beyond the scope of this paper, but it will be presented in a separate work (*Alexeev et al.*, 2007).

4.3.2 Thermal conductivity

A surface layer of organic material of 0.2−0.3 meter depth is prevalent in many permafrost regions and plays a dominant role in heat balance and soil temperature regime because of its distinct thermal properties (*Walker et al.*, 2002). The CLM3 does not include the effect of soil organic material on the thermal and hydraulic properties of the soil. The thermal conductivity and heat capacity of each soil layer are directly parameterized by its sand and clay content, and the entire soil column is treated as a mineral soil only. Consequently, thermal conductivity values simulated in the CLM3 are typically significantly larger than measured ones for both soil types (mineral and organic) (*Romanovsky and Osterkamp*, 1997; *Mölders and Romanovsky*, 2006).

We illustrate the importance of including an organic layer by analyzing the soil temperature dynamics computed at Nome (grid cell $165.6°\pm0.3°W$, $65.2°\pm0.2°N$) on the Seward Peninsula in Alaska. Permafrost at Seward Peninsula can be characterized as discontinuous and its temperature is near $0°C$. Therefore, in order to estimate the current permafrost distribution in Seward Peninsula and its evolution it is necessary to prescribe thermal

properties accurately. In our numerical experiments, we compute long-term temperature dynamics over 100 years. Recall that in all our simulations the atmosphere forcing is given by repeating 100 times the 1988 NCEP/NCAR reanalysis forcing data. Initial soil temperatures are prescribed according to observed present-day conditions. Results from two CLM3/80 simulations are shown in Figure 4.2. In the first simulation, the organic layer is not included and original CLM3 thermal properties, as listed in Table 4.1, are used. In this simulation, initially frozen soil becomes thawed after 100 years, i.e. there is no ice at 3 meter depth and the soil temperature stays above $0°C$. In the second simulation, we represent the surface organic layer by reducing thermal conductivities throughout the upper 3 meters (see Table 4.1). In this simulation, the temperature at 3 meter depth stays below $0°C$ and permafrost exists, as it should for this tundra site with a well-developed organic soil horizon. Therefore, these simulations indicate that incorporation of an organic layer in CLM3 is likely crucial to obtain a realistic permafrost distribution, especially in areas of discontinuous permafrost where soil temperature is close to $0°C$.

We compare measured soil temperature dynamics at the West Dock site ($148°33.1'W$, $70°22.5'N$, a cold permafrost site near Deadhorse, Alaska) with results simulated by CLM3 (grid cell $148.4°\pm0.06°W, 70.0°\pm0.06°N$) and its modifications: CLM3/80 and CLM3/80 + "organic layer". We note that for 1998 year the NCEP surface air temperature (SAT) at this specific grid cell reflects reasonably well the measured SAT at the West Dock site except for the shoulder seasons. Since the West Dock site is located near a coastal line, the measured SAT is influenced by the Arctic Ocean, whereas in the CLM, the climate at the West Dock is modeled as more continental. For instance, in June and July 1998 the measured SAT at 2m height is colder by $7\pm2°C$ than the SAT computed by CLM at the same height. With this discrepancy in mind, the measured and simulated soil temperature dynamics at 1m depth are shown in Figure 4.3. Once again, the inclusion of an organic layer and deeper soil layers significantly improve soil temperature simulations, particularly during the summer and fall. In winter, the simulated soil temperatures are much colder than the measured ones. This winter colder bias may be partially explained by a thinner snow layer in the CLM3 ($\approx$0.11m) than the one observed at this site in 1998 ($\approx$0.25m). Another potential reason for the cold winter soil temperature bias in the CLM3 is the colder NCEP SAT (by $10\pm5°C$) compared to the measured SAT in early winter.

The results in this subsection indicate that inclusion of an organic layer has a significant bearing on the soil temperature simulations and should be included in future versions of the

model. (*Lawrence and Slater*, 2007) describe a method of incorporating globally organic soil and its impact on soil thermal and hydraulic properties through the use of global soil carbon data provided by the Global Soil Data Task (*GSDT*, 2000).

4.3.3 Numerical scheme of the soil heat transfer

The CLM3 simulates typical seasonal soil temperature T dynamics at different depths by the following procedure (*Oleson et al.*, 2004). First, neglecting the phase change, the heat equation

$$C\frac{\partial T}{\partial t} = \frac{\partial}{\partial z}\lambda\frac{\partial T}{\partial z}, \tag{4.1}$$

where C is the heat capacity and λ is the thermal conductivity is solved numerically to calculate the soil temperatures. At the second step, an energy conservation principle is used to adjust the temperature, water, and ice content for each soil layer independently (not taking into account temperature of the adjusted soil layers). One of the consequences of this two-step procedure is that the region where the phase change occurs can be artificially stretched, leading to inaccuracies in the simulation of active layer depth.

In order to calculate temperature dynamics near $0°C$ more accurately, and hence to compute the active layer dynamics more precisely, it is preferable to solve heat diffusion and phase change *simultaneously*. We propose to employ the enthalpy formulation of the heat equation (*Samarskii and Vabishchevich*, 1996).

First, evaluate the apparent heat capacity

$$C_{app} = C + L\frac{d\theta_w}{dT},$$

where $\theta_w = \theta_w(T)$ is a volumetric liquid water content at the temperature T. One of the common parameterizations of the liquid water content θ_w is proposed by (*Anderson et al.*, 1978):

$$\theta_w = n\psi, \quad \psi = \begin{cases} 1, & T \geq T_* \\ (\frac{T}{T_*})^b, & T < T_* \end{cases}, \tag{4.2}$$

where the temperature T is in $°C$, the quantity n is the volumetric liquid water content at the moment when freezing starts; $T_*<0°C$ is referred to as the temperature of the freezing point depression, and $b<0$ is a constant.

After evaluating the apparent heat capacity C_{app}, the next step is to use C_{app} instead of C in the original code that solves (4.1). Since the apparent heat capacity C_{app} is a

rapidly changing function of the temperature near $0°C$, iteration of the soil temperature T calculation is required.

Note that this two-step procedure allows explicit evaluation of the unfrozen water content θ_w at any temperature. In many in-situ measurements, it is observed that some liquid water exists even at soil temperatures significantly below $0°C$ (*Romanovsky and Osterkamp*, 2000). In the CLM3, liquid water can co-exist with ice only at $0°C$. Physically, unfrozen water introduces a spatially distributed latent heat and changes thermal properties which retard the thermal response of an active layer or permafrost. Unfrozen water in the freezing and frozen active layer and near-surface permafrost protects the ground from rapid cooling and creates a strong thermal gradient at the ground surface that increases the heat flux out of the ground. This enlarged heat flux also increases the insulating effect of the snow cover (*Romanovsky and Osterkamp*, 2000). To capture these effects in the CLM3, we need to include the unfrozen liquid water content in the CLM3, e.g. by (4.2).

Finally, we compare two numerical schemes by analyzing soil temperatures calculated by CLM3 and its modification (the enthalpy formulation of the heat equation). To highlight differences between two numerical schemes, we consider soil layers which have constant thermal properties and porosity. Also, just for this comparison we modify the original code to remove thermal effect of precipitation, moisture evaporation and incident solar radiation. In our simulations, the soil is initially thawed and its temperature is $4°C$. When the soil surface temperature falls below freezing temperature, the soil starts to freeze from the top down, and its temperature dynamics are determined by upper and lower boundary conditions. The boundary conditions are calculated directly by the CLM3. On the soil surface, the upper boundary condition is computed by the CLM3 from the energy balance principles, where the atmosphere temperature is set to be a linear, rapidly decreasing function of time. The lower boundary condition is also determined by the CLM3 and is zero heat flux at 3.43m.

Results of two simulations are shown in Figure 4.4. The soil temperature profiles computed by CLM3 have sharp corners and artificially stretched regions where the phase change occurs. Therefore, the thickness of developing frozen soil can not be computed accurately, but rather is estimated up to the thickness of adjusted layers. The proposed numerical scheme gives a better physical behavior of temperature, and allows an accurate prediction of the soil freezing depth. Further details regarding stability and accuracy of the proposed numerical scheme can be found in (*Voller and Swaminathan*, 1990; *Alexiades and Solomon*,

1992).

4.4 Conclusions

1. Introducing a deeper soil column, and the associated heat reservoir, into CLM3 results in more realistic annual mean and seasonal soil temperatures.

2. The thermal properties of the organic and organically enriched mineral soil layer play an important role for correct simulation of the temperature regime both in winter and summer.

3. Realistic treatment of unfrozen liquid water at temperatures below $0°C$ with a modification to the numerical scheme improve the simulation of permafrost dynamics, particularly at soil temperatures near $0°C$.

4.5 Acknowledgments

We would like to thank S.Marchenko and N.Mölders. This research was funded by National Science Foundation (OPP-0120736, IARC-NSF CA ARC-0327664), NASA, UAF CIFAR Student Award, and by the State of Alaska.

Bibliography

ACIA (2004), *Impacts of a Warming Arctic: Arctic Climate Impact Assessment*, 139 pp., Cambridge University Press.

Alexeev, V., D. Nicolsky, V. Romanovsky, and D. Lawrence (2007), How deep should be a minimum soil depth for adequate permafrost representation in climate models?, *Geophys. Res. Lett.*, *34*(9), L09502.

Alexiades, V., and A. Solomon (1992), *Mathematical Modeling of Melting and Freezing Processes*, 336 pp., Taylor Francis.

Anderson, D., R. Pusch, and E. Penner (1978), *Geotechnical Engineering for Cold Regions*, chap. Physical and thermal properties of frozen ground, pp. 37–102, McGraw-Hill, New York.

Anisimov, O., and F. Nelson (1997), Permafrost zonation and climate change in the northern hemisphere:results from transient general circulation models, *Climatic Change*, *35*, 241–258.

Brown, J., O. Ferrians, J. J. Heginbottom, and E. Melnikov (1997), Circum-arctic map of permafrost and ground-ice conditions, U.S. Geological Survey Circum-Pacific Map CP-45, 1:10,000,000, Reston, Virginia.

Collins, W., et al. (2006), The Community Climate System Model:CCSM3, *J. Climate*, *19*(11), 2122–2143.

Lachenbruch, A., J. Sass, B. Marshall, and T. Moses (1982), Permafrost, heat flow, and the geothermal regime at prudhoe bay, alaska, *J. Geophys. Res.*, *87*(B11), 9301–9316.

Lawrence, D., and A. Slater (2005), A projection of severe near-surface permafrost degradation during the 21st century, *Geophys. Res. Lett.*, *32*, L24401, doi:10.1029/2005GL025080.

Lawrence, D., and A. Slater (2007), Incorporating organic soil into a global climate model, *Clim. Dynam.*, 10.1007/s00,382–007–0278–1.

GSDT (2000), Global gridded surfaces of selected soil characteristics (IGBPDIS), *Available online [http://www.daac.ornl.gov/] from the ORNL distributed active archive center*, International Geosphere-Biosphere Programme - Data and Information Services, Oak Ridge National Laboratory, Oak Ridge.

Mölders, N., and V. Romanovsky (2006), Long-term evaluation of HTSVS frozen ground/permafrost component using observations at barrow, alaska., *J. Geophys. Res.*, *111*, D04105, doi:10.1029/2005JD005957.

Oleson, K., et al. (2004), *Technical description of the Community Land Model (CLM)*, NCAR Tech. Note NCAR/TN-461+STR, 173 pp., NCAR.

Osterkamp, T. (2005), The recent warming of permafrost in alaska, *Global Planet. Change*, *49*, 187–202.

Osterkamp, T., and V. Romanovsky (1999), Evidence for warming and thawing of discontinuous permafrost in alaska, *Permafrost Periglac.*, *10*(1), 17–37.

Romanovsky, V., and T. Osterkamp (1997), Thawing of the active layer on the coastal plain of the alaskan arctic, *Permafrost Periglac.*, *8*, 1–22.

Romanovsky, V., and T. Osterkamp (2000), Effects of unfrozen water on heat and mass transport processes in the active layer and permafrost, *Permafrost Periglac.*, *11*, 219–239.

Romanovsky, V., and T. Osterkamp (2001), *(eds), R. Paepe and V. Melnikov, Permafrost Response on Economic Development, Environmental Security and Natural Resources*, chap. Permafrost: changes and impacts, pp. 297–315, Kluwer Academic.

Samarskii, A., and P. Vabishchevich (1996), *Computational Heat Transfer, Mathematical Modeling*, vol. 1, 418 pp., Wiley.

Sazonova, T., V. Romanovsky, J. Walsh, and D. Sergueev (2004), Permafrost dynamics in the 20th and 21st centuries along the east siberian transect, *J. Geophys. Res.*, *109*, D01108, doi:10.1029/2003JD003680.

Stendel, M., and J. Christensen (2002), Impact of global warming on permafrost conditions in a coupled gcm, *Geophys. Res. Lett.*, *29*, 1632.

Voller, V., and C. Swaminathan (1990), Fixed grid techniques for phase change problems: a review, *Int. J. Numer. Meth. Eng.*, *30*, 875–898.

Walker, D., G. Jia, H. Epstein, N. Shiklomanov, F. Nelson, L. Hinzman, and V. Romanovsky (2002), Vegetation-soil-active layer relationships along a low-arctic bioclimate gradient, alaska, in *Eos. Transactions AGU*, vol. 83, pp. B72D–02, abstract.

Table 4.1: Thermal conductivity of frozen and thawed soils

Soil horizons	Depth	CLM3	Typically measured
Organic layer	0.0–0.2	1.8/3.3[a]	0.4/0.7
Mineral-organic mix	0.2–1.0	1.8/3.3	0.8/1.3
Mineral soil	1.0–3.0	2.1/3.3	1.2/1.9

[a] Thawed/frozen soil.

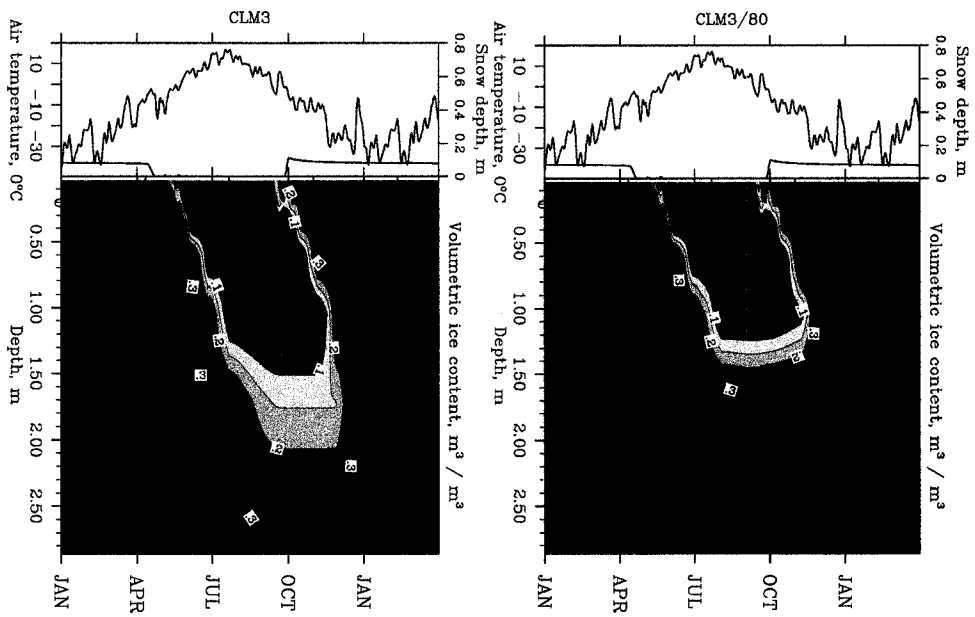

Figure 4.1: The air temperature and snow cover (upper plot) used to compute the volumetric ice content (lower plot) at Deadhorse for 3.43m and 80m thick soil columns without an organic layer.

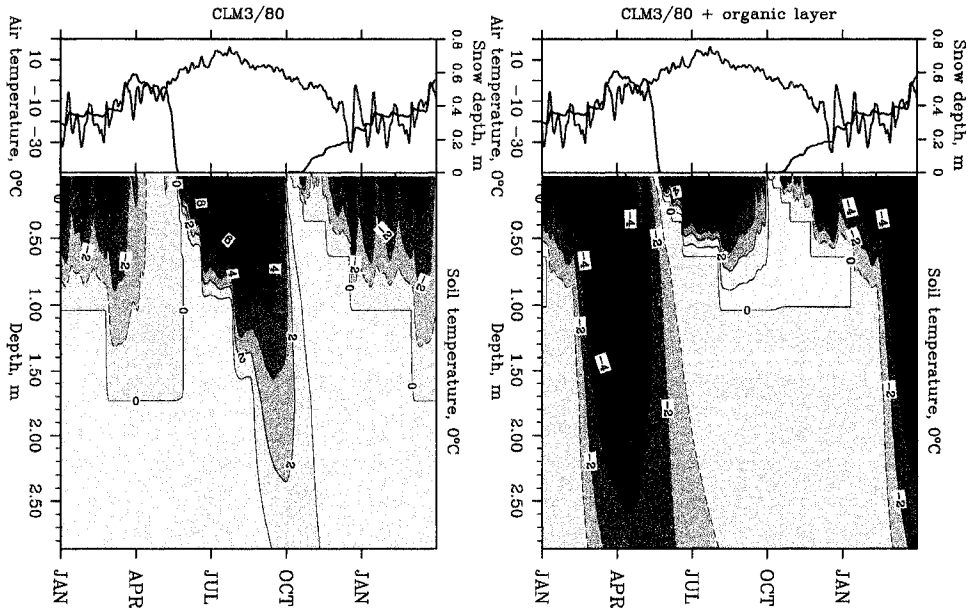

Figure 4.2: The air temperature and snow cover (upper plot) used to compute the soil temperature dynamics (lower plot) at Nome, Seward Peninsula, Alaska for 80m thick soil columns with and without an organic layer.

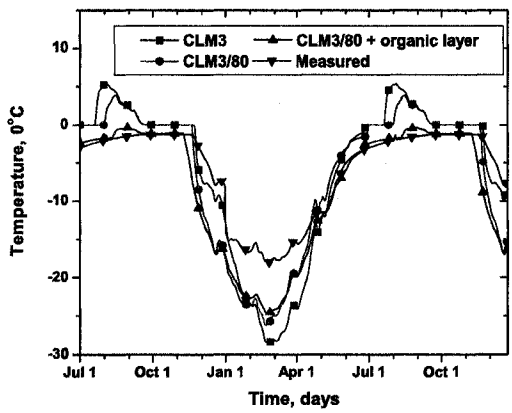

Figure 4.3: Measured and computed soil temperature at 1m depth at West Dock, near Deadhorse, Alaska.

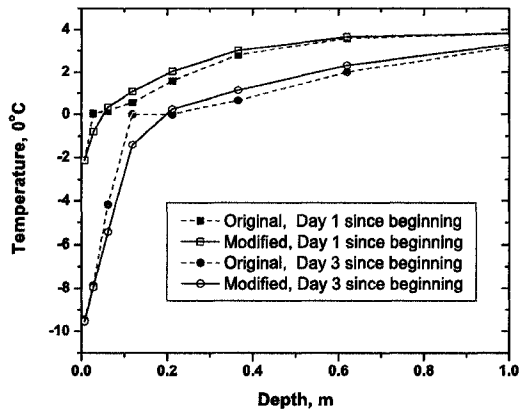

Figure 4.4: Temperature profiles calculated by the original (dotted line) and modified (solid line) numerical schemes.

Chapter 5
An evaluation of deep soil configurations in the CLM3 for improved representation of permafrost[5]

5.1 Abstract

A thin layer of soil used in many coupled global climate models does not resolve the heat reservoir represented by underlying ground material. Underrepresentation of this feature leads to unrealistic simulation of temperature dynamics in the active layer and permafrost. Using the Community Land Model (CLM3) and its modifications we estimate a required thickness of soil layers to calculate temperature dynamics within certain errors. Our results show that to compute the annual cycle of temperature dynamics for cold permafrost, the soil thickness should be at least 30 meters. Decadal-to-century time scales require significantly deeper soil layers, e.g. hundreds of meters. We also tested a new geometrical configuration of the soil layer geometry which is called slab permafrost. This configuration is represented by a thick soil layer underneath the traditional resolved soil layer. The model configuration with 30 meter deep resolved soil layer and a 30 to 100 meter thick slab shows results that favorably compare with our benchmark model which has a fully resolved 300 meter deep soil layer.

5.2 Introduction

Permafrost regions occupy approximately 25% of land in the Northern Hemisphere (*Brown et al.*, 1997). This is a climatologically important feature of the Northern high latitudes. Changes in permafrost are likely to have an impact on ecosystems, hydrology and infrastructure. The local communities of the North are very vulnerable to the thawing of permafrost and to associated changes in the northern environment.

In cold permafrost, a detectable annual cycle can be measured at depths of 15-20 meter (*Yershov*, 1998). This indicates that for proper simulation of the annual cycle in a soil model (with zero heat flux at the lower boundary conditions) a soil layer which is at least 20-30 meter deep is required. Longer time scales will obviously require deeper soil layer thickness. The position of the bottom boundary in a soil model in a climate model has an impact on the soil heating storage capacity (*Stevens et al.*, 2007). In the present chapter we estimate a

[5] V.A. Alexeev, D.J. Nicolsky, V.E. Romanovsky, and D.M. Lawrence, 2007, "An evaluation of deep soil configurations in the CLM3 for improved representation of permafrost", published in Geophysical Research Letters, 34(9): L09502

minimum total soil layer thickness that is required to reasonably describe soil temperature dynamics across a range of different time scales. Using a linear heat diffusion equation we analytically estimate the error of simulations in a shallow soil layer model compared with the exact formulation in a semi-infinite domain. This study can be considered as a test of what kind of biases different configurations of model soil layers can introduce in the simulation of permafrost. A new configuration for climate models is suggested and tested with a thick slab soil layer underneath the traditional GCM upper soil model. This configuration can potentially save time without loss of quality of simulations. All of our runs are driven by the same forcing, namely, NCEP/NCAR reanalysis persistent year 1998 forcing, for a location roughly corresponding to typical observed Alaskan North Slope conditions.

5.3 "Back of the envelope" calculations

We intentionally decided to simplify processes during soil freezing by omitting any water phase change effects, although we acknowledge that these effects are very important. This simplification is valid for model temperature dynamics below the active layer depth where the unfrozen liquid water content is usually negligible. To derive an analytical solution to the heat equation, we assume that the thermal properties for the thawed and frozen ground material are the same.

5.3.1 Analytical solution for diffusion equation in limited and unlimited domains

In this section, we consider a one dimensional heat equation

$$\frac{\partial T(z,t)}{\partial t} = D\frac{\partial^2 T(z,t)}{\partial z^2}, \tag{5.1}$$

in a bounded interval $z\in[0,H]$. Here D is a diffusion coefficient. Given the boundary condition at the surface $z=0$ and some depth $z=H$:

$$T(0,t) = Ae^{i\omega t}, \quad \frac{\partial T}{\partial z}|_{z=H} = 0,$$

we look for a periodic solution of (5.1) in time t. Here, the constant A is the amplitude of temperature oscillations on the soil surface, $\omega=2\pi/\tau$ is the frequency of the forcing at the boundary and τ is the period of the forcing. We also consider a bounded solution $T_\infty(z,t)$ of the heat equation (5.1) in a semi-infinite domain $[0,\infty]$ with the same boundary condition on the surface.

It is easy to show (*Carslaw and Jaeger*, 1959) that T_∞ which we call the exact solution is

$$T_\infty(z,t) = Ae^{i\omega t-(1+i)z/h}. \tag{5.2}$$

where $h = \sqrt{2D/\omega}$ is a characteristic vertical damping length. The solution of (1) for the limited domain $[0, H]$ is:

$$T(z,t) = Ae^{i\omega t}\frac{(e^{(1+i)(z-H)/h} + e^{-(1+i)(z-H)/h})}{(e^{(1+i)H/h} + e^{-(1+i)H/h})} \tag{5.3}$$

We define the solution error due to using limited domain in the following way:

$$\Delta T(\tau,H)=\sqrt{\frac{1}{\tau}\frac{1}{H}\int_0^\tau\int_0^H |T(z,t)-T_\infty(z,t)|^2 dtdz} \tag{5.4}$$

This error as a function of the total soil layer depth H and the period τ of the surface temperature oscillations is shown in Figure 5.1a. The error is small when the soil layer depth is very shallow or when it is very deep. When the model soil layer is very shallow (and therefore heat storage of the soil layer is small) the solution is completely controlled by the surface forcing for large enough τ (which in this case serves as a measure of persistence of the forcing). The warming/cooling periods in this case are slow enough and also they last long enough time so that because of the too low heat capacity soil temperature simply follows the changes in the atmospheric temperature. The error becomes small again when the model total soil layer depth is much thicker than the corresponding characteristic damping length. In this case the bottom boundary does not "feel" the surface, nor does the model domain "feel" the effect of the bottom boundary. There is a maximum in the error when the total soil layer depth is comparable with the vertical damping length. In this case the bottom boundary has a maximum effect on the model solution. The heat capacity of the total model soil layer is still too low because of the no-flux lower boundary condition. Therefore the heat, which normally goes to the deeper soil, keeps accumulating in the upper soil layers. This results in a too high sensitivity of soil to changes in the surface forcing. This would be the main point of the chapter: depending on the timescale of interest the lower boundary should be placed far enough from the surface so that the total soil depth is much greater than the corresponding damping length h. The location of the error maximum is always the same - near the soil layer bottom (Figure 5.1b). The timescale corresponding to this maximum gets longer as the total model soil layer depth deepens. For the 30 meter deep total soil layer shown in Figure 5.1b the timescale of maximum error is at approximately 200 years. For a 3-4 meter deep soil layer the picture looks very similar (not shown) with a

maximum error at about 2 years. After reaching the maximum, the error starts decreasing because for very long timescales the temperature dynamics of the soil layer becomes fully controlled by the surface forcing.

We can define the relative amplitude error as the absolute value of the difference between the amplitudes of the exact solution for the semi-infinite domain and that of the finite domain divided by the amplitude of the exact solution. It can be shown that the behavior of the amplitude error non-monotonically depends on the total soil layer depth if we look at a fixed depth. We will see this effect later on in our numerical experiments.

5.3.2 Characteristic vertical damping lengths for different time scales

The damping length h enters both the solution in the limited and unlimited domains. Frequency of the time signal is an important factor affecting this damping length. Therefore this simple formula can be used to assess how deep the soil layer in a model should be depending on a time scale of an arbitrary external forcing. Let us define the constants in the following way: $D = d_0 10^{-7} m^2/s, \omega = 2\pi/T = 2\pi/n \times 86400 \times 365 s^{-1} \approx (2*10^{-7}/n)\ s^{-1}$. Here for typical soils d_0 would vary between 1-20 and n would denote number of years in a period of the applied periodic forcing. The formula for the damping length then becomes the following $h \approx \sqrt{d_0 n}$. For $d_0 = 10$ and $n = 365^{-1}$ (diurnal cycle) we get $h \approx 0.15$ meters. For $d_0 = 10$ and $n = 1$ (annual cycle) we get $h \approx 3$ meters for the damping height of the seasonal cycle, consistent with measurements by (*Osterkamp and Romanovsky*, 1996) in cold permafrost showing the damping factor of about 3 at 3 meter depth. This is why the soil layer thickness in the standard CLM3 (3.4 meters) is too shallow to approximate the semi-infinite domain problem. The above estimates show that even for seasonal timescales the soil layer depth should not be smaller than 25-30 meters. For timescales longer than a century we need to use 10 times thicker soil layer – 200-300 meters. Millennial scales will require even deeper soil layer - 500 meters and more.

5.4 Model sensitivity tests with the CLM3

Our error estimates are tested using the CLM3 with different soil layer configurations driven by the same forcing. The reference solution is calculated using the model with total soil layer thickness equal to 300 meters. The upper 3.4 meters of soil in this model are identical to the standard CLM3 model configuration with 10 layers. The thickness of added soil layers underneath is exponentially increasing from 1.2 to 7.0 meters. The total number of

layers added is 90. The reference solution inherits all the problems typical for the given model. We discuss some of the problems of the current version of the CLM3 in our other paper (*Nicolsky et al.*, 2007). All the model configurations used for comparison are identical to the CLM3 soil model in the upper 3.4 meters. The CLM3 with 300 meter thick soil is spun-up for 2000 years before we start collecting the statistics of the reference solution.

We conduct runs with different soil layer thicknesses (3.4, 10, 30, and 100 meters) and different periodic forcings with periods: 1 year (annual cycle), 20 years, 60 years, 200 years, 600 years, 2000 years. For the annual cycle we use the NCEP forcing that comes with the CLM3 in the persistent 1998 regime. All other periods represent artificially added perturbations with $5°C$ amplitude in the surface temperature oscillating with the corresponding periods. This is done in order to mimic different timescales of the long-term variability of the atmospheric forcing.

Slab soil layer configurations, upper level resolved soil layers with a thick layer underneath, were also tested. The tested configurations included three different slab layer depths (30, 100, and 300 meters) underlying 2 resolved soil layer depths (3.4 and 30.0 meters). We are evaluating this type of configuration as a computationally cheaper alternative to the more straightforward solution: adding a large number of deep layers. The upper layers are run in their usual mode (the resolved soil) while the layer underneath is represented by just one very thick mineral soil layer (ranging from 30 to 300 meters in thickness), and one more thinner layer of soil to implement the no flux lower boundary condition. The slab configurations are marked as $(X+Y)meters$ in the text below where X and Y show depths of the resolved and slab soil layers correspondingly.

5.5 Results

To quantify the accuracy of our model in different configurations we calculate the "error" of the solution at 1 and 3 meters for different configurations assuming the solution with 300 meters soil thickness represents the reference solution. The error is defined as a root mean square deviation of the approximate solution from the reference solution divided by the root mean square of the reference solution. Another measure of the quality was the error of the solution at different timescales. For the reference solution we calculate the amplitudes of the solution at frequencies corresponding to the periods of long-term oscillations in the forcing at 1 and 3 meter depths. The relative amplitude error at a certain frequency is calculated by dividing the absolute difference between the amplitudes of the approximate

and the reference solution by the amplitude of the reference solution. The amplitude error will indicate how different timescales are reproduced in models with different configurations of soil layers. Looking at the conventional solution error as defined at the beginning of this section may not be enough since it will include all timescales.

5.5.1 Seasonal cycle

The standard CLM3 configuration with total soil layer thickness of 3.4 meters does not adequately reproduce the seasonal cycle compared to the 300 meter deep soil layer model. The model has strong biases – warm in the beginning of the cold season and cold in the spring (Figure 5.2a). The cooling at 1 meter in the model with 3.4 meter deep soil layer is delayed by approximately 20 days and the model shows later recovery from the colder winter temperatures. The 3.4 meter model warms up too much in the summer and cools down in the winter, compared with the 300 meter deep soil model (Figure 5.2b). This happens because in the 3.4 meter model the heat cannot propagate downwards beyond the lower boundary due to the no flux condition at the bottom. Therefore only the shallow 3.4 meter deep soil layer is thermodynamically active, which further helps accumulate even more heat in the model layers. Therefore the entire soil layer beneath 1 meter in the 3.4 meter soil model is at the freezing point in the summer. However, the amounts of unfrozen water are quite different for the 3.4 meter model and the reference model with 300 meter deep soil layer. For example, in the 3.4 meter model within the soil layer located between 0.76 and 1.31 meters, 80% of ice turns into water during thawing, whereas in the 300 meter model within the same layer about only 40% of ice melts. When we use 3.4 meter deep resolved soil layer with a 30 meter slab layer, the problem is opposite. The thick slab layer adds too much thermal inertia to the system, therefore the biases are just the opposite compared to the model with 3.4 meter deep soil, which is also shown in Figure 5.2.

The results on comparison of models with different soil layer configurations are summarized in Table 5.1. Analysis of Table 5.1 suggests that a minimum of 30 meters of resolved soil layer is necessary for proper simulation of the seasonal cycle. The 100 meter thick soil layer model produces the same results as the model with 30 meter thick soil layer, with- or without a slab layer of different depths (30, 100 or 300 meters). Therefore for the reasonable reproduction of the seasonal cycle a 30 meter deep resolved soil depth appears to be sufficient. Deeper soil thicknesses will be important for longer timescales as we will see later.

5.5.2 Long timescales

Figure 5.3 demonstrates the fact that a too shallow soil layer depth and therefore too low heat capacity results in too much sensitivity of the soil temperature at the lower boundary (3.4 meters). We see that the model with a 3.4 meter soil layer constantly overshoots and undershoots the more inert soil model with overall depth of 300 meters. The difference can be as big as 4-6K on timescales of a decade. Adding 30 meter deep slab to the same 3.4 meter deep soil significantly improves the solution (see Table 5.1). One might be inclined to choose this configuration as a compromise between the accuracy and computational efficiency, but as we know the 3.4+30 configuration failed the seasonal cycle test. From Table 5.1 we can see that the models with 30 meter deep resolved soil layer and 100 meters of slab underneath and the model with 100 meter deep soil layer probably show best results in the long-term integrations among all the configurations, but a number of other alternative options will give similar results. For example, there is a significant improvement as we just go from 3.4 to 30 meter deep soil layer. Too thick slab layer (300 meters) makes the upper soil feel the thermal inertia of the layer underneath. We can see that this configuration underestimates the variability. Table 5.2 gives the model amplitude error in our long-term integrations. We see that shallow soil layers (3.4 and 10) significantly overestimate variability on all timescales, especially on shorter periods. Adding a slab improves the situation, only if the slab is not too thick. Models with 100 and 300 meters thick slab layer strongly underestimate variability on shorter periods.

5.6 Conclusions and discussion

The main purpose of the chapter is to test sensitivity of the CLM3 to various geometries of the soil layers. The results of simulations with various total soil depths were compared with a reference solution represented by a model configuration with 300 meter deep soil layer. A slab configuration represented by a resolved soil layer (3.4 or 30 meter deep) with a thick layer of soil underneath is proposed and tested against the reference solution. Solution error is estimated for various time scales by forcing the model with a periodic surface forcing across a variety of frequencies that mimic annual, decadal and century timescales. The main conclusions are the following.

1. The standard 3.4 meter soil layer used in the CLM3 significantly overestimates the temperature variability on all time scales, from seasonal to decadal and longer.

2. We estimate that in order to properly reproduce the seasonal cycle of the temperature a model soil layer should be at least 25-30 meters deep. Decadal and longer time scales require 100 meter and deeper soil layer. The best configuration is somewhat dependent on the timescale of interest.

3. A slab permafrost configuration with at least a 30 meter deep resolved soil layer with a thick slab layer beneath could be a computationally cheaper but reasonable alternative to a deep soil model with fine resolution throughout the depth.

4. Deepening of the model total soil layer seems to improve the described modeling results. However, with deepening of the soil layer there maybe some other contraints that may influence the quality of simulations - e.g. interaction with soil hydrology.

5.7 Acknowledgments

The work was supported by the NSF Cooperative Agreement 0327664, and UAF CIFAR Student Grant Award. Computer simulation were carried out at Arctic Region Supercomputing Center.

Bibliography

Brown, J., O. Ferrians, J. J. Heginbottom, and E. Melnikov (1997), Circum-arctic map of permafrost and ground-ice conditions, U.S. Geological Survey Circum-Pacific Map CP-45, 1:10,000,000, Reston, Virginia.

Carslaw, H., and J. Jaeger (1959), *Conduction of Heat in Solids*, 520 pp., Oxford University Press, London.

Nicolsky, D., V. Romanovsky, V. Alexeev, and D. Lawrence (2007), Improved modeling of permafrost dynamics in a GCM land-surface scheme, *Geophys. Res. Lett.*, *34*, L08501.

Osterkamp, T., and V. Romanovsky (1996), Characteristics of changing permafrost temperatures in the alaskan arctic, usa, *Arctic Alpine Res.*, *28*, 267–273.

Stevens, M., J. Smerdon, J. Gonzalez-Rouco, M. Stieglitz, and H. Beltrami (2007), Effects of bottom boundary placement on subsurface heat storage: implications for climate model simulations, *Geophys. Res. Lett.*, *34*, L02702.

Yershov, E. (1998), *General Geocryology*, 604 pp., Cambridge University Press, Cambridge.

Table 5.1: Solution error, % at different depths

Case	Seasonal cycle			Long term	
	0.4m	1m	3m	1m	3m
3.4m	23.6	35.8	61.7	21.7	29.1
10m	5.7	6.60	5.80	11.9	17.6
30m	0.85	1.33	2.15	6.33	7.39
100m	0.84	1.31	2.16	5.35	5.38
3.4+30m	33.7	45.5	70.9	8.75	11.25
3.4+100m	43.8	57.4	90.4	19.1	28.7
3.4+300m	45.9	60.5	96.7	33.5	50.5
30+30m	0.84	1.31	2.16	4.53	5.10
30+100m	0.84	1.31	2.16	2.41	3.10
30+300m	0.83	1.28	2.19	5.17	6.35

Table 5.2: Amplitude error, % for different timescales.

Case	1 meter depth			3 meter depth		
	200yrs	60yrs	20yrs	200yrs	60yrs	20yrs
3.4m	7.72	18.4	17.6	13.4	29.5	46.7
10m	5.54	12.6	7.07	10.4	22.3	30.9
30m	3.07	-2.29	-8.87	6.27	-1.3	-1.5
100m	-1.28	-1.38	-7.78	-1.12	-0.50	0.14
3.4+30m	0.77	-2.49	-13.6	4.11	0.75	-4.10
3.4+100m	-4.00	-12.8	-38.2	-3.11	-11.1	-40.4
3.4+300m	-13.4	-41.5	-52.8	-13.4	-49.9	-76.7
30+30m	-0.08	-1.72	-8.18	0.84	-1.30	-0.30
30+100m	-1.59	-1.99	-7.34	-2.05	-2.04	0.98
30+300m	-4.09	-1.17	-6.72	-6.37	-1.13	1.93

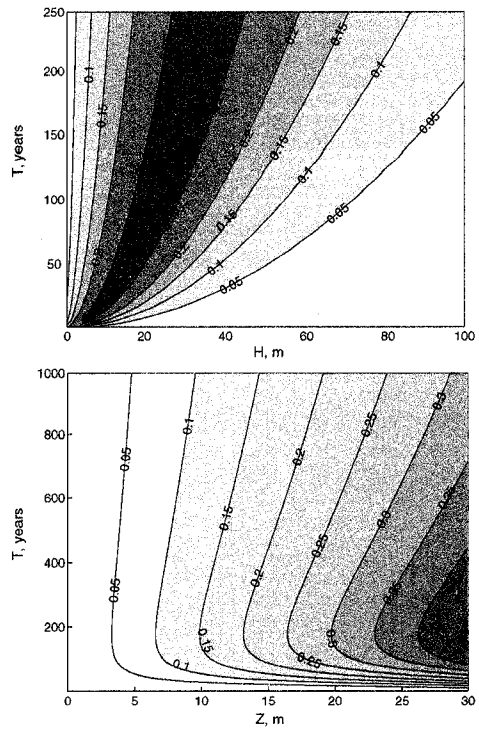

Figure 5.1: Solution error, analytical case (idealized periodic forcing with $1°C$ amplitude). Upper panel – vertical integral of the absolute value of the difference between the solution for the semi-infinite domain and that obtained for finite domain as a function of the total soil layer depth (m) and oscillation period of the applied surface forcing. lower panel – absolute value of the difference between the solution for the semi-infinite domain and that for the finite domain as a function of depth and oscillation period of the applied surface forcing for the model with 30m deep soil layer

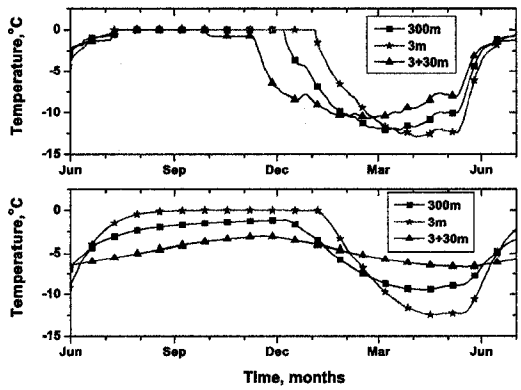

Figure 5.2: Soil temperatures at 1.0 and 3.0 meter depths. Upper panel - soil temperature at 1m, lower panel - 3m (configurations 300m, 3.4m, 3.4+30).

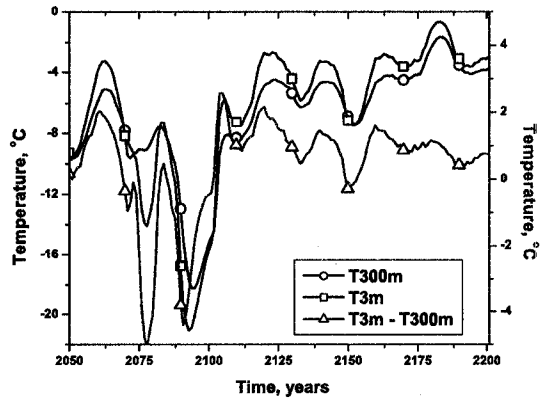

Figure 5.3: Solutions at 1.0 meter for 300.0 and 3.4 meter configurations and the difference between them.

General Conclusions

The future fate of permafrost is controlled by climatological, biological, geological, and hydrological factors. At present, numerical modeling is a cornerstone in understanding inter-connections between these factors, and in predicting the future changes in permafrost distribution, its temperature and thickness. In this thesis we presented some aspects of numerical modeling of the active layer and permafrost dynamics.

1. We applied a variational data assimilation technique to determine soil properties: soil porosity, thermal conductivity, and the parametrization of the unfrozen water for the fully saturated ground material in the active layer and permafrost. To compute the soil properties, we minimized a multivariate cost function describing the discrepancy between the measured and calculated temperatures during a certain time interval. In the presented variational approach, one of the crucial steps is selection of the initial approximation to the soil properties.

   We developed an algorithm to calculate the initial approximation by solving a sequence of simpler subproblems in a certain order. The proposed method of finding the initial approximation is to adapt a coordinate-wise iterative minimization technique to the specifics of our inverse problem. At each iteration, we select a particular set of soil properties and associate with them a certain time interval over which we minimize the cost function. After employing the proposed sequence of iterations, we find the initial approximation to the soil properties.

   Although the proper initial approximation is important, efficient and accurate calculation of the temperature dynamics in the freezing and thawing ground is important too. Therefore, we developed a new finite element discretization of the Stefan-type problem on fixed coarse grids using enthalpy formulation. One of the advantages of the new method is that it allows computation of the temperature dynamics for the classical Stefan problem without any smoothing of the enthalpy. Also, the new approach shows equal or better performance compared with other finite element models of the ground thawing and freezing processes.

   We conducted a sensitivity analysis of the computed soil properties with respect to a typical configuration of soil layers (to simplify the inverse problem we assumed that the soil properties are constant within each soil horizon) and in-situ observations.

Based on results of this sensitivity analysis we conclude that for high resolution-in-time temperature records at several depths below the soil surface, and occasional measurements in a adjacent deep borehole, it is possible to estimate thermal conductivity for all soil layers. However, soil porosity and parametrization of the unfrozen water content can be identified only for intermediate layers where active phase change occurs.

One of the limitations of the presented variational approach is that it requires values of heat capacities in order to find a unique value of the thermal conductivity and soil porosity. Another limitation of the presented approach is that we compute the volumetric content of water which changes its phase during freezing or thawing. Water content of liquid water that is tightly bound to soil particles and is not changing its phase in a range of naturally occurring temperature variation can not be estimated within the presented permafrost model. Additionally, we used one dimensional assumption regarding the heat diffusion in the active layer, which sometimes is not applicable due to hummocky terrain in the Arctic tundra. Another assumption used in the model is that the frost heave and thaw settlement are negligible and there is no ice lens formation in the ground during freezing. Therefore, the proposed method could be only applied if these assumption are satisfied.

Although there are limitations to the presented approach, we successfully applied it to recover soil properties for several sites along the Dalton highway in Alaska: West Dock, Deadhorse, Franklin Bluffs, Happy Valley, and Imnaviate Creek . We computed most probable estimates of the soil properties for the above sites. At sites where the soil properties were previously determined, the presented approach gives values that are no more than 25% different from the previously found values. One of the advantages of the presented approach is its ability to asses errors in the recovered soil properties. Using the recovered soil properties, we computed the soil temperature dynamics at the above-mentioned sites. The difference between the simulated and measured temperature dynamics over the periods of testing and calibration is typically less than $0.3°C$.

2. A new numerical thermo-mechanical model of differential frost heave was developed with special emphasis on simulating the biocomplexity of non-sorted circle ecosystems. This model takes into account the basic thermodynamic principles: energy, momentum, and mass conservation laws and consequently simulates the observed frost heave

in non-sorted circles. The governing system of equations is reduced to a computationally convenient set of strongly coupled equations for temperature, liquid water pressure, porosity, and the velocity of soil particles in a three-dimensional domain with an assumption of cylindrical symmetry. A finite element and fictitious domain methods in conjunction with the implicit scheme in time are employed to construct a non-linear system of equations, which are solved iteratively. Despite the simplicity (no diffusion of salts, simplified rheology) the model captures and successfully simulates temperature and water dynamics in soil. Also, the model satisfactory simulates the ground surface motion in relation to frost heave and explains the dependence of the amount of frost heave on specific environmental properties of this ecosystem.

The model was tested using observational data obtained from several sites within the Permafrost/Ecological North American Arctic Transect. We obtained a good comparison between simulated and observed dynamics of physical processes in the non-sorted circle at the Franklin Bluffs. The model also qualitatively represents "non-heaving" non-sorted circles at the Howe Island site. Therefore, accomplished testing of our numerical model provides an assurance that this model can be used to study the impact of changes in major natural geophysical and biological drivers on specific properties and dynamics of the non-sorted circles ecosystem. Sensitivity analysis provided deeper understanding of functioning of the non-sorted circle as an ecosystem. It was discovered that the most active development of differential frost heave takes place for non-sorted circles within waterlogged areas with strong upper-soil-layer heterogeneity caused by living vegetation. The simulated frost heave is found to be sensitive to hydrological soil properties, and to change in the vegetative insulation layer within the circle and inter-circle areas. The results of our sensitivity analysis with respect to addition/removal of vegetation layer to/from the surface of a circle are well correlated with a field manipulation experiment, where a layer of organic material was added to the non-sorted circle, or removed. The performed sensitivity analysis allows drawing a conclusion that the most important driver of the non-sorted circle ecosystem is the presence of vegetation which over a significant time, changes the soil mineralogy and thermal and hydrological soil properties, thus changing the amount of differential frost heave and reducing or enhancing all bio-geophysical processes responsible for the formation and evolution of the non-sorted circles.

The developed model can be used to explain the specific behavior of the non-sorted

circle ecosystems in different ecological regions. Also, this model provides a very powerful tool for investigation of possible future changes in this ecosystem in relation to observed and projected climatic and biological changes in the Arctic.

3. We found that computations with a standard soil layer thickness in the Community Land Model 3 (CLM3) significantly overestimate the temperature variability on all time scales from seasonal to decadal and longer. However, the inclusion of a deeper soil column, and the associated with it heat reservoir, into CLM3 results in more realistic annual mean and seasonal soil temperatures. We found an optimal depth of the soil column in the CLM3 by testing various geometries of soil layers in CLM3. We estimated that in order to properly reproduce the seasonal cycle of the temperature a model soil layer should be at least 25-30 meters deep. The modeling on decadal and longer time scales require 100 meters and even deeper soil layers.

   We noticed that the present version of CLM does not include the effect of soil organic material on the thermal and hydraulic properties of the soil. We illustrated the importance of including an organic layer by analyzing soil temperature dynamics at a certain site located in the Seward Peninsula. On a basis of this example, we showed that thermal properties of the organic and organically enriched mineral soil layer play an important role for correct simulation of the temperature regime both in winter and summer. Additionally, we suggested to add a realistic treatment of unfrozen liquid water with a modification to the numerical scheme in order to improve simulations of permafrost dynamics, particularly at soil temperatures near $0°C$.

In conclusion, the findings presented in this thesis provide a better understanding how to parameterize permafrost models, to compute the frost heave, and to constrain General Circulation Models.